Studies on Turning Difficult-to-Machine Materials with Super Hard Tools — Cutting characteristics of titanium alloy and sintered carbide —

Dissertation

Studies on Turning Difficult-To-Machine Materials with Superhard Tools – Cutting Characteristics of Titanium Alloy and Cemented Carbide

超硬質工具による難削材の旋削加工に関する研究
―チタン合金および超硬合金の切削特性―

Graduate School of Natural Science & Technology

Kanazawa University

Division of Innovative Technology and Science

System Design and Planning

Student ID Number : 1323122001

Name : Abang Mohammad Nizam
Abang Kamaruddin

Chief advisor : Prof. Akira Hosokawa

Date of Submission : March 22th, 2016

TABLE OF CONTENT

CHAPTER 1: INTRODUCTION

1.1 Turning

Material removal methods have been used in shaping solid material since the Neolithic period (8000–3000 BCE), including carving, woodworking and grinding. Although metal alloying techniques were used in the Bronze Age (3500–1500 BCE), it was not until the Industrial Revolution (1770–1850) that modern methods of material removal were developed in manufacturing. For metal, these include boring, turning, drilling, milling, shaping and planning [1].

Turning is one of the most important techniques in material removal. It is used to remove layers of materials, and involves the rotation of a workpiece as a cutting tool is moved across its surface. The cutting tool is set to a pre-specified cutting depth (in mm or inches) with the cutting surface parallel to it, and moves with a pre-specified velocity in relation to the rotation speed of the workpiece. This velocity rate (called the ‘feed rate’) is simplified as the distance travelled by the tool parallel to the cutting surface per unit of revolution of the workpiece (stated in mm/rev or in./rev) [2].

1.2 Difficult-to-machine material

The term ‘difficult-to-machine material’ is self-explanatory. These types of material entail greater manufacturing costs to produce components. These stem for example from reduced tool life, increased production time and unsustainable accuracy. Several materials have been identified as difficult to machine, such as titanium alloys, Inconel, and cemented carbide. This study focuses on titanium alloys and cemented carbide (tungsten carbide with cobalt binder), as these materials are commonly used in various industries.

1.2.1 Titanium Alloys

Titanium is an elusive material with highly desirable material qualities, which has been used in the aerospace, medical, automotive industries among several others, owing to its high strength-to-weight ratio, ability to withstand elevated temperatures, and excellent corrosion and fracture resistance. The aerospace and military industries have been the main users of titanium alloys – sometimes known as ‘marvel metals’ – which have increased production and allowed the manufacture of smaller components. However, difficulties during machining makes manufacturing products using titanium very expensive. This is due to chemical instability during cutting, which leads to reactions between tools and workpieces. To reduce this effect, the machining process is tuned down in order to elongate tool life. But this reduces productivity, even as demand is increasing. Careful selection of cutting tool is also important in order to minimize instability during the cutting process.

Titanium alloys are basically materials that contain titanium and other chemical elements. The main reason for alloying is to improve the mechanical properties of titanium to enable the metal to be used in extreme applications, for example in the aerospace and biomedical industries. Titanium alloys can be basically classified into three major classes: alpha alloys, alpha–beta alloys, and beta alloys. These are based on the microstructures of these materials, and involve various additions and processes.

Basically, alpha alloys are much stronger but less ductile than beta alloys, while alloys with both alpha and beta characteristics have medium strength and ductility [3]. Alpha alloys are alpha-phase alloys that are not thermally treatable. These alloys generally contain a large amount of aluminum, ensuring excellent strength and oxidation resistance at elevated temperature. Examples of alpha alloys are Ti-5Al-2.5Sn and pure titanium. Alpha–beta alloys are basically alpha alloys that contain beta-stabilizing elements (such as vanadium, ferum, molybdenum and silicon). The role of beta structure in titanium alloys is to allow heat treatment to be applied to modify the strength. One example of an alpha–beta alloy is Ti-6Al-4V. Lastly, beta alloys contain a large percentage of metastable beta-phase due to sufficient beta-stabilizing elements. These elements in turn maintain the beta-phased structure of titanium alloys after quenching (thermal treatment), and also enable this type of alloy to be solution and age treated. Stable beta-phased alloys can only be annealed. An example of a beta alloy is Ti-10V-2Fe-3Al. The microstructure of the aforementioned alloys is depicted in **Fig. 1.1**.

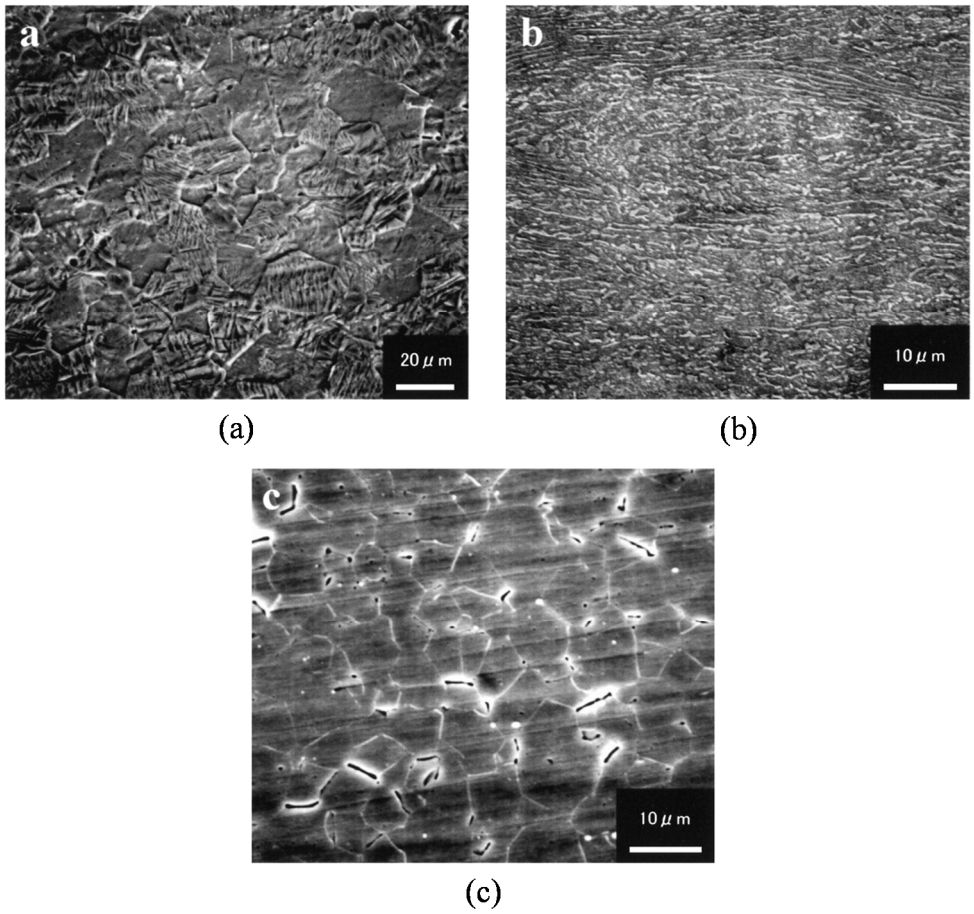

Fig. 1.1 Microstructure SEM photographs of (a) alpha phase of pure titanium, (b) alpha–beta alloy of Ti-6Al-4V and (c) beta alloy of Ti-33Nb-15Ta-6Zr [4]

1.2.2 Cemented Carbide

Cemented carbide is a metal matrix composite where hard carbide particles or grains are bonded or cemented together with metal binder (commonly used binders are cobalt and nickel), with or without a small percentage addition of other metals. These materials are usually found in cutting tools and have been used to make dies and molds. The hard carbides used in cemented carbide are titanium carbide (TiC), tantalum carbide (TaC) and tungsten carbide (WC) [1]. The hardness of these materials is influenced by the percentage by weight of the binder, whereby the lower the binder content, the harder and less tough the material becomes.

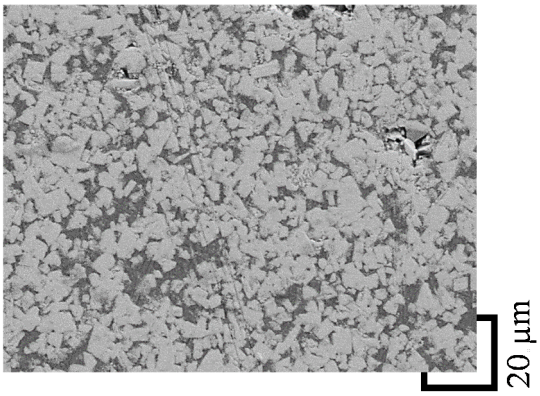

Fig. 1.2 Sintered cemented carbide of tungsten carbide with cobalt binder

Common properties of these cemented carbides are very high physical strength and considerable thermal conductivity. Due to these properties, cemented carbide is widely used for making molds and dies, and also in cutting tools. **Fig. 1.2** shows a typical cemented carbide grain under an SEM microscope; the black spots represent the cobalt binder in the cemented carbide with tungsten carbide in light grey.

Cemented carbides are manufactured by a sintering process and shaped as desired by using EDM and diamond grinding. The sintered grain of tungsten carbide with cobalt is shown in **Fig. 1.3**. These shaping methods are very expensive, thus increasing the overall production cost. Research is needed in turning and milling in mold making. These have been seen as alternatives to existing processing methods, which could reduce dependency on or completely replace diamond grinding in the cemented-carbide material removal process. Cutting of tungsten carbide is known to be chemically stable.

1.3 Cutting Temperature

Tool life plays an important role in determining quality of surface roughness. Tool life is related to the tool wear rate during workpiece cutting. In turning, tool wear depends on the tool and workpiece material, cutting speed, feed speed, cutting depth, and coolant or cooling method. In order to increase production rate, cutting speed and depth of cut can be increased. But in increasing production rate, tool wear also increases.

Cutting temperature is one of the most important parameters indicating the energy produced during cutting. It is a product of shearing and friction forces that emerge during cutting between the tool/chip and also the tool–workpiece interface. The higher the energy in the cutting, the higher the cutting temperature will be; this relationship depends on the cutting depth, feed rate and cutting speed. Cutting temperature is also influenced by several other factors including thermal conductivity, tool/workpiece hardness, ductility, coolant, and lubrication.

Temperature – especially high temperature – is very important in cutting due to its effects. Excessive thermal energy generated during cutting is one possible factor in lowering the strength, hardness, stiffness and wear resistance of the cutting tool, which in turn can lead to plastic deformation that changes the tool's geometry. Such excessive energy also influences accuracy and dimension on the workpiece during cutting. At very high cutting temperature, thermal damage and metallurgical changes usually occur and induce undesired properties on the machined surface [2].

1.4 Previous research

Several studies touch on cutting of cemented carbide, particularly in micromachining [6, 7]. These studies assess the possibilities of replacing diamond grinding. Conventional cutting of cemented carbide is still lacking. This might have been influenced by the move to near-net dimension manufacturing. However, studies discussing the performance of cutting tools, especially ultra-hard tools such as CBN and diamond-based tools, in conventional cutting of cemented carbide is relatively low [8, 9].

Meanwhile, the literature on cutting of titanium alloys is extensive. Cutting performance of tools has been tested and methods for pre-selection of suitable tools for cutting of titanium alloy have been formulated [10, 11]. It should be noted that the cutting of titanium alloys induces high temperature, which has a thermal effect on the tool. Demand for these hard-to-machine materials means they have gained a lot of interest from researchers in particular in the development of tool materials and cooling methods. The trend is skewed toward high-speed cutting to save process time and increase production rate [12].

It is well known that cutting of titanium alloys induces very high cutting temperature. Almost all of the studies done in this area show high tool wear on tools used in cutting of titanium alloys, especially in high-speed cutting. Nabhani provides evidence that titanium carbide provides a layer of protection in a PCD tool, but further research is needed to corroborate this finding [13]. Meanwhile, Rahman et al. concluded that binderless CBN makes the best tool for cutting of titanium alloy in high-speed milling [11]. It should be noted that the

studies on cutting of titanium alloys reveal that tools with high thermal conductivity are preferred [10, 11].

It has been found that the CBN tool performs better in comparison to PCD in cutting of cemented carbide, and that cutting of cemented carbide is harder with lower binder content [8, 9]. Tool wear in cutting of cemented carbide is attritional [8, 9]. There has been little discussion of tool failure in cutting of cemented carbide or cutting temperature.

1.5 Objectives of the study

This study focuses on the performance of superhard tools in cutting difficult-to-machine materials, in this case titanium alloy (Ti-6Al-4V) and cemented carbide (WC-Co), two materials that occupy each end of the range of difficult-to-machine materials: they have opposing properties, being very soft and very hard materials, respectively. They are both vulnerable to chemical wear. It is important to pursue further understanding of these tools and their material reactions, as difficult-to-machine materials are in high demand.

Superhard tools are tools that contain CBN and diamond as the base materials, with a minimum hardness of 30 GPa HV (14). These tools have three major desirable mechanical properties: high thermal conductivity, low thermal expansion, and low friction coefficient. These properties mean superhard tools have come to be in high demand in manufacturing industries. In this study, superhard tools, in particular diamond tools, will be used to cut both

titanium alloy and cemented carbide, assessing the possibilities for use of these tools in relatively extreme cutting conditions and further increases in productivity. The diamond tools are single-crystal (SC) diamond and binderless nano-polycrystalline diamond (BL-NPD).

As the name suggests, these tools are carbon-based. SC diamond tools have a very high thermal conductivity of 1000–2200 W/(m·K) and a respectable hardness level of 70–120 GPa HV. Meanwhile, BL-NPD is made from nano-sized diamond crystals or particles with a thermal conductivity of 250–300 W/(m·K) and a slightly higher hardness of 120–140 GPa HV. The BL-NPD tool has been chosen in this study because the use of this material for tools is relatively new; it was first introduced in 2012 due to its very high hardness value. The SC diamond tool is tested against this tool to compare tool performance. The two tools are tested together in high-speed wet cutting of Ti-6Al-4V and together with other tools, using materials such as PCD (polycrystalline diamond) tools with binders and CBN (cubic boron nitride), in cutting three grades of cemented carbide (based on tungsten carbide, WC) that vary by binder percentage.

The performance of the BL-NPD tool is the main focus. This study is important to understand how this and other superhard tools react in severe cutting conditions involving difficult-to-machine materials at elevated cutting speed. Tool life, especially tool wear, will be analyzed. This in turn will help improve the selection of tools and their materials to cut these difficult-to-machine materials efficient and economically.

It is important that the performance of new types of binderless diamond tool is studied in order to establish the potentials of the new technology. The pursuit of the right tool for cutting of titanium alloys is vital here, due to the fact that machining these types of difficult-to-cut material is inducing high wearing on the tool. As the chemical conditions during the cutting of titanium produce the by-product titanium carbide, it is interesting to see how a pure-carbon-based tool (i.e., a diamond tool) behaves during cutting, especially in high-speed turning.

Research on tool performance in cutting of cemented carbide can provide a better understanding of the requirements for tools in this context. Comprehensive research on tool wear, cutting force, cutting temperature and surface roughness is needed to formalize efficient conventions for the cutting of cemented carbide. Study of a selection of ultra-hard tools is necessary in order to establish the best all-round tool for cutting different grades of cemented carbide.

In order to explore the unknowns of cutting ultra-hard and hard-to-machine materials, the study is constructed based on certain objectives. These are:

i. To assess the machinability of ultra-hard and hard-to-machine materials in severe conditions.
ii. To investigate the cutting properties of the selected ultra-hard tools on ultra-hard and hard-to-machine materials at high cutting speed.

iii. To investigate the influence of the physical properties of tools and workpieces on cutting performance components.

iv. To establish the best tool among those studied for cutting the aforementioned materials.

This study emphasizes the cutting performance of one of the hardest tool materials – diamond – in cutting two of the most difficult-to-machine materials, titanium alloy and cemented carbide. The cutting of cemented carbide will pit CBN against several diamond tools in a comparison of performance. Meanwhile, for titanium alloy, two distinct diamond tools will be tested against each other to find the best tool in the given cutting conditions.

1.6 Thesis Outline

In Chapter 2, a literature review is carried out on tool damage, cutting of cemented carbides and titanium alloy, and cutting temperature.

In Chapter 3, the basic principle of the two-color pyrometer is explained, as well as the temperature calibration set-up.

Chapter 4 presents the study on the cutting performance of the two distinct diamond tools in high-speed cutting of titanium alloy.

Chapter 5 presents the study on the cutting performance of CBN and diamond tools in cutting three grades of cemented carbide.

Chapter 6 presents the conclusion.

References:

[1]. M. P. Groover, Fundamentals of modern manufacturing; materials, processes and systems, Wiley, 4th ed. (2010).

[2]. S. Kalpakjian and S. R. Schmid, Manufacturing engineering and technology, Prentice Hall, New Jersey, 6th ed. (2010).

[3]. RMI Titanium Co. (2000), Titanium Alloy Guide [online]. Available: http://www.rtiintl.com/Titanium/RTI-Titanium-Alloy-Guide.pdf

[4]. T. Muguruma, M. Iijima, W. A. Brantley, T. Yuasa, H. Ohno, and I. Mizoguchi, "Relationship between the metallurgical structure of experimental titanium miniscrew implants and their torsional properties," Eur. J. Orthod., Vol. 33, No. 3 (2011), pp.293–297.

[5]. T. Childs, K. Maekawa, T. Obikawa and Y. Yamane, Metal Machining, Arnold, London, 1st ed. (2000).

[6]. C. Nath, M. Rahman and K. S., Neo, "Machinability study of tungsten carbide using PCD tools under ultrasonic elliptical vibration cutting," International Journal of Machine Tools and Manufacture, Vol. 49, No. 14 (2009), pp.1089–1095.

[7]. M. J. Kim, J. K. Lee, Y. Hwang, D. H. Cha, H. J. Kim, and J. H. Kim, "Experimental study of the diamond turning characteristics of tungsten carbide (Co 0.5%) when using a chamfered diamond bite," Journal of the Korean Physical Society, Vol. 61, No. 9 (2012), pp.1390–1394.

[8]. T. Miyamoto, J. Fujiwara, and K. Wakao, "Influence of WC and Co in cutting cemented carbides with PCD and CBN tools," Key Engineering Materials, Vol. 407–408 (2009), pp.428–431.

[9]. J. Fujiwara, K. Wakao and T. Miyamoto, “Influence of tungsten-carbide and cobalt on tool wear in cutting of cemented carbides with polycrystalline diamond tool,” International Journal of Automation Technology, Vol. 7, No. 4 (2013), pp.433–438.

[10]. E. O. Ezugwu, and Z. M. Wang, “Titanium alloys and their machinability – a review,” J. Material Processing Technology, Vol. 68 (1997), pp.262–274.

[11]. M. Rahman, Z.-G. Eang, and Y.-S. Wong, “A review on high-speed machining of titanium alloys,” JSME Int. J. (C), Vol. 49, No. 1 (2006), pp.11–20.

[12]. E. O. Ezugwu, “Key improvements in machining of difficult to cut aerospace superalloys,” Int. J. of Machine Tools & Manufacture, Vol. 45 (2005), pp.1353–1367.

[13]. F. Nabhani, “Wear mechanism of ultra-hard cutting tool materials,” J. Material Processing Technology, Vol. 115 (2001), pp.402–412.

[14]. E. Uhlmann, F. Sammler, J. Barry, J. Fuentes and S. Richarz, “Superhard Tools,” in CIRP Encyclopedia of Production Engineering, Heidelberg, Berlin, Springer-Verlag (2014), pp.1183–1188.

CHAPTER 2: OVERVIEW OF DIFFICULT-TO-MACHINE MATERIAL CUTTING

2.1 Tool

2.1.1 Tool Damage

Tool life is governed by the ability of a tool to slow or subdue tool wear leading to tool failure. Tool damage is classified in two distinct groups: wear and fracture. Wear is a phenomenon of material loss in contact with other material, which progresses continuously. Meanwhile, fracture is a sudden event of damage on a greater scale than wear; most of the time it is identified by chipping.

Tool damage is caused by three different kinds of factor: mechanical, thermal and adhesive. This is illustrated in **Fig. 2.1**. Mechanical damage relates to deterioration inflicted by abrasion, chipping, fracture and fatigue, and is less dependent on temperature than for example thermal damage such as plastic deformation, diffusion and chemical reactivity at the tool–workpiece interface. Here, the higher the cutting temperature, the higher the damage rate. Finally, adhesive damage occurs as the workpiece material welds itself to the tool cutting edge. This type of damage is also temperature dependent [1].

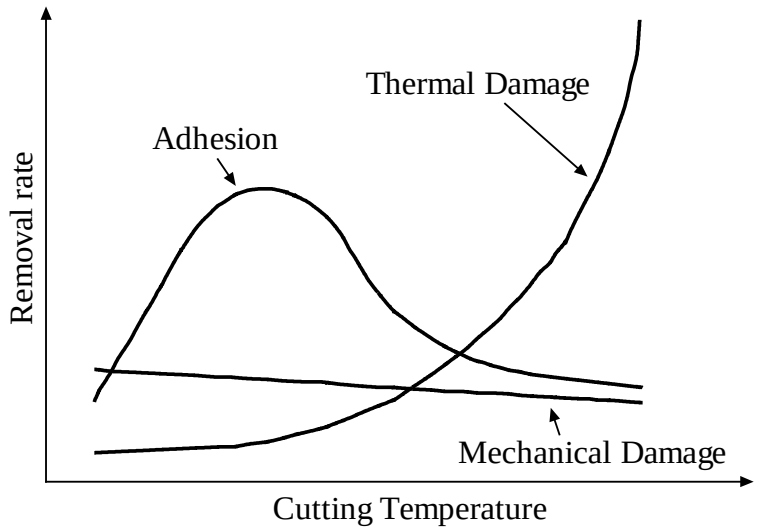

Fig. 2.1 Tool damage mechanism and cutting temperature

Wear and fracture are categorized according to size, which ranges from less than 0.1 µm to 100 µm with four different modes. Fracture that is more than 100 µm in size is considered to constitute a failure. An example of tool wear is shown in **Fig. 2.2** where wear and fracture can be clearly seen.

Abrasive wear is caused by the hard particles from the workpiece sliding on the tool. These hard particles come from the workpiece microstructure. Meanwhile, attrition is related to abrasion on a bigger scale. Basically, the hard particles cause microchipping on the tool as the workpiece and tool slide against each other during cutting. The tool incurs micro-fractures, which lead to microchipping on the tool surface. Lastly, chipping and fracture are caused by mechanical shock caused by fluctuations in the cutting force. This fluctuation is on a larger scale than the cutting force experienced by the tool during attrition [1].

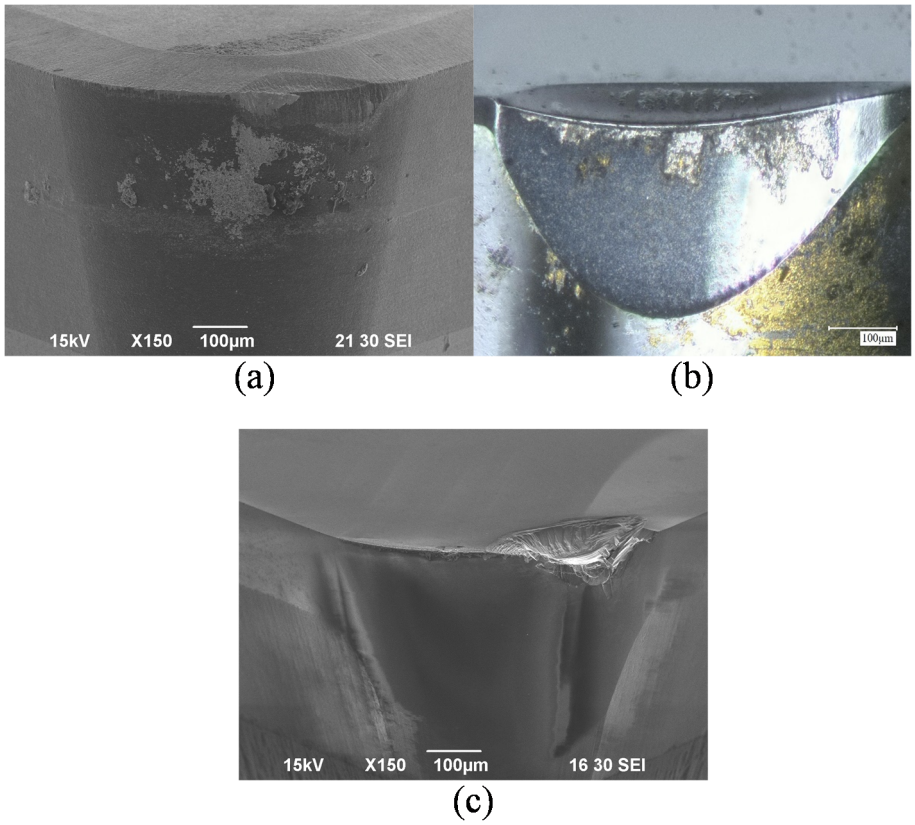

Fig. 2.2 (a) Adhesion and abrasive wear on CBN tool in cutting WC
(b) Diffusion wear on diamond tool in cutting of titanium alloy
(c) Fracture/failure on SC diamond tool in cutting WC.

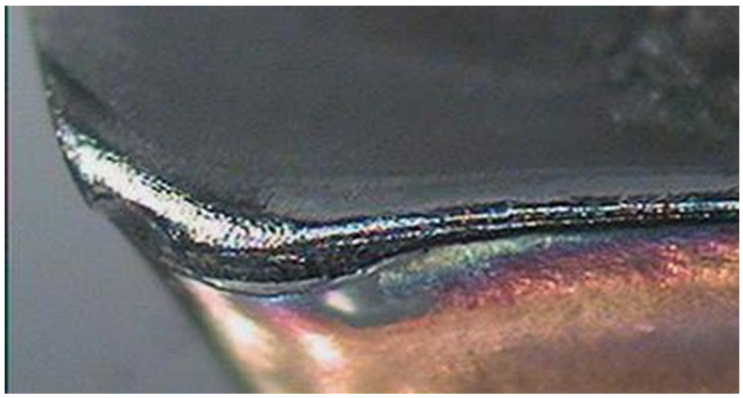

Fig. 2.3 Plastic deformation on cutting edge of a tool

Plastic deformation is thermal damage sustained by the cutting tool whereby the tool geometry changes at the cutting edge as the compressive stress increases. This type of wear is

shown in **Fig. 2.3**. This phenomenon occurs due to the high cutting temperature, reducing the hardness of the tool and weakening the tool structure [1].

Diffusion refers to the tool wear induced by high cutting temperature, with material from the tool being removed as it diffuses with the workpiece materials. This type of wear is shown in **Fig. 2.2 (b)**. It has been researched by several authors in the context of cemented carbide tools. Other types of material also have a tendency of diffusion, such as diamond, silicon nitride, ceramics and other materials used in machining steel. Carbon, silicon and nitrogen tend to diffuse with iron at elevated temperature. It is noted that diffusion wear can be slowed if a protective layer is applied onto the surface of the tool, also known as coating [1].

2.1.2 Tool life criteria

In industry, quantitative measurement of accuracy in products is related to surface roughness. Surface roughness is in turn related to tool life, especially in relation to tool wear. In order to maintain accuracy, certain limits have to be applied, in particular on tool life [1].

In order to set the tool life limit, tool wear has to be measured in the desired cutting conditions. This will prolong the cutting time, which is not economical. Observation of the surface roughness can be used, but there is no fixed value relation between tool wear and surface roughness in real-world cutting conditions with only one time observation. Another

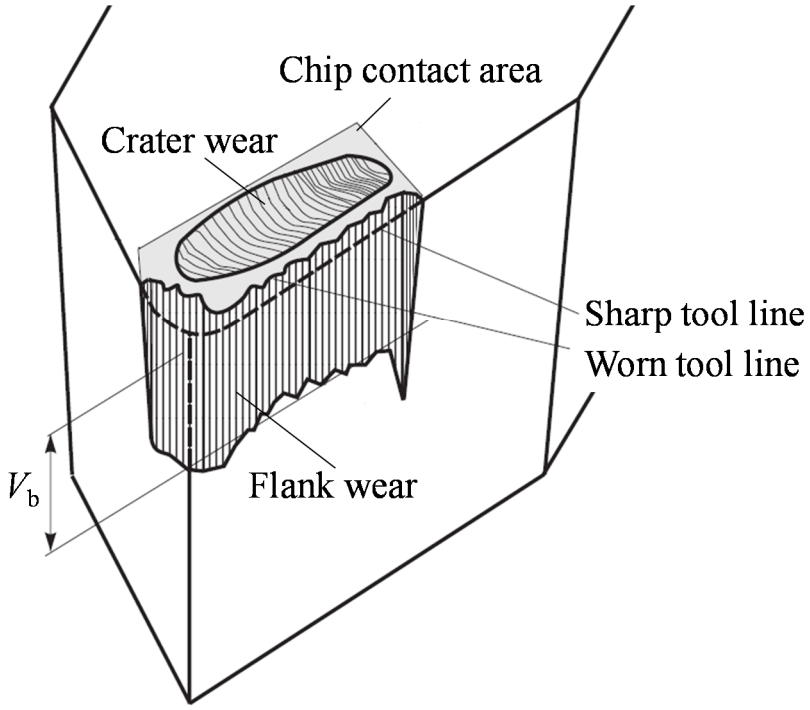

Fig. 2.4 Typical flank wear V_b on worn cutting tool

way of studying tool wear involves observation of the cutting chip, but this is difficult to apply, as measurement is difficult in mass production. The only effective way to determine optimal utilization of the tool in industry is to determine the number of components that can be produced with one tool or a set of tools. This approach can be used in a preliminary test, but the calculation must take into account the safety factor, which ultimately increases the manufacturing cost. [1]

Tool wear has been a fundamental component in assessing tool life in laboratory experiments, since it is easy to determine quantitatively in a lab setting. Flank wear has always been used as an indicator of surface roughness and accuracy. An example of flank wear width as used in tool life measurement is shown in **Fig. 2.4**. A standard measurement limit of 300

microns is applied. This value is increased such as to ensure the tool does not fail during the experiment, limiting the tool usage based on surface roughness and accuracy. Crater wear is another indicator for tool life. Surface roughness and accuracy are independent of this type of wear. Crater wear can therefore be seen as a better indicator of the machinability of diverse tool and workpiece combinations. Generally, crater depth between 0.05 and 0.1.mm can be seen as a sign of the end of tool life [1].

2.2 Material

2.2.1 Cutting of titanium Alloy

The aerospace and military industries have been main users of titanium alloys. These industries emphasize increased production and the creation of smaller components. High production means that material removal is also elevated. The quickest way to increase the production time is to increase the cutting speed.

Most of the research done in this area has shown that titanium alloys are indeed hard-to-machine materials. Higher cutting temperature with increased cutting speed is possible due to the low thermal conductivity of titanium alloy, as the thermal energy is concentrated at the tool–workpiece–chip interface. This ultimately increases manufacturing cost [2].

Titanium alloys have been identified as having a strong carbide-forming tendency. A semi-empirical classification produced in 1995 indicates that titanium on its own has a very

high affinity to form carbide in comparison to niobium, vanadium and molybdenum [3]. Titanium carbide (TiC) is a strong material in itself, and the forming of this material on the tool might help to cut the titanium alloy in the process.

One study has suggested that, in cutting of titanium-based material, tool candidates should show certain properties, as follows: the build-up edge formed in cutting is strong enough that the chip slides smoothly; chemical stability and low solubility with Ti; adequate hardness and mechanical strength [4, 5]. PCD tools possess these attributes.

As illustrated in **Table 2.1**, Pettifor formulated a relation indicator for four known metals with carbon [3]. This is described empirically showing the strength of reactivity with carbon using the enthalpy values of carbide formation. From this table, Pettifor concluded that the more negative the value of the carbide-forming enthalpy of a metal, the higher the affinity of that metal towards carbon.

Table 2.1 Enthalpies of formation of carbides

Metal	Carbide	ΔH kJ/mol
Titanium (Ti)	TiC	92
Niobium (Nb)	NbC	71
Vanadium (V)	VC	51
Molybdenum (Mo)	MoC	5

Meanwhile, another study pointed out that these indications might not be an issue using carbon-based tools, as the carbide formed might be compact and strong [6]. The authors concluded that, in cutting of titanium-based material, tool candidates have to show "strong interfacial bonding between the tool and the chip to create a seizure condition at the chip–tool interface, low chemical solubility in titanium to create a barrier to the diffusion flux of the tool constituents into the chip and sufficient hardness and mechanical strength to maintain physical integrity". At the time of writing, the PCD tool is acknowledged to possess all of these requirements.

It has been found that, at 500°C, almost all commercially available tools will react with titanium alloy [7]. The temperature gradient in cutting of titanium alloy is similar to that in cutting pure metal, though the alloying titanium does increase the cutting temperature [5]. This, in turn, limits the allowable cutting speed of the tool if tool life is to be improved. Another study suggested that very high temperature in cutting of titanium alloy is due to shorter cutting length in comparison to cutting steel [8]. These conditions might lead to the conclusion that tool candidates for titanium cutting should have high elevated-temperature hardness to overcome the high stresses from the cutting process, suitable thermal conductivity to reduce thermal shock, good chemical dormancy to subdue the chemical reaction with titanium, adequate toughness and fatigue resistance to endure chip segmentation, and high compressive, tensile and shear strength [7].

2.2.2 Cutting of cemented Carbide

Tungsten carbide (WC) is used in manufacturing industries, where its use is grouped in three major areas according to the hardness and the binder content: mold, dies and tools. Candidates for mold building have to able to withstand high-impact and -shock environments. Meanwhile, material candidates for dies are required to be able to withstand high impacts and have resistance to abrasion. Lastly, materials for tools are required to have even better resistance to abrasion.

CBN and PCD tools have been used in cutting of cemented carbide in previous research [9]. It has been reported that PCD tools have a higher tendency to build up adhesion, as the binder content decreases for better tool wear. CBN tools have the reverse effect. Both PCD and CBN tools experience abrasion/attrition wear. Another study has stated that cutting of cemented carbide is much more effective with the PCD tool, with higher binder content and smaller WC particles [3].

Cemented carbide is a hard and brittle material. The surface profile is therefore important in the production of molds and dies. Surface roughness has much to do with tool performance and how the cutting chip forms during cutting. For brittle materials, it is expected that the cutting chips produced are brittle and powdery in nature. Cutting brittle materials implies the tool does not cut smoothly, which can jeopardize tool life. Achieving ductility in cutting of cemented carbide has been an objective in several studies due to the surface quality that is guaranteed in ductile cutting of brittle materials. In conventional low-speed cutting,

researchers have achieved ductile cutting of cemented carbide ranging from 10 to 25% Co binder content at cutting speed of 15 m/min using CBN and PCD tools [10]. Meanwhile, in micromachining, researchers have achieved grinding surfaces on cemented carbide using ultrasonic elliptical vibration cutting [11]. On the other hand, cutting of cemented carbide with a very low binder content (Co binder at 0.5%) has been successfully executed to provide a near-diamond grinding-like surface finish with a chamfer diamond tool [12]. High-speed micromachining has suggested that turning with CBN tools could replace diamond grinding in processing cemented carbide [13].

Cutting temperature on cemented carbide is also being explored. One study on cutting of cemented carbide (22% Co binder content) with SC found that cutting temperature increases with cutting depth and cutting speed [14]. The cutting temperature of 550°C at the rake face of the tool gave a speed of 27 m/min with 0.5 mm depth of cut and feed rate of 0.1 mm/min. On the other hand, high-speed cutting of 100 m/min with a depth of cut of 2 µm yielded a lower cutting temperature of 180°C in cutting of cemented carbide with an SC diamond tool [15].

2.3 Cutting Temperature

Cutting temperature has been associated with cutting energy, influenced by the tool life. Almost 99% of the energy used during metal cutting is converted into thermal energy, with 1% of the remaining energy used in cutting [16]. Most of the thermal energy during cutting is transferred to the tool and the chip. One study concluded that thermal energy is directed to the tool if the thermal conductivity of the workpiece material is very low [11]. **Fig. 2.5** shows that, in the case of cutting of titanium alloy, 80% of the thermal energy goes to the cutting tool and the rest to the cutting chip. On the other hand, in cutting steel 50% of the thermal energy passes to the tool. Other studies have suggested that cutting speed (and cutting force in some cases) increases the cutting temperature [17-19]. This could be related to the theory of cutting energy/power shown below.

$$P_C = F_C V \tag{2.1}$$

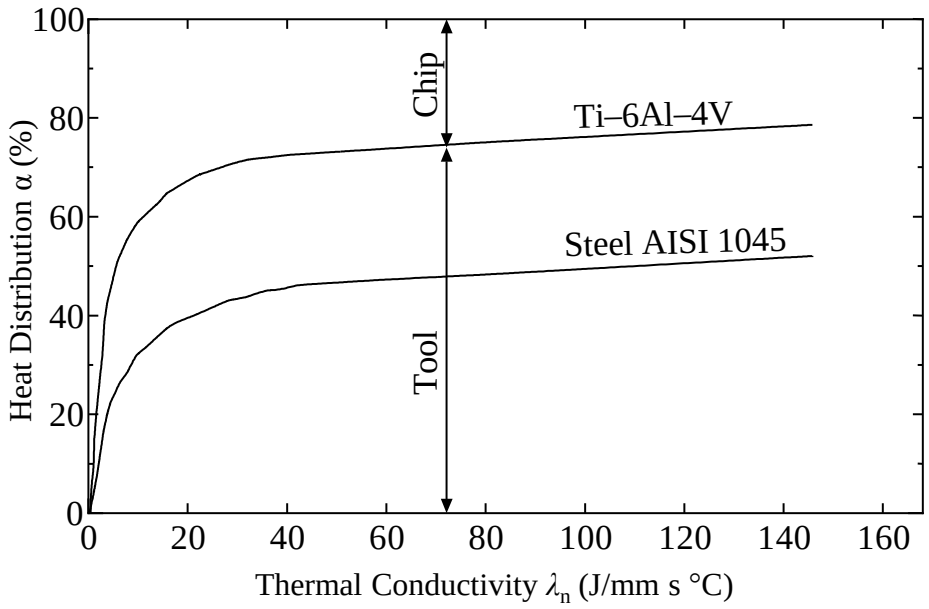

Fig. 2.5 Thermal distribution versus tool thermal conductivity in cutting Ti-6Al-4V and AISI 1045 steel [11]

It is shown here that F_c and V are components that raise the P_c value. Increased P_c indicates that the energy required for cutting is also increasing. This means that the relation between cutting speed, tool wear and cutting temperature is unbreakable.

Most cutting temperature studies [17-19] emphasize the cutting speed – probably based on the goal of decreasing the cutting time. These studies point out that the influence of cutting speed is much greater than that of depth of cutting. The feed rate is another factor influencing cutting temperature.

Studies have also pointed out that the thermal conductivity of the tool's material influences the cutting temperature. This is clearly shown in cutting of titanium alloy in wet conditions with PCD and CBN tools [18]. PCD tools emit a lower cutting temperature than the CBN tools, as they have a high thermal conductivity, and the coolant acts to absorb thermal energy during cutting. The ability of the material to disperse thermal energy is indicated by the thermal conductivity values; thus, the higher the thermal conductivity, the lower the cutting temperature. With lower cutting temperature, tool wear associated with thermal wear and even chemical wear will be reduced.

Depth of cut and feed rate have also been identified as factors influencing cutting temperature. These parameters can be used to increase or decrease the amount of material removed within a period of time. Increased depth of cut has been shown to increase cutting temperature in cutting of cemented carbide [7]. Increased feed rate has also been shown to

increase cutting temperature [18]. It is observed that in both parameters a by-product is cutting force, and it is this that influences cutting temperature.

2.4 Conclusion

In-depth studies have been done on the cutting of cemented carbide and titanium alloy. Effects of the cutting temperature of titanium alloy have been much explained and the search for the optimum high-speed cutting tool to withstand thermal wear is still on-going. Meanwhile, cutting-temperature studies in relation to cemented carbide are still lacking. Tool performance comparisons still lack variety, and hard turning studies have not been conducted.

It is clear that there are opportunities to adopt different perspectives on CBN and diamond tools in cutting of cemented carbide. There is also an opportunity to study the effect of high-thermal-conductivity tools in high-speed cutting of titanium alloy, looking at the effectiveness of the titanium carbide layer in reducing tool wear.

References:

[1]. Childs, T., Maekawa, K., Obikawa, T. and Yamane, Y., Metal Machining, Arnold, London, 1st ed., (2000).

[2]. Rahman M., Wang Z.G. and Wong Y.S., "A Review on High-Speed Machining of Titanium Alloys," JSME International Journal, Series C, Vol. 49, No. 1, (2006), pp.11–20.

[3]. Pettifor, D.G. Bonding and Structure of Molecules and Solids, Oxford University Press, (1995), pp.12–13.

[4]. Klocke, F., Konig, W., Gerschwiller K., "AMST'96 CISM Courses and Lectures 372" (E. Kuljanic ed.), Springer Verlag, Vienna (1996), pp.7–21

[5]. Trent, E.M. and Wright, P.K., Metal Cutting. 4th Ed. Butterworth-Heinemann, USA, (2000).

[6]. Kuljanic E., Fioretti M., Beltrame L., and Miani F., "Milling titanium compressor blades with PCD cutter," Annals of the CIRP, Vol. 47, Issue 1, (1998), pp.61–64.

[7]. Ezugwu E. O., Wang Z. M., "Titanium Alloys and Their Machinability – A Review," Journal of Material Processing Technology, Vol. 68, (1997), pp.262–274.

[8]. Nurul Amin, A.K.M., Ismail, A.F. and Nor Khairusshima, M.K., "Effectiveness of uncoated WC-Co and PCD insert in end milling of titanium alloy – Ti-6Al-4V," Journal of Material Processing Technology, (2007), pp.147–158.

[9]. Miyamoto, T., Fujiwara, J. and Wakao, K., "Influence of WC and Co in cutting cemented carbides with PCD and CBN tools," Key Engineering Materials, Vol. 407–408, (2009), pp.428–431.

[10]. Nath C., Rahman M., and Neo K. S., "Machinability study of tungsten carbide using PCD tools under ultrasonic elliptical vibration cutting," International Journal of Machine Tools and Manufacture, Vol. 49, No. 14, (2009), pp.1089–1095.

[11]. Kim M. J., Lee J. K., Hwang Y., Cha D. H., Kim H. J., and Kim J. H., "Experimental study of the diamond turning characteristics of tungsten carbide (Co 0.5%) when using a chamfered diamond bite," Journal of the Korean Physical Society, Vol. 61, No. 9, (2012), pp.1390–1394.

[12]. Liu K., Li X., and Rahman M., "Characteristics of high speed micro-cutting of tungsten carbide," Journal of Materials Processing Technology, Vol. 140, No. 1–3, (2003), pp.352–357.

[13]. Moriwaki, T., Tsurimoto, S. and Ueda, T., Cutting temperature in diamond turning of tungsten carbide, Proceedings of the 13th euspen International Conference, Vol. 2, (2013), pp.43–46.

[14]. Yui, A., Matsuoka, H., Okuyama, S., "Precision cutting of tungsten carbide using a mono-crystal-diamond tool – Measurement of cutting temperature," Proceedings of the 10th Anniversary International Conference of the European Society for Precision Engineering and Nanotechnology, euspen 2008, (2008), Vol. 2, pp.77–80.

[15]. Rao P. N. Manufacturing Technology, Metal Cutting and Machine Tools. McGraw-Hill, (2002).

[16]. Okada M., Hosokawa A., Tanaka R., and Ueda T., "Cutting performance of PVD-coated carbide and CBN tools in hardmilling," Int. J. Machine Tools & Manufacture, Vol. 51, No. 2, (2011), pp.127–132.

[17]. Nishimoto H., Tanaka R., Hosokawa A., Ueda T., and Furumoto T., "Development of tool edge temperature measurement method in wet cutting," J. Advanced Mechanical Design, Systems, and Manufacturing, Vol. 6, No. 6, (2012), pp.916–922.

[18]. Okada M., Hosokawa A., Asakawa N., and Ueda T., "End milling of stainless steel and titanium alloy in an oil mist environment," Int. J. Advanced Manufacturing Technology, Vol. 74, No. 9–12, (2014), pp.1255–1266,

CHAPTER 3: BASIC PRINCIPLES OF TWO-COLOR PYROMETER

3.1 Introduction

Thermal energy is closely related to the cutting energy needed to cut the workpiece in any given conditions. The thermal energy is a by-product of the cutting energy used to shear the workpiece at the primary shear zone, as well as friction at the tool–chip and tool–workpiece interfaces. This is clearly shown in dull or worn tools, so cutting temperature can be used as an indicator of tool life.

Cutting temperature has been determined by several methods, such as thermocouple and radiation (pyrometer) methods [1]. Radiation techniques have been seen as better measurement methods in cutting, as they have the ability to measure in very tight spaces, such as those found in this context [2-5]. This type of temperature measurement technique uses two or more infrared sensitive sensors, which give a voltage output whenever they sense infrared radiation. The utilization of two or more such sensors in tandem solves the emissivity problem during temperature measurement.

3.2 Thermal Radiation

Materials are continuously emitting electromagnetic radiation as atoms and molecules detach due to internal energy. Electromagnetic radiation wavelengths can be tens of meters (basically the length of a radio wave) or as small as 1 µm or below (the wavelength of cosmic rays). This study only considers thermal radiation, which is emitted by all elements or substances in the universe.

Fig. 3.1 shows the wavelength and frequency domains of thermal radiation, showing the respective positions on the electromagnetic spectrum. The thermal radiation domain is positioned approximately between 0.1 and 100 mm. The visible range is situated roughly between the wavelengths of 0.4 and 0.7 mm. As wavelengths increase, the thermal radiation domain can be divided into three consecutive sub domains: the ultraviolet range, the visible range, and the infrared range.

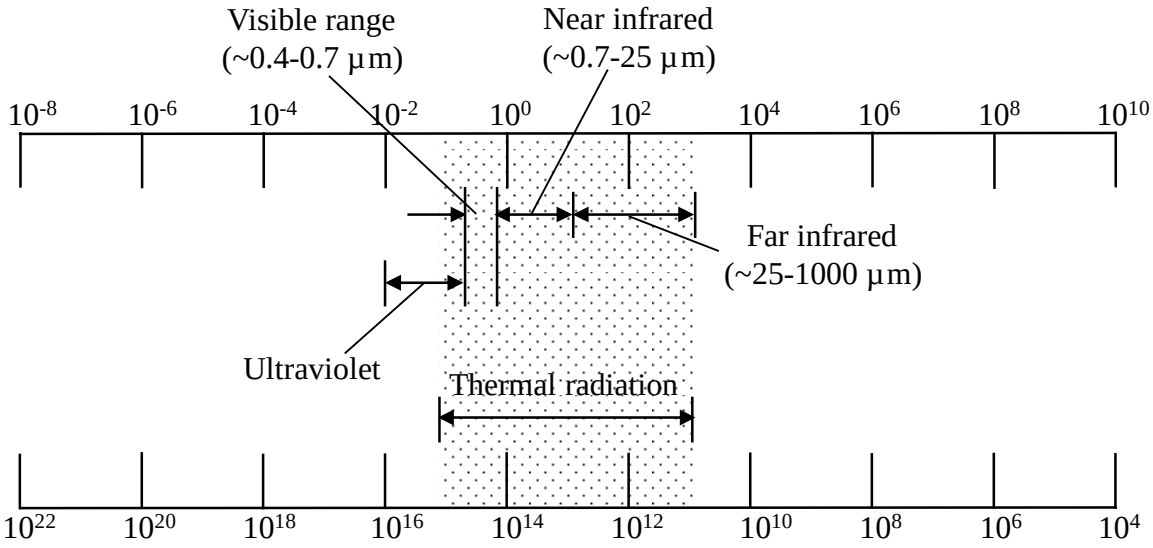

Fig. 3.1 Wavelength and frequency domains of thermal radiation and positions on the electromagnetic spectrum

The intensity of thermal radiation, *I*, is defined as the radiant energy per unit of time per unit of solid angle per unit of area of the emitter, projected normally to the line of view of the receiver from the radiation element [6]. Quantum arguments of Planck [7], verified experimentally, have shown that for a blackbody the spectral distributions of hemispherical emissive power and radiant intensity in a vacuum are given as a function of wavelength l and the blackbody's absolute temperature *T*. The monochromatic intensity of blackbody radiation, $I_{b\lambda}$, has been identified as:

$$I_{b\lambda}(\lambda,T)=\frac{2hc^2}{\lambda^5\{\exp(hc/k\lambda)-1\}} \tag{3.1}$$

where:

k =1.3805 x 10^{-23} J/K is the Boltzmann constant,

h =6.6256 x 10^{-34} J.s is the Planck constant,

c =3x10^8 m/s is the speed of light in a vacuum.

The unit of $I_{b\lambda}$ is W/(m^3.sr), the number of Watts per unit of wavelength (W); the unit of the area normal to the ray is m^2, and the unit of the solid angle is sr, steradian. The total intensity of blackbody radiation, I_b, is acquired by integrating the monochromatic intensity, $I_{b\lambda}$, over the entire radiation spectrum:

$$I_b(T)=\int_\lambda I_{b\lambda}(\lambda,T)d\lambda \tag{3.2}$$

The total intensity represents the energy conveyed by the ray (in a certain direction) per unit of time, solid angle, and area normal to the direction of the ray.

By multiplying π by $I_{b\lambda}$, the monochromatic hemispherical emissive power of the black surface, $E_{b\lambda}$, can be obtained as:

$$E_{b\lambda}(\lambda,T)=\pi I_{b\lambda}(\lambda,T)=\frac{C_1}{\lambda^5\{\exp(C_2/\lambda T)-1\}} \tag{3.3}$$

For which the values of the constants C1 and C2 can be deducted from equation (3.1):

$$C_1=2\pi hc^2=3.742\text{x}10^{-16}\ \text{W.m}^2 \tag{3.4}$$

$$C_2=hc/k=1.439\text{x}10^{-2}\ \text{m.K} \tag{3.5}$$

The unit of $E_{b\lambda}$ is W/m^3, which is the energy per unit of time, wavelength, and surface area.

Fig. 3.2 shows the $E_{b\lambda}(\lambda,T)$ function for several temperatures. The monochromatic emissive power in shown to intensely increase with the absolute temperature. A maximum $E_{b\lambda}$

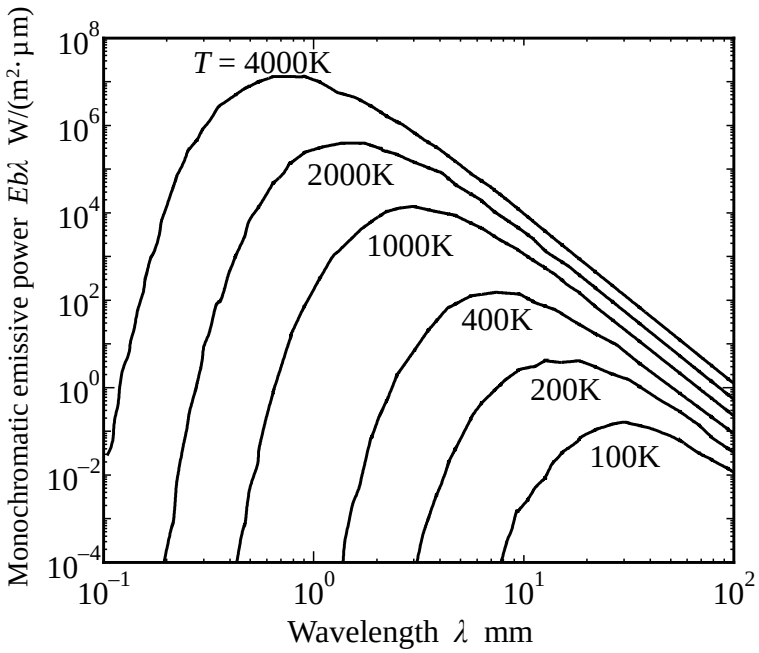

Fig. 3.2 Radiant energy of a black body

value is registered at a characteristic wavelength for each temperature by solving $\partial E_{b\lambda}/\partial\lambda = 0$ in conjunction with equation (3.8):

$$\lambda T = 2.898 \text{ x } 10^{-3}\ \text{m}\cdot\text{K} \tag{3.6}$$

This is known as Wien`s displacement law [8], and describes the locus of the $E_{b\lambda}$ maximum, represented by a straight line in the logarithmic field, as shown in **Fig. 3.2**. As seen here, the wavelength of maximum $E_{b\lambda}$ varies inversely with the absolute temperature, leading to the conclusion that the bulk of the energy emitted by a blackbody shifts to gradually shorter wavelengths.

In conclusion, the monochromatic emissive power $E_{b\lambda}$ represents the heat flux emitted from a surface area along all the rays intersected by the hemisphere, per unit of wavelength interval. The total hemispherical emissive power of blackbody E_b can be calculated by integrating equation (3.2) over all the wavelengths of the radiation spectrum:

$$E_b(T) = \int_{\lambda} E_{b\lambda}(\lambda, T)\, d\lambda \tag{3.7}$$

which is the Stefan–Boltzmann law [8, 10];

$$E_b(T) = \sigma T^4 \tag{3.8}$$

where σ = 5.6697 x 10-8 W/(m2.K4) is the Stefan–Boltzmann constant.

From equations (3.3) and (3.8), it is clear that the total energy radiated from a surface depends on the temperature of the surface; therefore, the temperature of an object can be determined by measuring the total energy radiated. The infrared radiation pyrometer is based on this phenomenon. A blackbody has both an ideal surface and an 'actual' surface; the actual object has a total emissive power that is less than the emissive power radiating from the blackbody. The emissive power of this 'real' surface is highly affected by the emissivity of the surface. The emissivity is defined as a ratio of the total emissive power of the surface to that of a blackbody at the same temperature. This problem led to the development of the two-color pyrometer that will be used in this study.

3.3 Basic Principles of Two-Color Pyrometer

The diagram of the pyrometer is shown in **Fig. 3.3**. The pyrometer consists of optical fibers, sensors and operational amplifiers that have been arranged to collect, channel and change the thermal radiation (on the infrared spectrum) to an electrical signal that is recorded

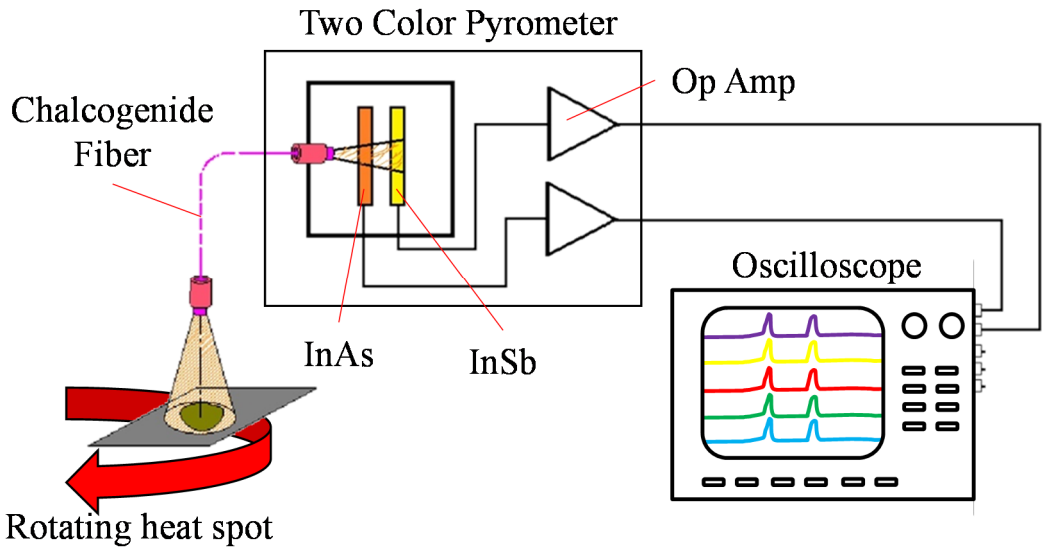

Fig. 3.3 Fundamental diagram of two-color pyrometer with optical fiber

on an oscilloscope. Two infrared sensors/detectors are used to detect different spectra of wavelength.

In cutting, thermal energy is emitted by the tool. In this study, the target area is the flank face near to the cutting edge. The thermal energy is emitted on the infrared spectrum and is collected by the end of the chalcogenide fiber. This infrared ray will be transmitted through the fiber to the two-color detector. The detector consists of two types of detector assembled in a sandwich configuration, which convert the infrared ray to electrical signals. These signals are recorded by an oscilloscope.

3.3.1 Components of Two-color Pyrometer

It is essential to perform proper selection of optical fiber, infrared detector and other important components of the pyrometer in order to ensure the accuracy and functionality of the built pyrometer. In this section, the main components of the two-color pyrometer will therefore be discussed in detail.

3.3.1.1 Optical fiber

There are two major groups in the production of optical fiber: multimode and single-mode. Multimode fiber is categorized into two further types: step-index and graded-index. In graded-index fiber, the core refractive index is differentiated by the radial distance originating from the center of the fiber in the form of a function.

In this study, step-index NSG chalcogenide optical fiber is used to build the pyrometer. **Fig. 3.4** illustrates the structure of the step-index optical fiber. Since the core's refraction index, n_1, is higher than the index of the cladding's refraction, n_2, the ray that enters the core at a smaller angle than the critical angle is guided along the fiber. The critical angle (minimum angle for total internal reflection) is regulated by the index of the refraction variance of the core and cladding materials as follows:

$$\sin\phi_c = \frac{n_2}{n_1} \tag{3.9}$$

From Snell's law:

$$n_0 \sin\xi_m = n_1 \sin\left(\frac{\pi}{2} - \phi_c\right) \tag{3.10}$$

The rays that reach the boundary at a low angle are diverted from the core into the cladding, and there is no light transfer along the fiber. The acceptance angle of the fiber is influenced by

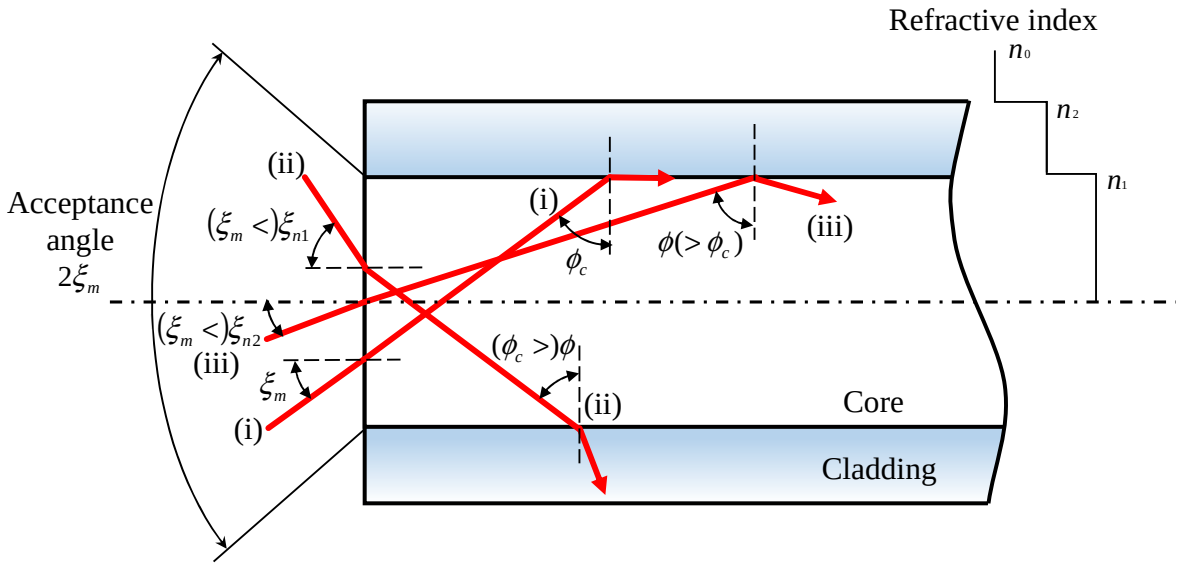

Fig. 3.4 Experimental set-up of internal turning

the critical angle, described as a numerical aperture (NA). The NA is defined as follows, deriving from equations (3.9) and (3.10):

$$n_0 \sin \xi_m = n_1 \left\{ 1 - \left(\frac{n_2}{n_1} \right)^2 \right\}^{1/2} = \sqrt{n_1^{\,2} - n_2^{\,2}} = NA \tag{3.11}$$

A high value of NA will allow the light to transmit through the fiber near to the axis and at numerous angles, permitting efficient coupling of light transmitted into the fiber. On the other hand, it will also prompt increased dispersion of rays at different angles, which acquire different path lengths and different times of transmission through the fiber. The ratio of the change in the refractive index of the core and cladding is called a relative refractive index difference, and is described as follows:

$$\Delta = \left(\frac{n_1 - n_2}{n_1} \right) \tag{3.12}$$

As the refractive index for the atmosphere is n_0=1, the maximum acceptance angle ξ_m of the optical fiber can be found as follows:

$$\xi_m = \sin^{-1}(NA) \tag{3.13}$$

3.3.1.1.1 Characteristics of Optical Fiber

Within a continuous fiber, structural and chemical imperfections affecting absorption and scattering contribute to transmission loss. Absorption loss due to elements such as Cr, Mn, Co, Fe, Ni, Cu, and V inside the fiber material has been detected previously [11]. These elements, especially Cr and V, affect loss at $\lambda > 0.8$ μm. In this study, this type of absorption loss is insignificant due to the satisfactory reduction of the impurity. Meanwhile, density fluctuation in the fiber may also cause transmission loss, as all transparent materials have

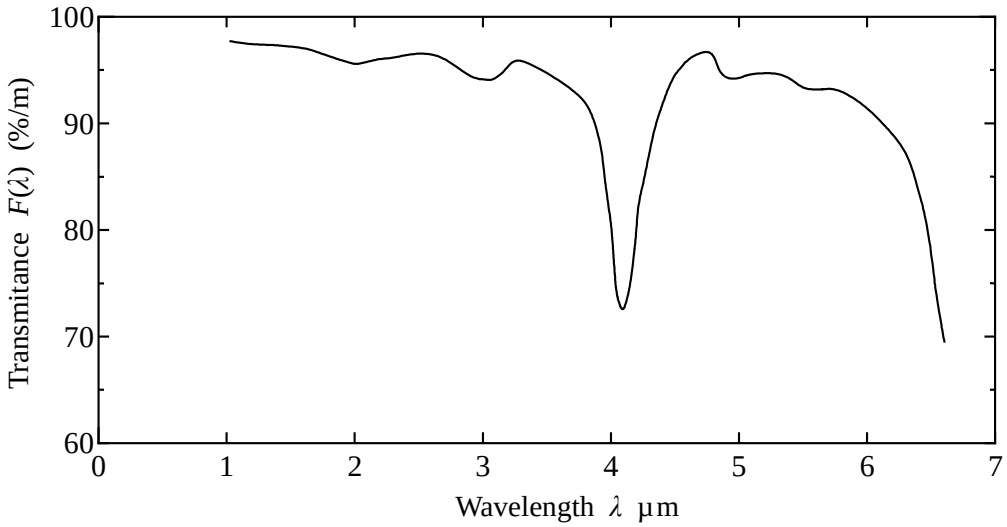

Fig. 3.5 Spectral transmittance of chalcogenide glass fiber

Table 3.1 Specifications of chalcogenide glass fiber

Core diameter [μm]	d_c	400
Numerical aperture	*NA*	0.4
Refractive index distribution		Step type
Acceptance angle [degree]	ξ_m	23.58°
Transmission wavelength range [μm]		1 to 6.6

intrinsic spatial density fluctuation [11]. This fluctuation affects the refractive index fluctuation and subsequently the Rayleigh scattering. Curvature of the fiber routes allows an acceptable level of radiation loss in some modes. Geometrical non-uniformity at the core–cladding boundary also contributes to transmission loss. The surfaces at both ends of the optical fiber have to be smooth in order to inhibit this; these surfaces are therefore polished.

The NSG chalcogenide optical-fiber wavelength is shown in **Fig. 3.5**. It can be seen that it is possible to measure temperatures as low as 300ºC using this optical fiber. **Table 3.1** shows the detailed characteristics of the NSG chalcogenide glass fiber.

3.3.1.1.2 Measuring area of the optical fiber

Fig. 3.6 (a) shows the schematic illustration of measuring area at the incidence face of the optical fiber. The fiber is placed perpendicular to and at a distance of t from the object. d_s is the diameter of the target area. **Fig. 3.7 (b)** shows the relationship between measuring distance, t and diameter of the target area, d_s. It can be seen that by increasing the measurement distance, the target diameter can also be increased. It has been shown previously that the measuring distance does not influence the output of the two-color pyrometer [5]. In this study, the measuring distances were fixed at 0.5 mm, yielding a target-area diameter of 0.74 mm.

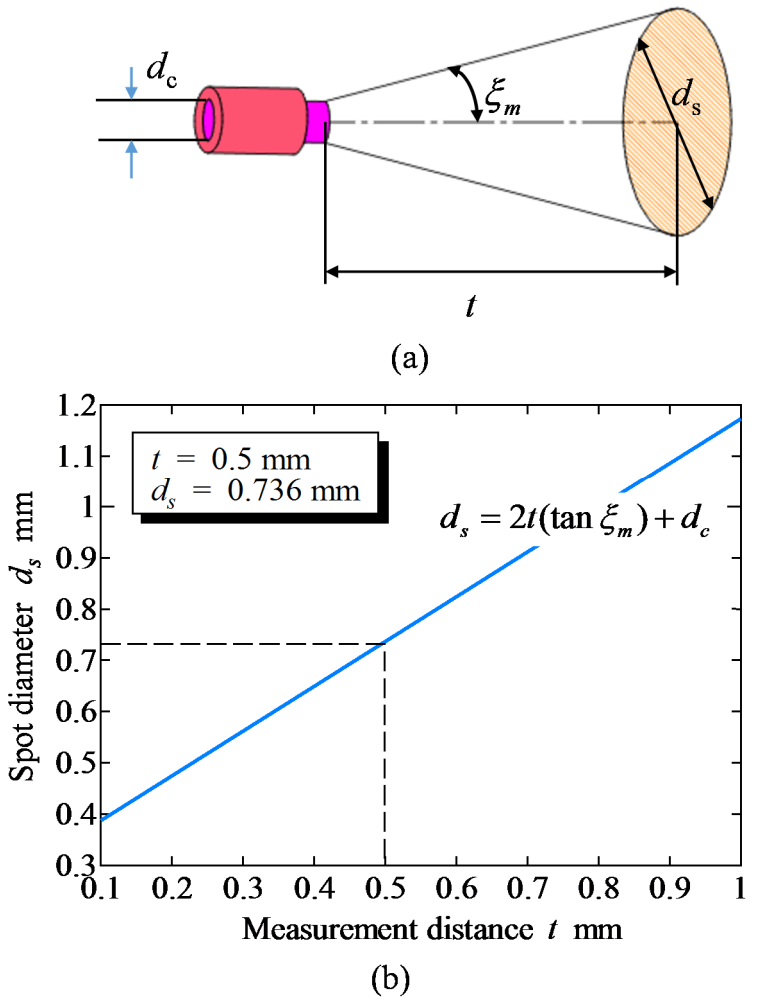

Fig. 3.6 (a) Schematic diagram of measurement area; (b) relations between measurement area and measurement distance

3.3.1.2 Pyrometer

Two types of infrared detector are available: thermal, and photon. Thermal detectors convert radiated power from infrared rays into measured parameters without any conversion. The bolometer [12], Gollay cell [13] and thermopile [14] are categorized as thermal detectors. On the other hand, photon detectors respond to incident radiation electronically. These types

of detector respond much faster, as the radiation does not need to come from an object that is only being heated.

Photon detectors are subdivided into two distinct types: photoconductive and photovoltaic. These detectors differ in their construction. As suggested in the name, photoconductors are fundamentally poor conductors, whose conductivity is improved with the presence of photon-generated carriers; meanwhile, photovoltaic detectors are diodes that generate an electromotive force when photons are detected. The advantages of photovoltaic detectors over photoconductive detectors are improved theoretical limit to signal-to-noise ratio, modest biasing and more accurately predictable responsivity. Photovoltaic detectors are more delicate in comparison to photoconductors, however, as they are more vulnerable to electrical discharge and physical damage during handling.

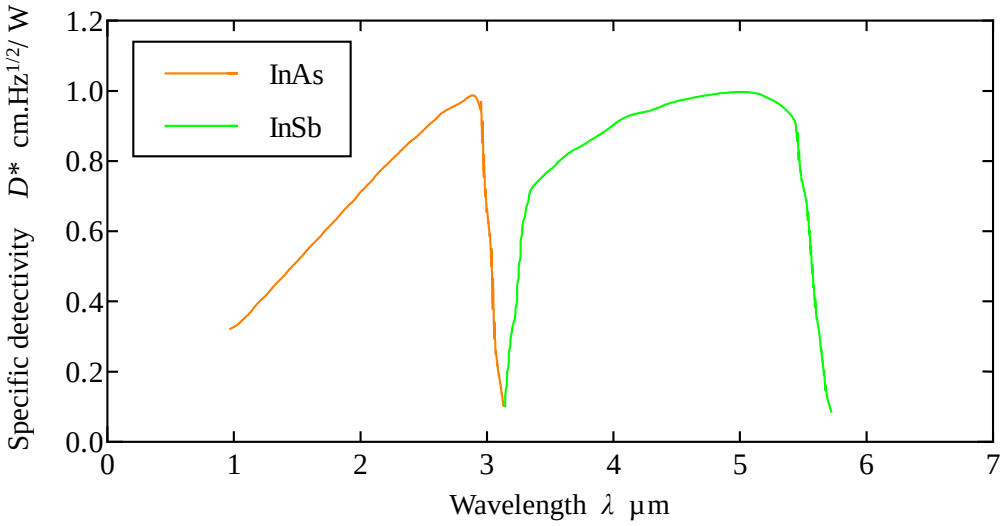

Fig. 3.7 Spectral transmittance of InAs and InSb detectors

In this study, Indium Arsenide (InAs) and Indium Antimode (InSb), are used as infrared detectors. InAs is used in photovoltaic detectors and InSb in photoconductive detectors. These detectors are mounted in a sandwich formation with InAs positioned in front of InSb. The range of detectable wavelength for the sensors' configuration is 1 µm to 5.5 µm; the range of InAs is from 1 µm to 3 µm, with the rest of the wavelength covered by InSb. **Fig. 3.7** visually explains the spectral transmittance of pyrometer sensors. It is crucial that these sensors are kept at a low operational temperature of -60°C using a Peltier cooler.

The configuration of the chalcogenide fibers and detectors used in in the experiment is used to measure the temperature from the desired area. Due to the range covered by the chalcogenide fiber and the InAs/InSb detectors, the pyrometer range is between 1 and 5.5 µm. This set-up, which gives a flat response from 10 Hz to 400 Hz, is suitable for use in turning, with a good degree of accuracy. This pyrometer assembly has been successfully implemented in cutting and milling.

3.3.1.3 Amplifier

The infrared detectors built into the two-color pyrometer used in this study have a desired response time that is suitable for internal cutting at low and high speed. For this purpose, the response performance of the conversion amplification circuit is required to be higher than the response speed of the infrared detectors. **Fig. 3.8** shows the schematic diagram of the amplifier for the InAs and InSb cells. The output current from the photovoltaic cell (InAs) is

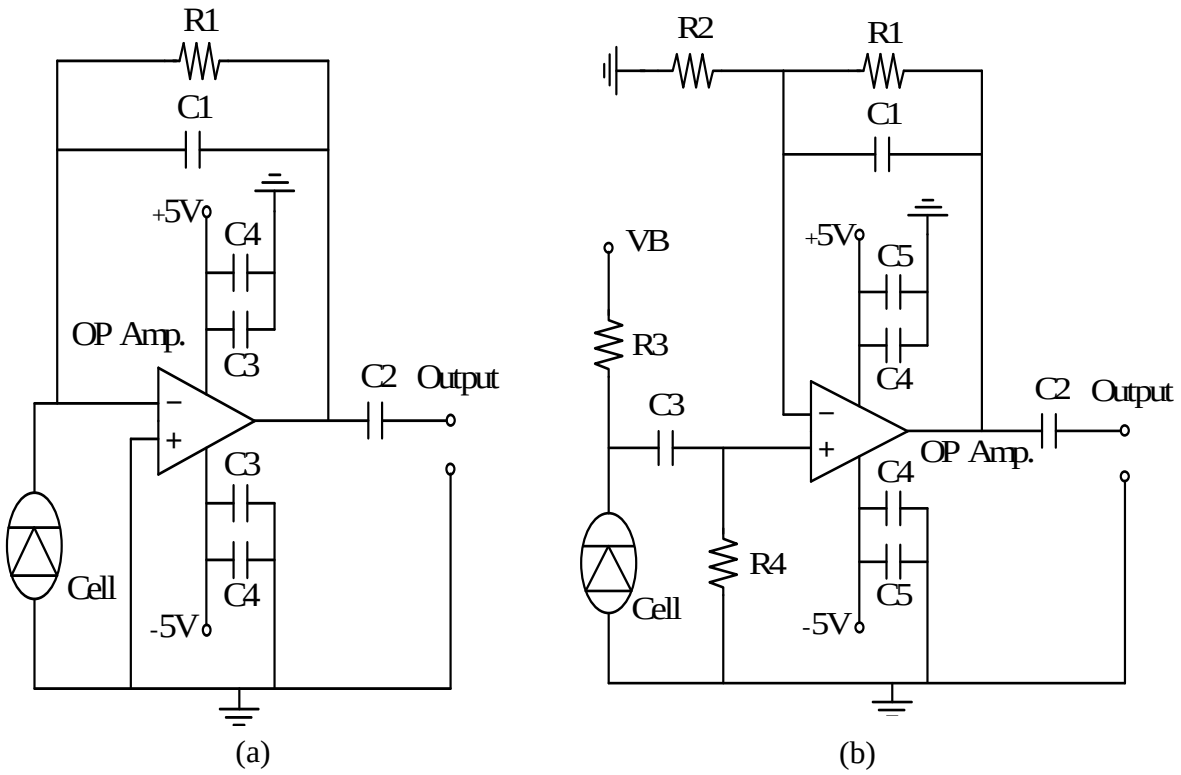

Fig. 3.8 Amplifier circuits of (a) InAs and (b) InSb detectors

converted into voltage and amplified with the conversion amplification circuit, as shown in **Fig. 3.8.** Because the InSb detector cell is a photoconductor cell **(a)**, the resistance of the InSb cell is amplified using the amplifier **(b)**.

3.3.2 Pyrometer calibration

In measuring temperature using infrared signals, emissivity is encountered as a problem. To address this, two types of infrared sensor are used to measure the temperature from the infrared radiation, rather than just one. In this study, two signals are recorded by the oscilloscope. As mentioned above, the two-color detector comprises two distinct sensors: InAs acts as a photovoltaic sensor, positioned in front of InSb, acting as a photo-conductive sensor.

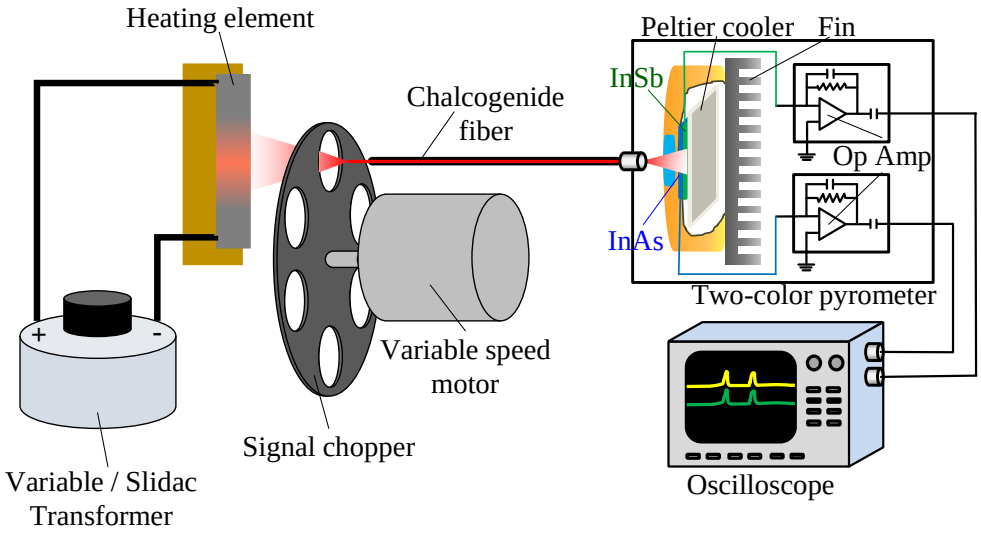

Fig. 3.9 Schematic set-up of pyrometer calibration

These detectors produce two electrical signals in millivolts that will be used to calculate the tool flank-face temperature. This successfully avoids the emissivity problem.

In theory, this type of pyrometer is capable of measuring the total energy radiated from the surface of the target object. Here, the object is presumed to have a blackbody surface at uniform temperature with no losses to the surroundings. The calibration curve is based on the relative sensitivity of the pyrometer. This calibration curve is formulated based on the following formula:

$$\Lambda_{InAs/InSb} = \frac{\Lambda_{InAs}}{\Lambda_{InSb}} = \frac{\int_{\lambda_1}^{\lambda_2} \omega_1 \varepsilon_1(\lambda,T) E_{b\lambda}(\lambda,T) F(\lambda) D_{InAs}(\lambda) d\lambda}{\int_{\lambda_4}^{\lambda_3} \omega_2 \varepsilon_2(\lambda,T) E_{b\lambda}(\lambda,T) F(\lambda) D_{InSb}(\lambda) d\lambda} \tag{3.14}$$

where:

$E_{b\lambda}(\lambda,T)$: the spectral emissive power of a blackbody

$\varepsilon_1(\lambda,T)$ and $\varepsilon_2(l,T)$: emissivity of the object

ω_1, ω_2 : constant

$F(\lambda)$: spectral transmittance of optical fiber

$D_{InAs}(\lambda)$ and $D_{InSb}(\lambda)$) : spectral transmittance of detector cell.

This calibration curve is then verified experimentally and compared to the theoretical curve.

In relating the voltage ratio to the temperature value, it is important to calibrate the detectors. This is done by using the heating element (SiC), which is treated as a heating

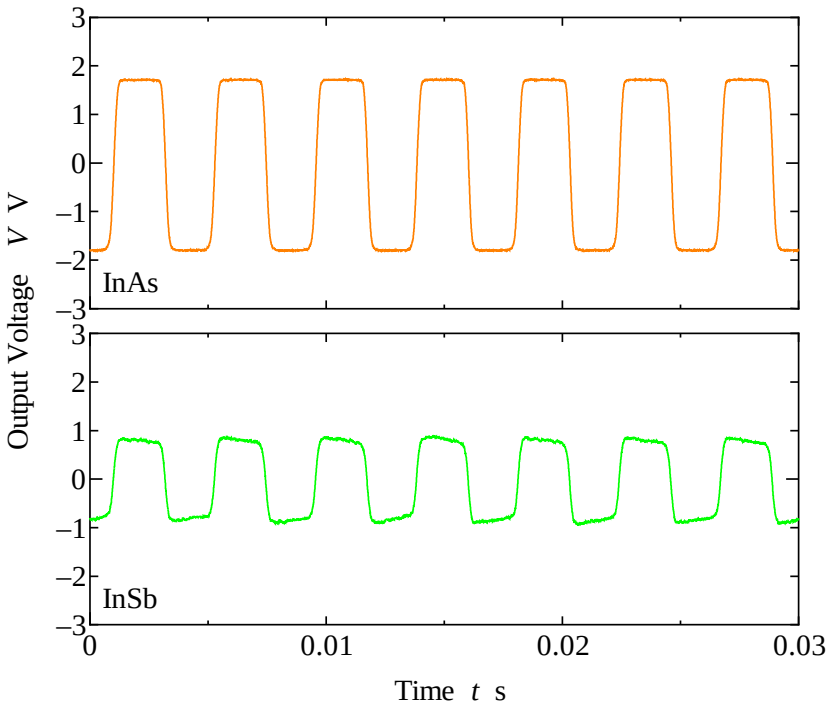

Fig. 3.10 Typical oscilloscope signal output

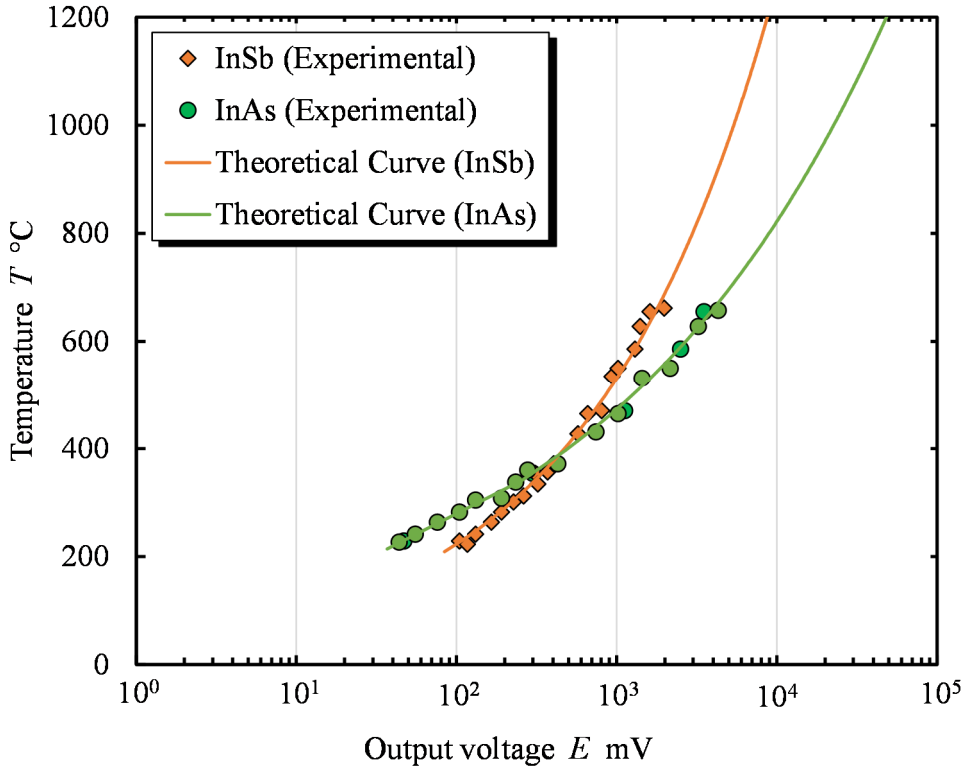

Fig. 3.11 Relation between InAs/InSb voltage and object temperature

blackbody. **Fig. 3.9** shows the set-up for pyrometer calibration. This set-up calibrates the output voltage from the InAs/InSb detector and tests it against the theoretical curve obtained from the theoretical equation.

The InAs and InSb signals recorded by the oscilloscope are shown in **Fig. 3.10**. The temperature readings from the thermocouple is then plotted against both detectors' output signals. These in turn are compared with the theoretical curves shown in **Figs. 3.11** and **3.12**. It is found that the readings satisfy the theoretical curve; good results have therefore been obtained. This method of calibration has been used in previous studies involving steel, sintered metal and titanium alloy [15].

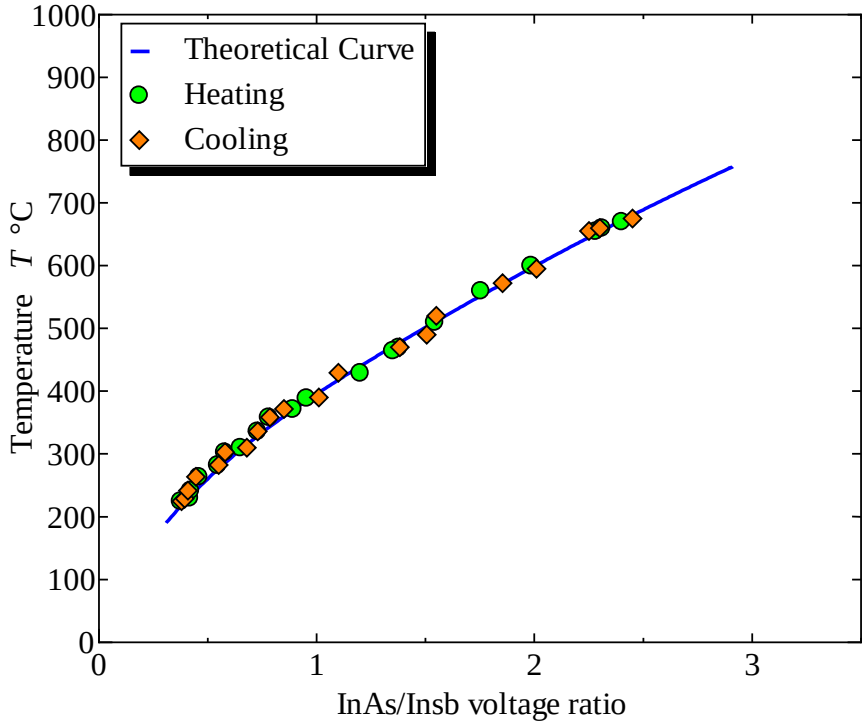

Fig. 3.12 Relation between InAs/InSb output voltage ratio and object temperature.

3.4 Conclusion

This chapter has explained the temperature measurement technique that has been used in this study. The pyrometer set-up has been designed and proven to be able to measure temperature, even in wet conditions. The conclusions of this chapter are as follows.

1. Temperature measurement is obtained using the voltage ratio of the InAs and InSb outputs. Emissivity is not a problem here and can be ignored. Calibration is relatively easy once the theoretical curve has been determined.
2. A pyrometer assembly consisting of chalcogenide fiber and InAs and InSb detectors can be used for this study. Based on previous research, this pyrometer has a minimum detectible temperature of 200°C

References:

[19]. Childs, T., Maekawa, K., Obikawa, T. and Yamane, Y., Metal Machining, Arnold, London, 1st ed. (2000).

[20]. T. Ueda, M. Sato, A. Hosokawa, and M. Ozawa, "Development of infrared radiation pyrometer with optical fibers – Two-color pyrometer with non-contact fiber coupler," CIRP Annals Manufacturing Technology, Vol. 57, No. 1, (2008), pp.69–72.

[21]. M. Al Huda, K. Yamada, A. Hosokawa, and T. Ueda, "Investigation of Temperature at Tool-Chip Interface in Turning Using Two-Color Pyrometer," Journal of Manufacturing Science and Engineering, Vol. 124, No. 2, (2002), p.200.

[22]. T. Ueda, M. Al Huda, K. Yamada, and K. Nakayama, "Temperature measurement of CBN tool in turning of high hardness steel," CIRP Ann. – Manuf. Technol., Vol. 48, No. 1, (1999), pp.63–66.

[23]. T. Ueda, A. Hosokawa, K. Oda, and K. Yamada, "Temperature on Flank Face of Cutting Tool in High Speed Milling," CIRP Annals – Manufacturing Technology, Vol. 50, No. 1, (2001), pp.37–40.

[24]. Chyssoloris, G., "Heat Transfer and Fluid Mechanics for Laser Machining," in Laser Machining; Theory and Practice, New York, Springer, (1991), pp.92–195.

[25]. Planck, M., "Distribution of energy in the spectrum," Ann. Phys., 4(3) (1901), pp.553–563.

[26]. Wien, W., "Temperatur und Entropie der Strahlung," Ann. Phys., 52(2) (1894), pp.132–165.

[27]. Boltzmann, L., “Ableitung des stefan’schen Gesetzes betreffend der Abhangigkeit der Waermestrahlung von der Temperatur aus der electromagnetischen Lichttheorie,” Ann. Phys., 22(3), (1884), pp.291–294.

[28]. Stefan, J., “Ueber die Beziehung zwischen der Waermestrahlung und der Temperatur,” Sitz-Ber. Akad. Wiss. Wien, 79, (1879), pp.391–428.

[29]. Okoshi, T., Optical fiber, New York, Academic Press (1982).

[30]. Strong, J. and P.W.Lawrence. Jr., “Bolometer theory,” Appl. Opt., 7, (1968), p.49.

[31]. Golay, M.J.E., “A pneumatic infra-red detector,” Review of Scientific Instruments, 18, (1947), p.357.

[32]. Stevens, N.B., “Radiation thermopiles,” Vol. 5, New York, Academic Press, (1987), p.287.

[33]. Nishimoto, H., Tanaka, R., Hosokawa, A., Ueda, T., and Furumoto, T., “Development of Tool Edge Temperature Measurement Method in Wet Cutting,” Journal of Advanced Mechanical Design, Systems, and Manufacturing, Vol. 6, No. 6, (2012), pp.916–922.

CHAPTER 4: HIGH-SPEED TURNING OF TITANIUM ALLOY WITH DIAMOND TOOLS

4.0 Introduction

Titanium alloy (Ti-6Al-4V) has been used in in aerospace, automotive, chemical plant, power generation, medical applications and several other industries owing to properties such as high strength, low weight (weight-to-strength ratio) and excellent corrosion resistance. In order to exploit this exceptional material as machine components, it is essential to machine with desired sharpness, accuracy, integrity and productivity. Serious tool wear, however, occurs when titanium alloy is machined because the low thermal conductivity of the material causes high cutting temperature [1-3]. A strong alloying tendency or chemical reactivity with materials also promotes galling, adhesion and diffusion/dissolution of tool materials [3-5].

There are many investigations on the machining of titanium alloys with several kinds of tool materials [6]. Narutaki et al. [3] reported the high cutting temperature of carbide tools and the excellent cutting performance of natural diamond tools in their pioneering study. Jawaid et al. [7] used the straight tungsten carbide inserts for turning Ti-6246 alloy. They reported that the tool life decreases rapidly when the cutting speed exceeds 60 m/min, and the dominant wear mechanisms of dissolution-diffusion and attrition were found. Zhang et al. [8] also applied the tungsten carbide tools in high-speed milling of Ti-6Al-4V alloy at the cutting

speed of 150 m/min. They observed that tungsten, cobalt and carbon diffused onto the workpiece during diffusion experiments in which the carbide tool and the Ti-6al-4V specimen were placed side by side and heated at 773 K in the furnace. Hartung et al. [9] measured the tool–chip interface temperature using a tool–chip thermocoupling technique in turning of Ti-6Al-4V with TiB2- and HfC-coated and uncoated cemented carbide tools. The cutting temperature approached the melting point of titanium when the cutting speed exceeded 460 m/min, and this high temperature caused the crater wear.

The advanced tool materials such as PCD and CBN were also applied to high-speed cutting of titanium alloys. Ezugwu et al. [10] reported lower cutting performance of CBN tools compared to uncoated carbide tools. Nabhani et al. [11] executed the simple quasi-static contact method in order to identify the critical workpiece–tool interface temperature in the formation of strong adhesion of titanium alloy. 760ºC and 900ºC were obtained for PCD and CBN, respectively. König et al. [12] found that the diffusion and dissolution processes of PCD tools were promoted by high local temperature due to poor thermal conductivity of the workpiece in turning Ti-6Al-4V. Similar results were obtained by Nabhani [11] for PCD and polycrystalline CBN (PCBN) when machining titanium alloys. Recently, binderless CBN sintered tools (BCBN) without any matrix materials have become available. Hirosaki et al. [13] reported better cutting performance of binderless PCBN compared to conventional PCBN and polycrystalline diamond tools in the machining of a vanadium-free titanium alloy. Wang et al. [14] also used BCBN for high-speed milling of Ti-6Al-4V at the cutting speed of 300-400 m/min. Non-uniform wear at the flank face was found to dominate, and adhesion of the

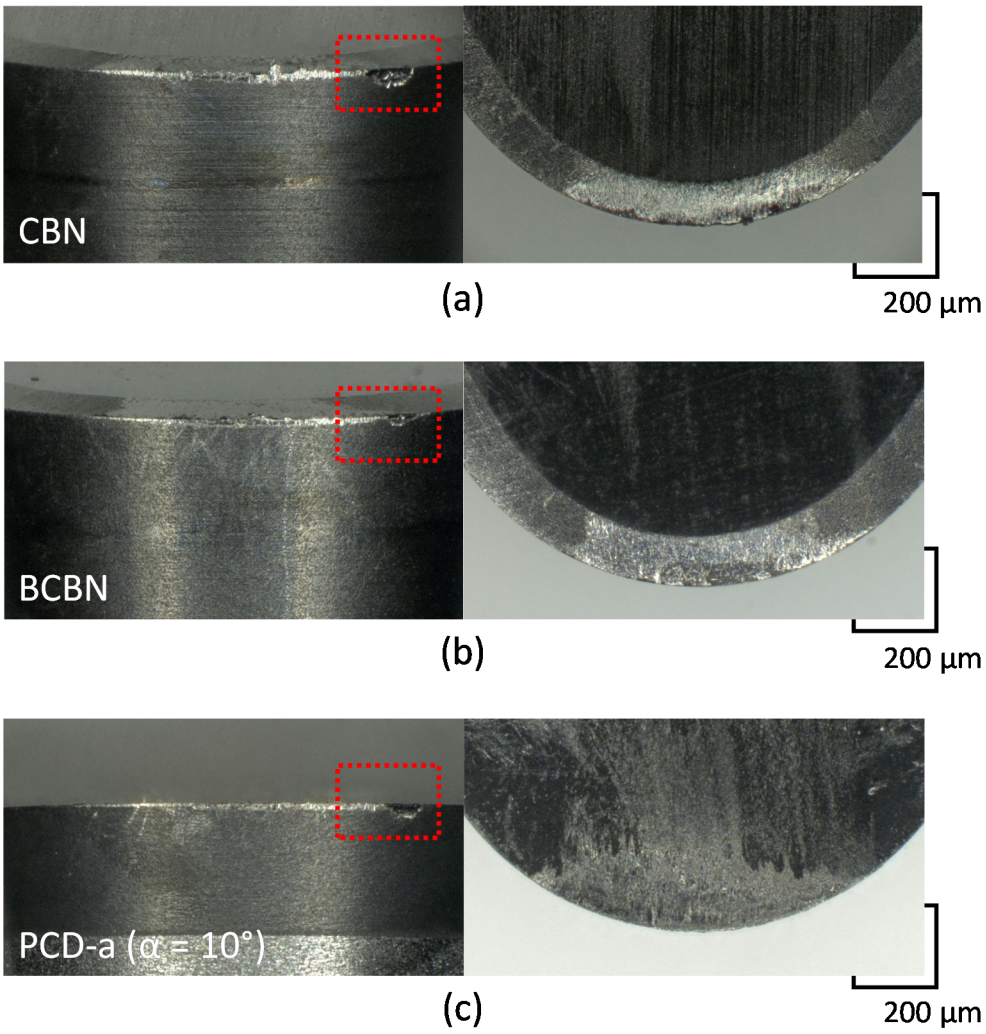

Fig. 4.1 Premature excessive adhesion/wear (highlighted by red box) on (a) CBN (b) BCBN and (c) PCD-a cutting Ti-6Al-4V in wet conditions at 300 m/min at 25 m of cutting length

workpiece materials on the flank face of the tool was also observed at higher depth of cut, feed rate and cutting speed. It was concluded that BCBN could be the most functionally satisfactory cutting-tool material for machining titanium alloys. Nevertheless, monocrystalline and polycrystalline diamond tools were found to have valuable characteristics such as high hardness and wear resistance and outstanding thermal conductivity, which are beneficial properties in machining titanium alloys [15].

Diamond is considered one of the hardest materials; whether it is created naturally or synthetically. Tools made of materials such as SC diamond and NPD have been used to cut ultra-hard materials owing to their hardness and thermal conductivity properties. These diamond tools have been seen as a chemically stable in its current usage. In the preliminary experiments, five types of super-abrasive tools – PCBN, BCBN, PCD, SC diamond, and NPD – were used in the turning of Ti-6Al-4V in both dry and wet conditions. Significant tool wear and/or adhesion of work material on the tool face were observed, preventing continuation of the cutting experiments with PCBN, BCBN and PCD. The tools are shown in **Fig. 4.1**.

In this study, the cutting performances of the SC diamond and NPD tools are investigated and their wear mechanisms examined.

4.1 Experimental Procedure

4.1.1 Workpiece Material and Cutting Tools

The most widely used α/β titanium alloy – Ti-6Al-4V (Grade 5) – is selected as the workpiece. Its applications are blades, discs, rings, airframes, biomedical implants, and others. **Table 4.1** shows the properties of the Ti-6Al-4V alloy used.

Table 4.1 Characteristics of workpiece materials

Workpiece	Specific Heat ρ [J/(kg·K)]	Thermal Conductivity λ [(W/(m·K)]	Hardness *HV* [GPa]
Ti-6Al-4V	520	7.1	3.8

Table 4.2 Physical properties of tool materials

Tool specification	Thermal Conductivity λ [W/(m·K)]	Hardness *HV* [GPa]
SC	1000 – 2200	70 – 120
BL-NPD	250 – 300	120 – 140

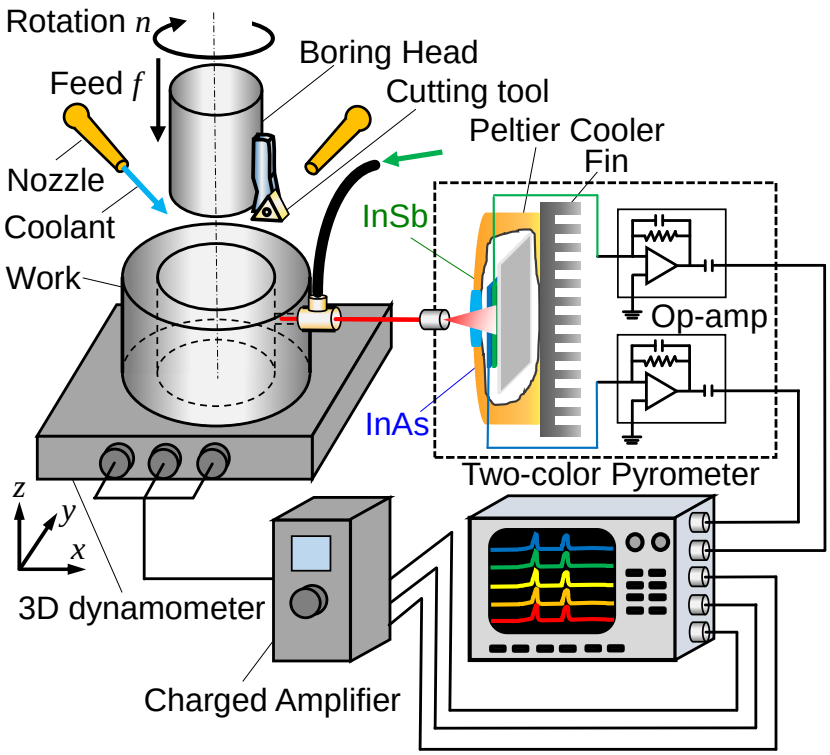

Fig. 4.2 Experimental set-up of internal turning

As stated, two types of diamond tool – SC diamond and a binderless nano-polycrystalline diamond (BL-NPD) – are used here. **Table 4.2** shows the characteristics of the tool materials. BL-NPD has extremely fine grain size ranging from 30 to 50 nm.

Table 4.3 Experimental conditions

Cutting tool (Binderless diamond)		Single crystal: SC Nano-polycrystalline: BL-NPD
Rake angle	α	0°
Nose radium	r_ε	0.8 mm
Workpiece		Ti-6Al-4V
Cutting speed	v	300 m/min
Depth of cut	a	0.2 mm
Feed rate	f	0.1 mm/rev
Cutting style		Wet (q_c=6 ℓ/min)
Coolant		Emulsion (1:30 in water)

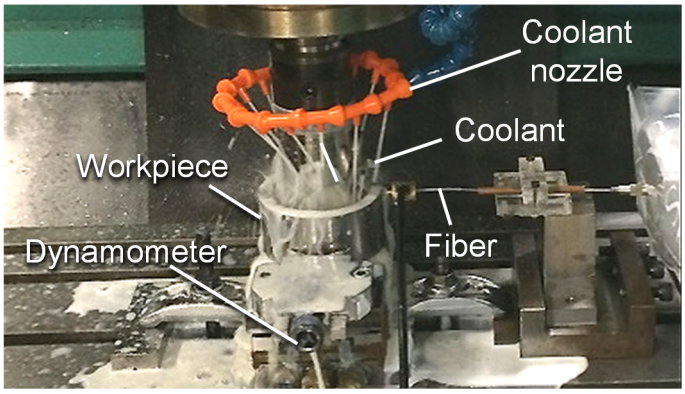

Fig. 4.3 Wet cutting with circular coolant nozzle array

4.1.2 Experimental Set-up and Conditions

The internal turning experiments with cutting fluid are carried out using the vertical machining center (Matsuura MC-600 V), as shown in **Fig. 4.2**. As shown in the figure, the cutting tool is mounted on a boring head. The workpiece is prepared in a tubular shape with the dimensions ϕ76.5×ϕ100×h50 mm. In order to assess the availability of cutting tools, the relatively high cutting speed of v=300 m/min is set. The other operating parameters are summarized in **Table 4.3**. The cutting tests are done with several different numbers of cutting

pass, where each cutting pass is equivalent to 25 m of cutting length. A water emulsion coolant is supplied at 6 ℓ/min with the nozzle arrays circularly located above the tubular workpiece, as shown in **Fig. 4.3**.

The cutting performance of each tool is evaluated by cutting force, cutting temperature, surface roughness and tool wear. Cutting force, cutting temperature, tool wear and surface roughness are measured by a three-axis piezoelectric dynamometer, two-color pyrometer, stylus profilometer and SEM, respectively.

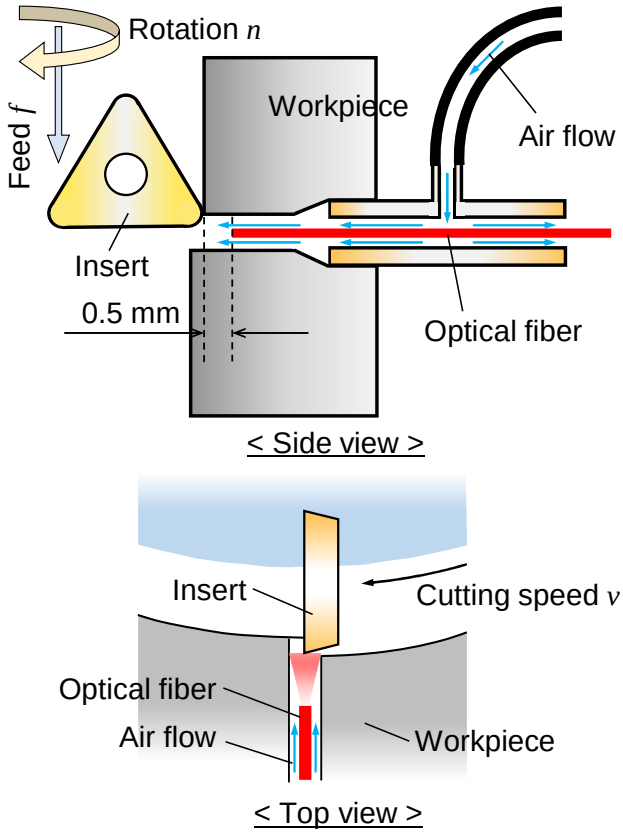

Fig. 4.4 Cutting temperature measurement in wet cutting

4.2 Cutting Temperature Measurement

As stated above, the cutting temperature is measured using a compact two-color pyrometer. As illustrated in **Fig. 4.1**, the chalcogenide glass fiber is inserted into a small hole (ϕ1.1 mm) drilled through the inner surface of the cylindrical workpiece. The infrared rays radiated from the flank face of the tool are accepted by the fiber tip's incidence face when the cutting tool passes over the hole during the cutting operation. In order to avoid coolant flowing into the probe hole, compressed air is supplied from the fiber tube, as shown in **Fig. 4.4**. The thermal radiation accepted by the fiber tip is transmitted to the two-color detector, which comprises InAs photovoltaic and InSb photoconductive cells assembled in a sandwich arrangement. These detectors are electrically cooled by a Peltier device and have different spectral sensitivities within the ranges 1–3 µm and 3-5.5 µm, respectively. The infrared radiation received by the detectors is then converted into electrical energy and amplified. By taking the output voltage ratio from these detectors, the temperature of the object can be calculated using the calibration curve obtained in the experiment. The pyrometer, having a flat response from 10 Hz to 400 kHz, can be used for measurement of the tool temperature in turning with acceptable accuracy [16]. This type of pyrometer has also been successfully employed in other applications such as milling [17] and drilling [18].

4.3 Cutting Force Measurement

In this experiment, the tubular workpiece is mounted on the three-axis (*x*-*y*-*z*) piezoelectric dynamometer, so that the sinusoidal cutting forces F_x and F_y and the constant axial force F_z are measured in internal turning. Then, the principal (tangential) cutting force F_p and the thrust (normal) force F_{th} are calculated based on F_x and F_y with respect to tool rotational position θ, as shown in **Fig. 4.5**. Here, F_z is equivalent to feed force F_f.

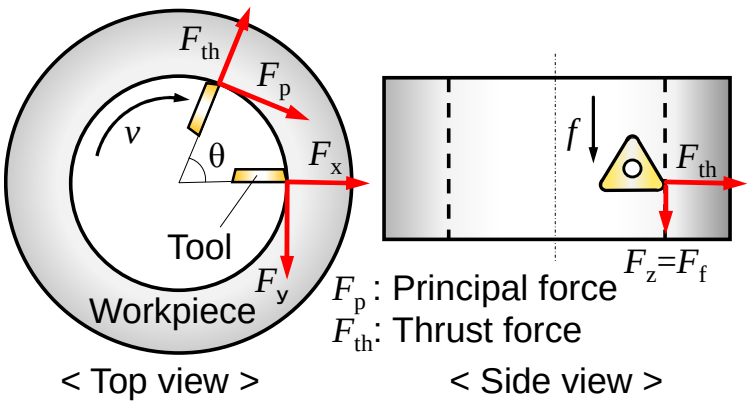

Fig. 4.5 Definition of cutting forces

4.4 Experimental Results

4.4.1 Cutting Force

The cutting force changes with cutting length L_c for the two types of diamond tool are presented in **Figs. 4.6** and **4.7**. It can be clearly seen from the figures that cutting force increases with the number of cutting pass, due to the dulling of the cutting edge. It seems to increase relatively rapidly when the cutting length exceeds approximately 600 m.

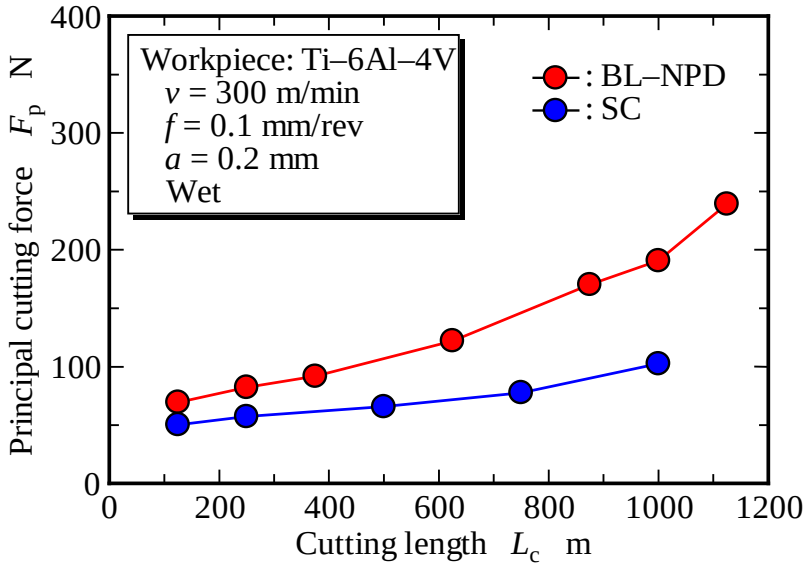

Fig. 4.6 Change of principal cutting force with cutting length

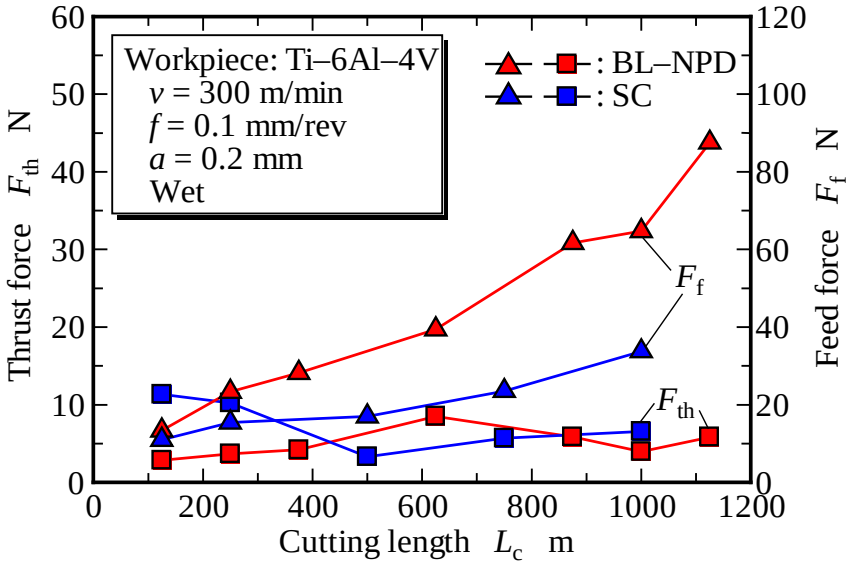

Fig. 4.7 Change of thrust and feed force with cutting length

As for the comparison between the SC and BL-NPD tools, the cutting force of the BL-NPD tool, especially F_p and F_f, increases faster than that of SC; higher cutting force is then observed in the NPD tool. There is not much difference between the tools at the initial stage of cutting due to their similar geometry; the higher cutting force of BL-NPD is related to the higher wear rate – even though BL-NPD is much harder than SC, as shown in Table 2. This could be related to the promotion of attritional wear or the growth of adhesion of work material on flank/rake faces. The cutting-edge dullness increases the friction between tool and chip/workpiece, and thus the thrust force F_{th} does not change so much with cutting length. It should be noted that the chipping of the SC tool occurs after the cutting length of 1000 m, whereas chipping does not takes place on the BL-NPD tool at all. This shows the high toughness of the BL-NPD tool.

4.4.2 Cutting Temperature

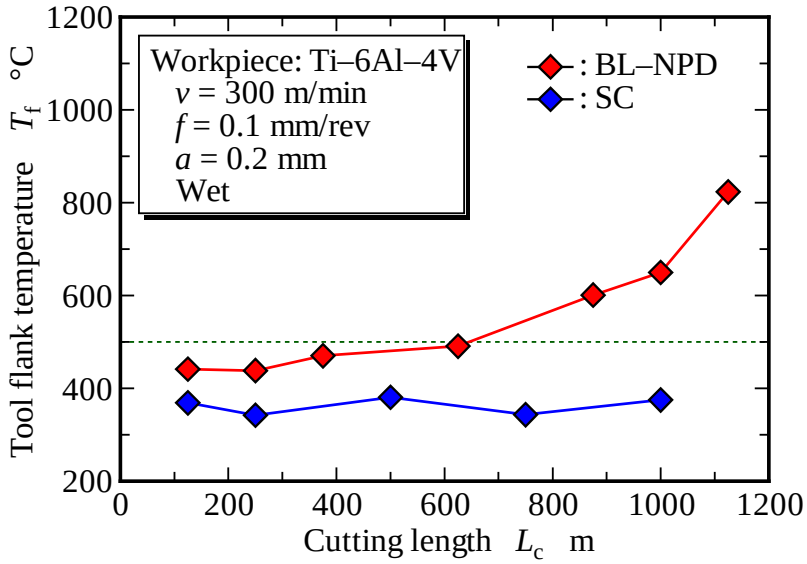

Fig. 4.8 Change of tool flank temperature with cutting length

Fig. 4.8 shows the change of tool flank temperature T_f with cutting length L_c for the two types of diamond tool. In BL-NPD, it is evident that the temperature increases as the cutting length increases, and it reaches approximately 800ºC or higher when the cutting length reaches 1125 m. This temperature curve has a similar tendency to that of principal cutting force F_p, as shown in **Fig. 4.6**, where both cutting temperature T_f and cutting force F_p of the BL-NPD tool increase relatively rapidly at L_c=600 m.

Meanwhile, the tool flank temperature of the SC diamond tool shows minute increments around 350ºC throughout the cutting experiments; naturally, the cutting force does not increase as much, as shown in **Fig. 4.6**. The higher temperature of BL-NPD seems to be primarily caused by the low thermal conductivity (250–300 W/(m·k)) relative to that of SC diamond (1000–2200 W/(m·k)), as shown in Table 2. It should be noted that the large amount of adhesion (discussed below) could influence cutting temperature [19] due to the experimental conditions and the relatively high thermal conductivity of the tools used. The temperature recorded is taken as the tool edge cutting temperature. High temperature on the BL-NPD tool is expected due to tool geometrical changes [20].

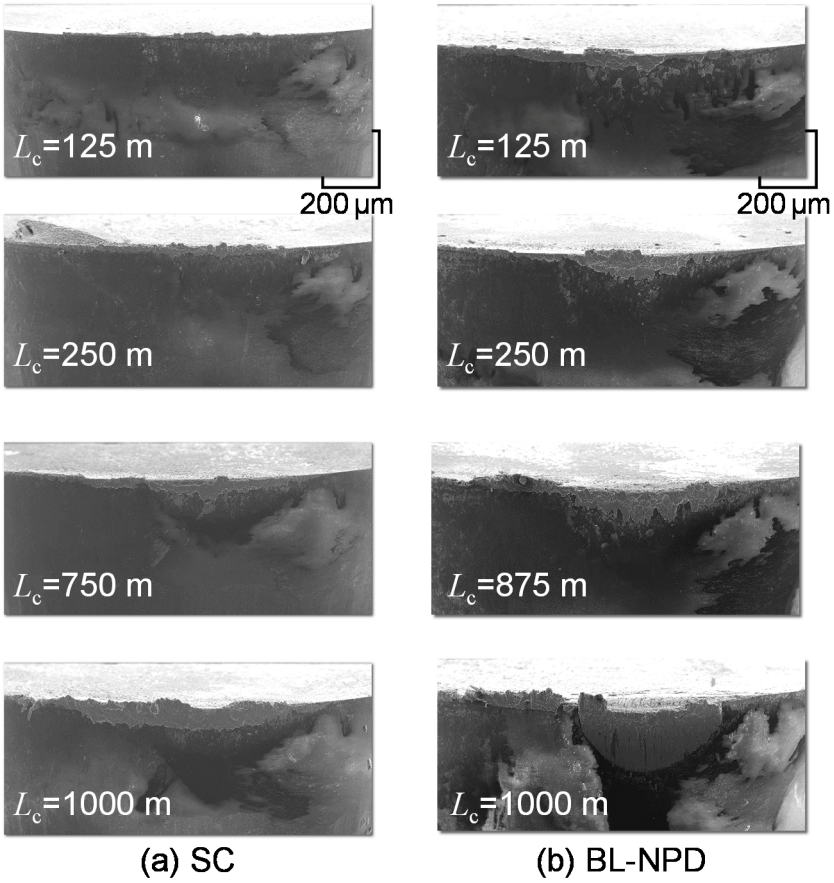

Fig. 4.9 SEM photographs of the worn cutting edges of SC and BL-NPD tools (the white region indicates electron scattering due to accelerating voltage)

4.4.3 Tool Wear

4.4.3.1 Tool morphology

Fig. 4.9 presents the SEM photograph of the cutting edge of the SC diamond and BL-NPD tools. As seen in the figure, the growth of the adhesion of work material already starts at L_c=125 m, and it becomes pronounced from L_c=500 to 700 m in the case of BL-NPD. The SEM photographs clearly show the rate of adhesion is much higher in the BL-NPD tools.

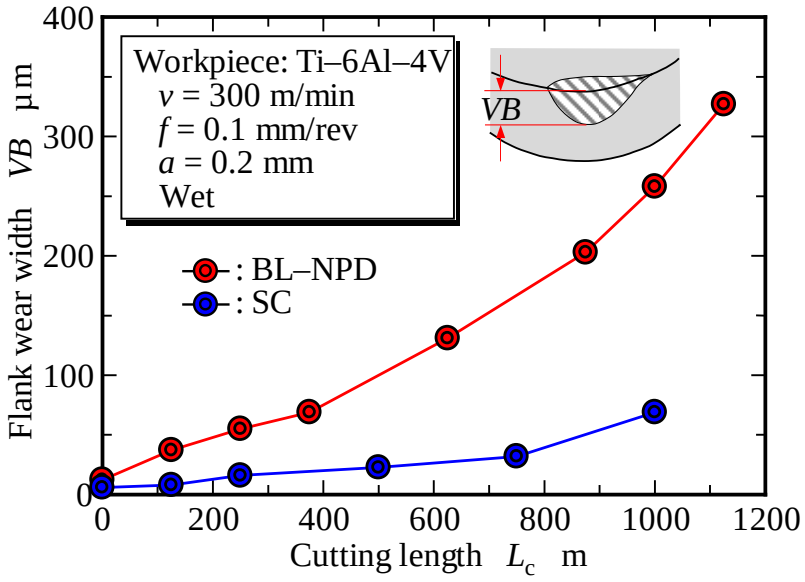

Fig. 4.10 Change of flank wear width with cutting length

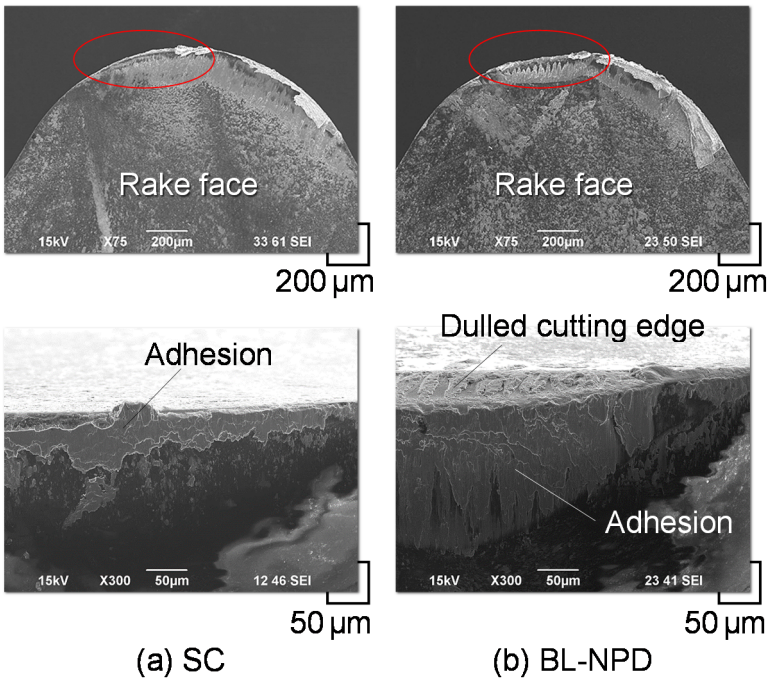

Fig. 4.11 SEM photographs of rake face and cutting-edge morphologies of SC diamond and BL-NPD tools at L_c=1000 m

The growth of flank wear width *VB* with cutting is shown in **Fig. 4.10**. As shown in the figure, the *VB* curve has a similar form to the curves of cutting force and tool flank temperature. According to the tool morphologies shown in Fig. 8, the tool wear mechanisms seem to be

related to the adhesion of Ti-6Al-4V because the flank wear is mostly under the adhesion layer in every photograph taken.

4.4.3.2 Wear mechanism

Fig. 4.11 shows the SEM photographs of the rake faces for the BL-NPD and SC tools after the cutting length of 1000 m. In these figures, the red circles show the tool-work contact region. There is visible geometrical change in the BL-NPD tool, which is less marked in the SC diamond tool. It is unmistakable that the tool wear of both tools is linked to adhesion. As shown in the close-up images in **Fig. 4.10**, the adhesion covers almost all of the flank wear region on the cutting edge. At the same time, the wear region is clearly seen in both tools. Small crater wear such as chamfering is observed on the BL-NPD tool; on the SC diamond tool, adhesion and wear are relatively insignificant. However, large-scale chipping has taken place after the cutting length of approximately 1000 m due to brittleness. Chipping tends to occur at engagement or disengagement.

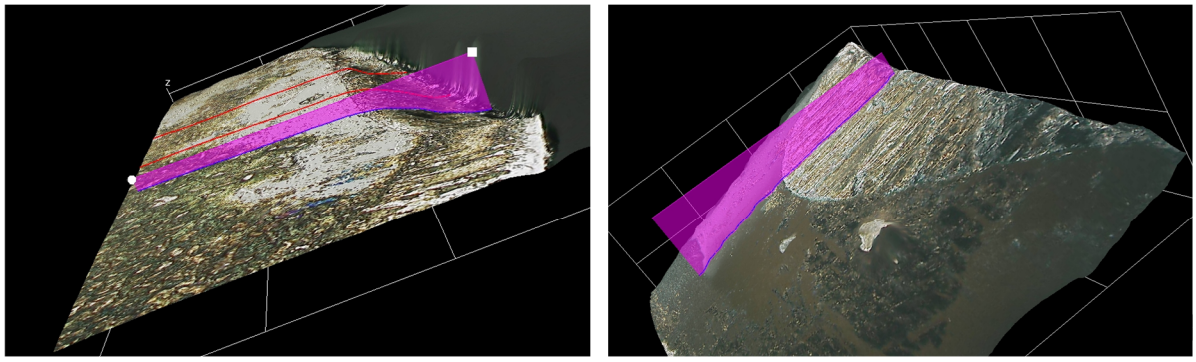

Fig. 4.12 (a) Rake and (b) flank of worn BL-NPD tools (1125 m cutting length) observed under 3D microscope

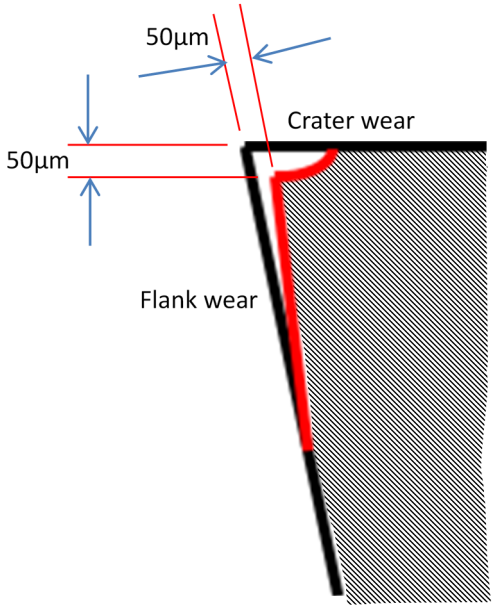

Fig. 4.13 Geometrical change of cutting edge of worn BL-NPD at 1125 m cutting length based on **Fig. 4.12**

Furthermore, as shown in **Figs. 4.12** and **4.13**, the tool edge at the end of life of BL-NPD experienced geometrical changes, affecting the flank and rake faces of the tool. As measured here, the dimension changes with BL-NPD are around 50 µm in depth. Note that this measurement includes the adhesion on the tool edge, and the dimension changes are expected to be higher after etching.

4.4.4 Surface Roughness

Fig. 4.14 shows the change of surface roughness R_z with cutting length. In the case of the SC diamond tool, it is evident that the surface roughness decreases as the cutting progresses. This is due to the geometrical changes of the tool that occur through wear of the cutting edge, whereby the rake angle changes to a negative value and the nose radius also increases. It is well known that the negative rake angle produces a smoother surface profile than a 0º configuration

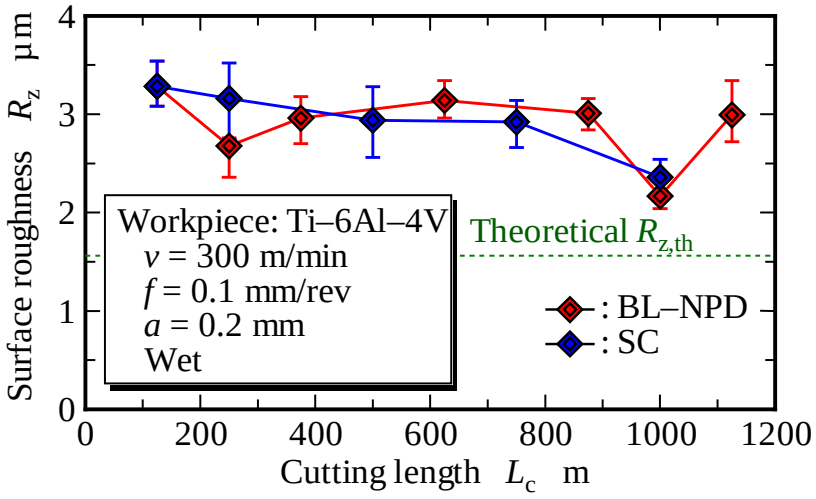

Fig. 4.14 Change of surface roughness with cutting length

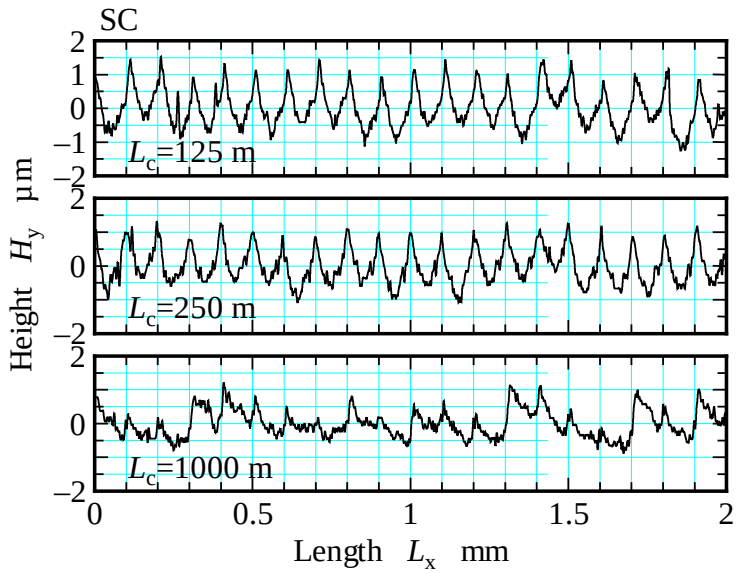

Fig. 4.15 Change of surface profile with cutting length for SC diamond tool

or a positively angled tool. On the other hand, surface roughness remains almost constant at around 3 µm due to the adhesion of work material on the tool face.

The longitudinal surface profiles of the workpieces cut by SC diamond and BL-NPD tools are shown in **Figs. 4.15** and **4.16**, respectively. Relatively clear feed marks are observed until L_c = 750 m in the case of the SC diamond tool. On the other hand, similar machined

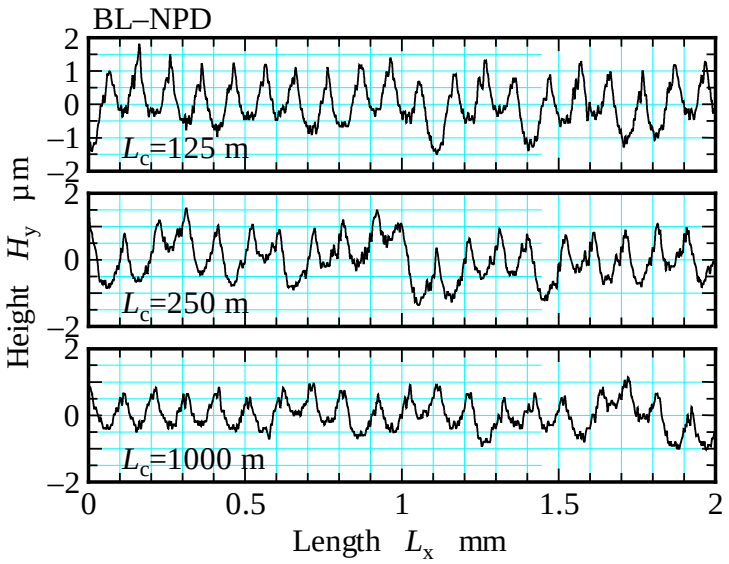

Fig. 4.16 Change of surface profile with cutting length for BL-NPD tool

profiles are formed in cutting with BL-NPD tool due to the successive adhesion and abrasion actions of the Ti-6Al-4V material.

4.5 Discussion of Tool-Workpiece Interaction

4.5.1 EDS Analysis

Fig. 4.17 presents the microscopic images of the worn rake and flank faces of the BL-NPD tool. The tool is etched by 1% HF-HNO_3 in order to remove the bonded Ti-6Al-4V, while adhered materials partially remain. As shown in the figure, a very smooth surface without scratch marks is observed, which suggests that diffusion wear is dominant rather than attritional wear.

Based on research done by Nabhani et al. [11], it can be stated that the smoothness of the flank face and crater is due to diffusion–dissolution wear of the tools. Diffusion–dissolution

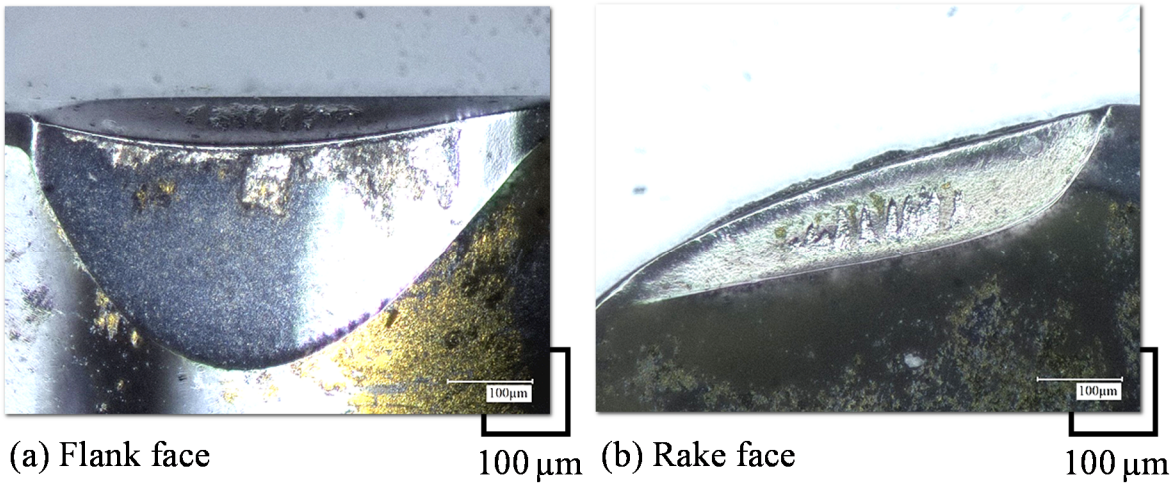

Fig. 4.17 Microscopic image of BL-NPD tool after etching by 1% HF-HNO_3

Table 4.4 Enthalpies of formation of carbides

Metal	Carbide	ΔH kJ/mol
Titanium (Ti)	TiC	92
Niobium (Nb)	NbC	71
Vanadium (V)	VC	51
Molybdenum (Mo)	MoC	5

wear occurs with some combinations of carbon-based tools and titanium work materials, and is promoted at high cutting temperature above 500ºC. Based on Pettifor's semi-empirical work, Kuljanic et al. [21, 22] reported a relation indicator of some well-known metals with carbon, as shown in **Table 4.4**. From this table, it can be concluded that titanium has a very high affinity to form carbide in comparison to niobium, vanadium and molybdenum.

The SEM/EDS (energy-dispersive X-ray spectroscopy) mapping analysis is carried out for both the SC diamond and the BL-NPD tool. The element mapping images of C, Al, Ti and V corresponding to each tool are shown in **Figs. 4.18** and **4.19**, respectively. In the BL-NPD

element mapping, less carbon (diamond) is detected on the relatively large flank wear region whereas Ti, Al and V are fully detected in the whole wear region. This means that the workpiece Ti-6Al-4V is firmly adhered to the flank wear region, and the wear is deeply related

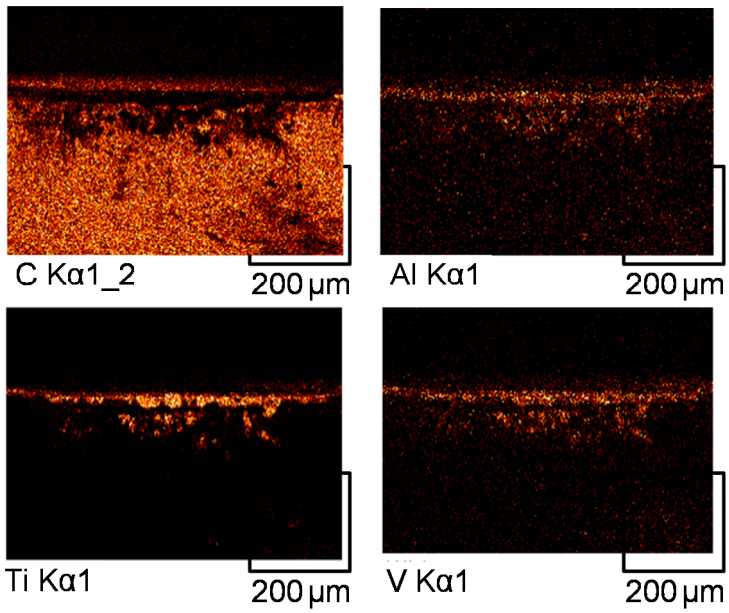

Fig. 4.18 SEM/EDS element mapping for flank face of SC diamond tool

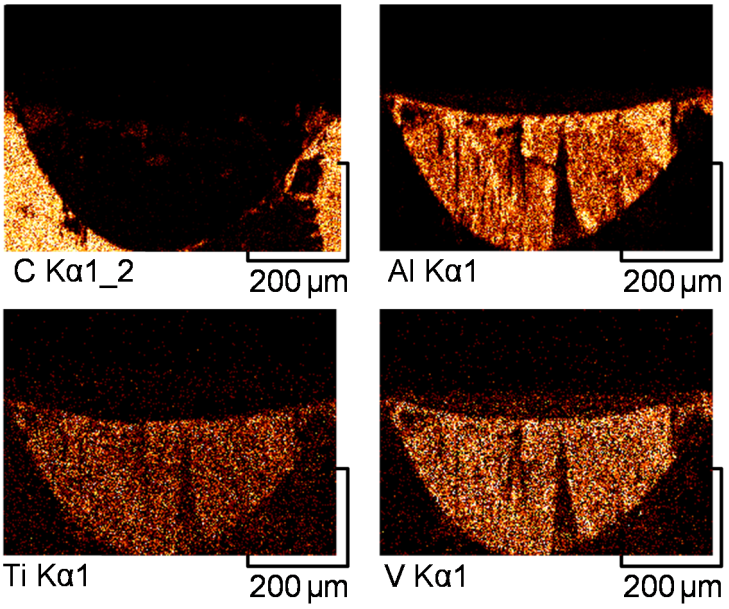

Fig. 4.19 SEM/EDS element mapping for flank face of BL-NPD tool

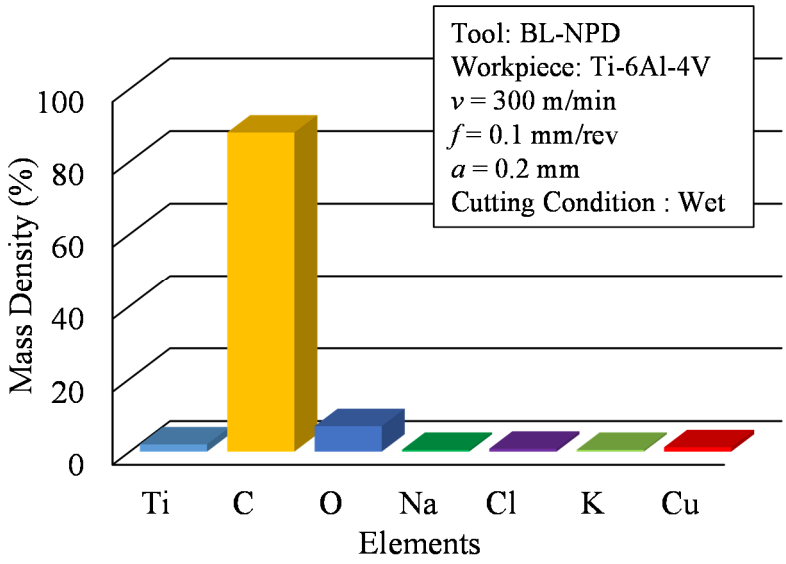

Fig. 4.20 Elemental analysis on etched BL-NPD flank face

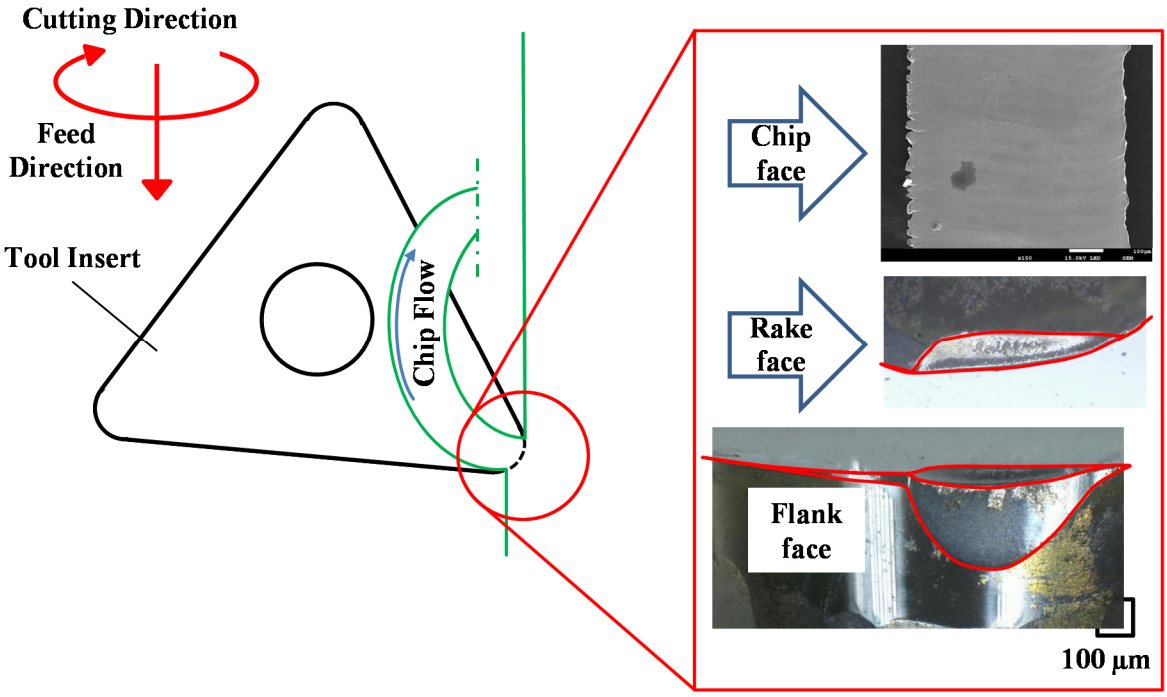

Fig. 4.21 Carbon-based build-up position on the cutting chips

to the adhesion of the workpiece. The same tendency is obtained for the SC tool, as shown in Fig. 15; however, the adhesion area is smaller than that of the BL-NPD tool with weak indication of Al, Ti and V. It is estimated that the worn area of the flank and rake face behind

the adhesion is diffusion/dissolution, where chemical reactions between the tool (carbon) and workpiece (titanium) take place under high temperature.

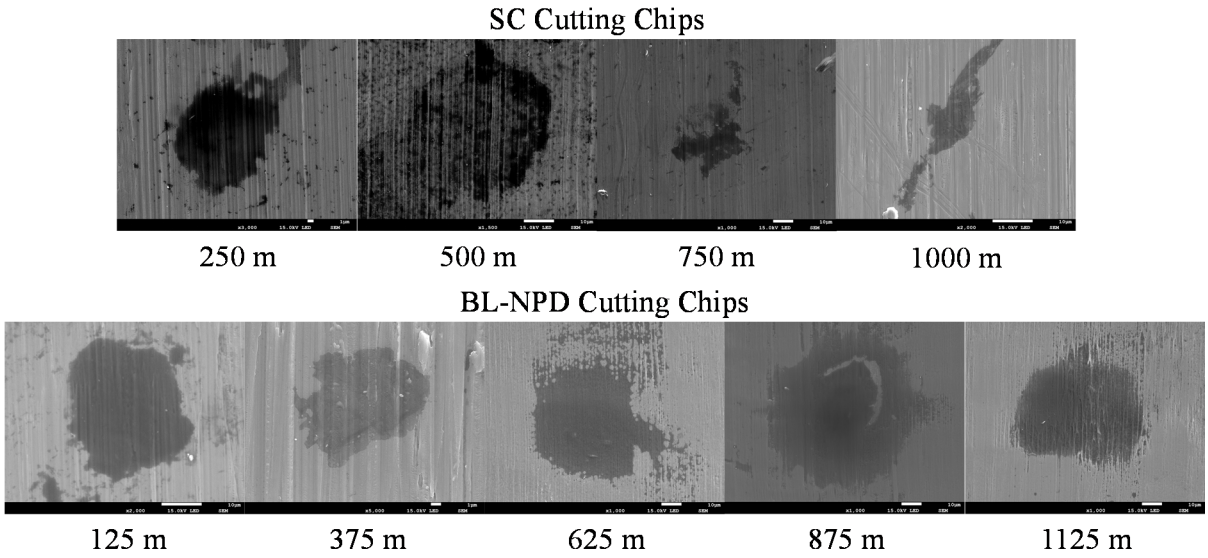

Fig. 4.22 Suspected carbon build-ups on cutting chips

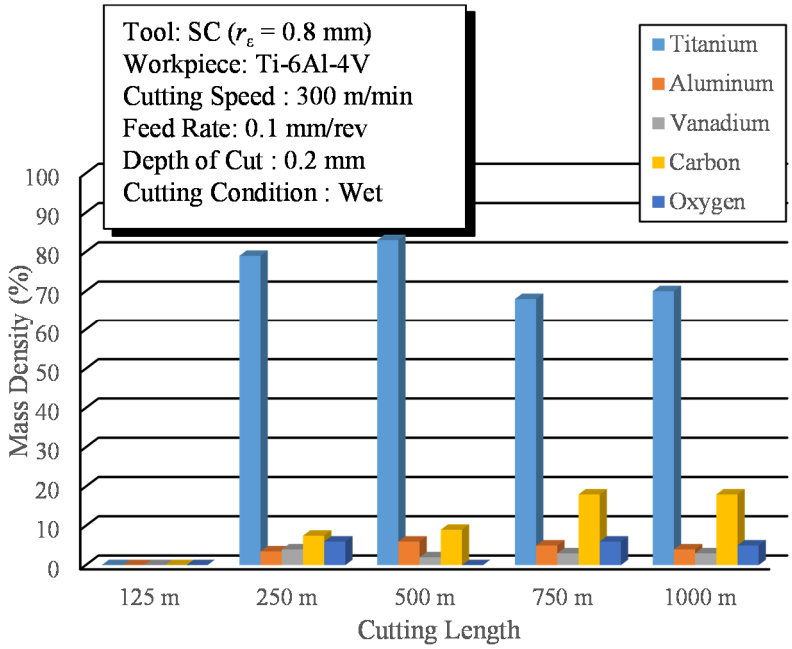

Fig. 4.23 EDS elemental analysis of back surface of cutting chips for SC tool

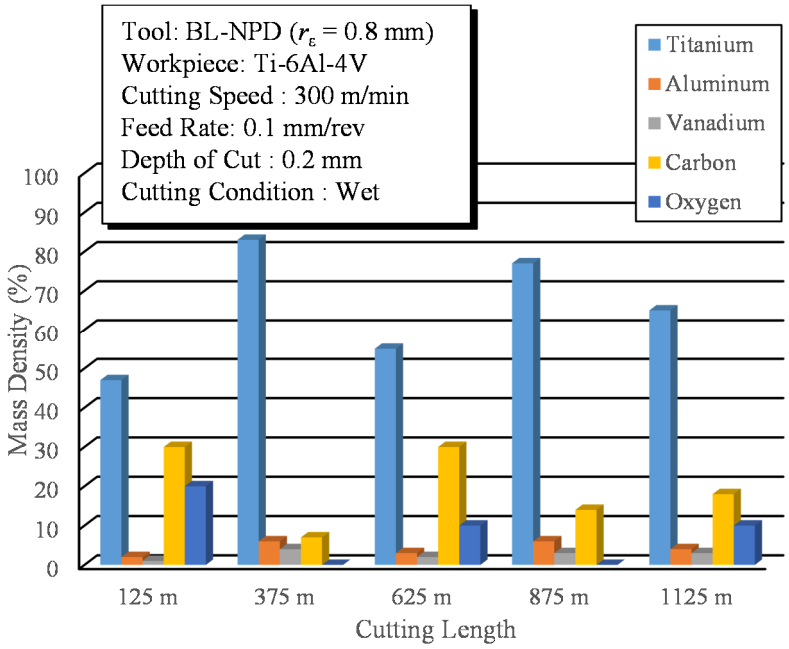

Fig. 4.24 EDS elemental analysis of back surface of cutting chips for BL-NPD tool

In order to confirm the existence of TiC between the Ti-6Al-4V and the diamond tools, SEM/EDS mapping is also done on the etched surface, as shown in **Fig. 4.17**. **Fig. 4.20** illustrates the elemental analysis of the flank face of the BL-NPD tool. Here, the suspected build-up contains C, O and Ti with traces of Na, Cl, K and Cu. The last four elements might come from the coolant used. It is supposed that TiC and TiO_2 are formed, but the presence of these compounds cannot be corroborated. The tool material could also diffuse into the cutting chip during high-speed cutting.

To gain more evidence for the chemical reaction between tool and chip, an SEM/EDS analysis is done for the cutting chips for both tools. The suspected carbon-based build-up is seen on the chip surface touching the rake face, as shown in **Fig. 4.21**. It is hypothesized that the titanium carbide is diffused into the cutting chip during the cutting. In the SEM images, these suspected build-ups are represented by the dark color. **Fig. 4.22** shows the gathered image

of the supposed carbon build-ups, which are assumed to be very thin. EDS analysis shows evidence of C in the dark area, as shown in the readings in **Figs. 4.23** and **4.24** for the SC diamond and BL-NPD cutting chips. The Ti signal from the background is strong indicating that the build-up is thin. Note that the reading on the SC diamond tool cutting chips at 125 m cutting length is not available due to the scarcity of the build-up during SEM observation. **Fig. 4.25** shows typical close-up images of the back surface of the chip strips and their element mapping with respect to carbon and titanium. As shown in the SEM photographs, dark spots are observed on the chip surface, and these increase in number as cutting proceeds, especially with the BL-NPD tool. The EDS mapping analysis reveals a substantial amount of carbon (carbide) on the Ti-6Al-4V chips, as shown in **Fig. 4.25,** proving that these carbon element build-ups do not emerge from the cutting fluid. This tendency is prominent in cutting with the

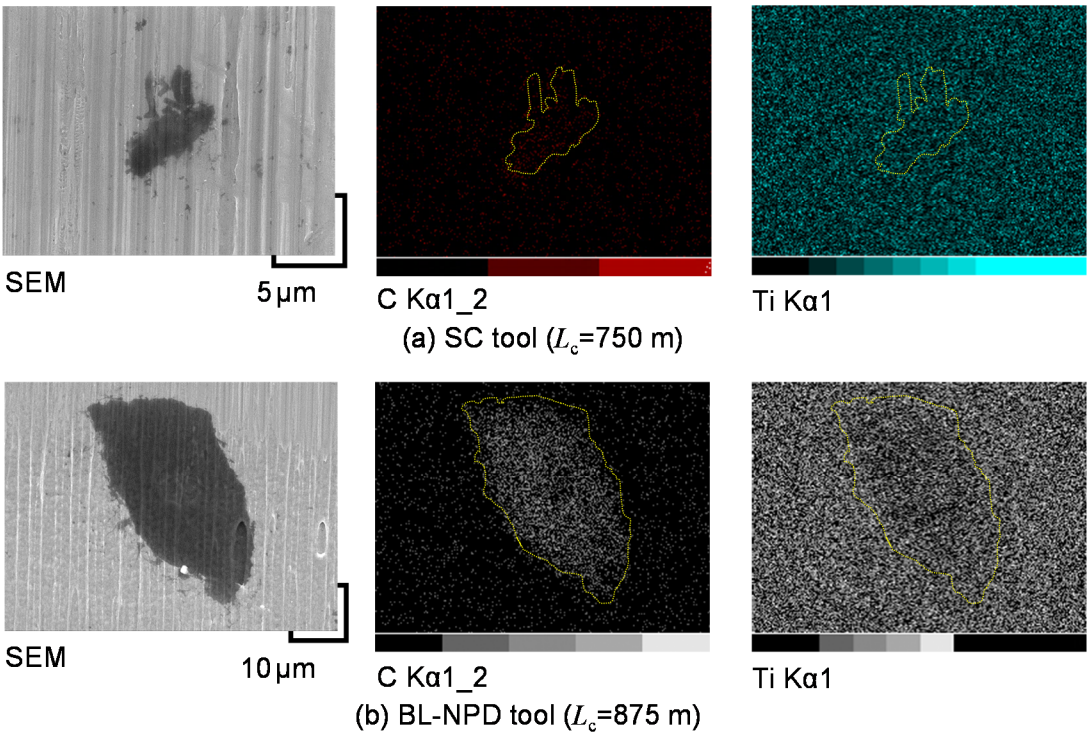

Fig. 4.25 SEM/EDS photographs and element mapping of back surface of cutting chips

BL-NPD tool. It is hypothesized that the TiC on these cutting chips comes from chemical reactions at high temperature. Nabhani [11] and Klocke et al. [15] reported that TiC seems to inhibit the growth of tool wear in the cutting of titanium alloy with PCD tools due to its wear resistance properties; however, this is not the case in this experiment, where the EDS analysis appears to show that the TiC formation is carried away by the passing chip. In the case of BL-NPD, tool wear acceleration by diffusion shows that the assumed TiC layer does not impede tool wear growth.

4.5.2 Wear Model Analysis

Based on the results and discussion in the previous section, a diffusion–dissolution wear model is proposed for the cutting of Ti-6Al-4V with diamond tools. **Fig. 4.26** demonstrates the simplified diffusion–dissolution wear model under consideration. During cutting, the workpiece material adheres to the tool surface (a, b). As the cutting process continues, the chemically unstable environment catalyzes the formation of carbides (TiC) under the adhesion layer (c, d). Detailed close-ups of (c) and (d) in **Fig. 4.26** are shown in Fig. 4.24. It is hypothesized that C atoms from the macromolecules (diamond) chemically react with Ti atoms on the Ti-6Al-4V material, and vice versa, as shown in **Fig. 4.27** (a). Thus, a thin layer of TiC is formed at the boundary between tool and chip/workpiece. This is due to the high affinity of Ti to form TiC with C, as explained by Pettifor [22]. The thin layer of carbide, which fuses carbon atoms on the tool surface and the titanium substrate in the adhesion, will be diffused and dissolved by the chip movement (e, f, and g). The process is repeated (h) throughout the cutting. According to the above mechanism, relatively substantial tool wear occurs with BL-

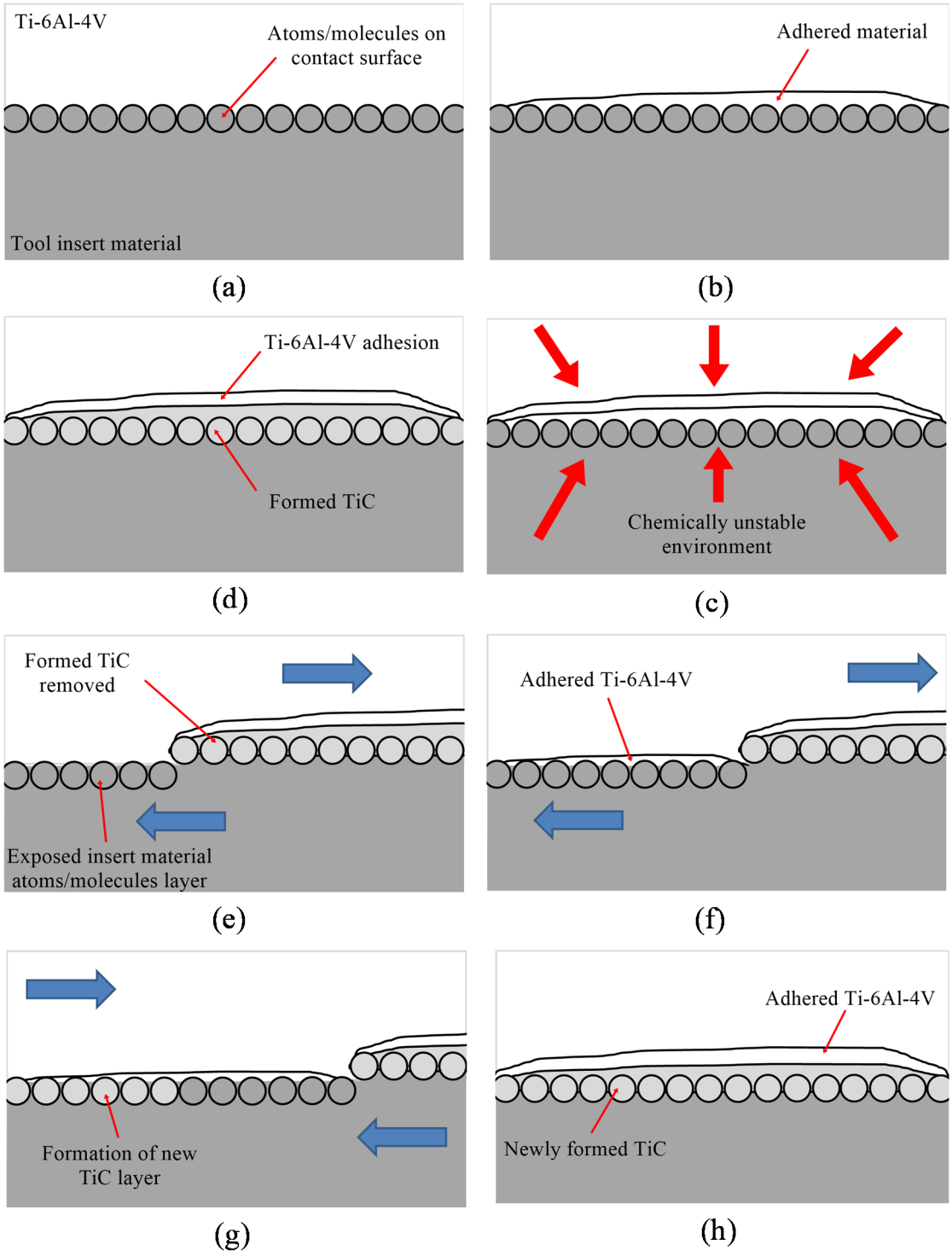

Fig. 4.26 Diffusion–dissolution wear model of diamond tools in cutting Ti-6Al-4V

NPD at high cutting temperature above 500ºC, as shown in **Fig. 4.8**. Both tools are binderless and the work–tool combination is the same, but the cutting temperature of BL-NPD is higher. This proves that the thermal conductivity of a tool's material has a great influence on tool wear [12].

In the experiment, the BL-NPD tool wears more rapidly than the SC diamond tool. This is due to the fact that diffusion happens more rapidly along the grain boundary in comparison to the perfect lattice (single crystal), owing to the imperfect surface of the polycrystalline grain structure [23]. This has been shown in an example self-diffusing experiment on radioactive silver in monocrystalline and polycrystalline specimens. The results showed the influence of temperature in increasing the diffusion rate for both crystal structures, with the diffusion activity seen to be higher in the polycrystalline structure. Activities at elevated temperature

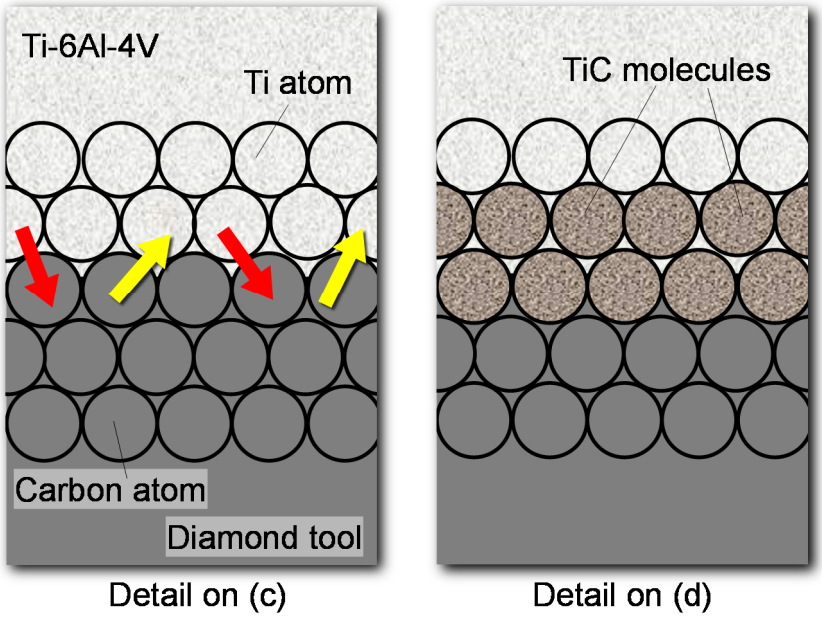

Fig. 4.27 Further magnification of the tool wear mechanism from **Figs. 4.26 (c) and (d)** showing the diffusion of Ti and C

were traced on the grain boundaries of the polycrystalline silver [24]. Activation energy of diffusion is therefore less in the polycrystalline than in the lattice or single-crystal structure [23, 25]. This means that any temperature-dependent diffusion will occur earlier at lower temperature in polycrystalline structures than in monocrystalline structure, as witnessed in the accelerated wear on the BL-NPD tool during cutting of Ti-6Al-4V.

4.6 Conclusions

Two types of binderless diamond tool – SC diamond and BL-NPD – were applied to high-speed turning of titanium alloy (Ti-6Al-4V) with water-soluble coolant. The main results obtained are as follows.

(1) The cutting force of BL-NPD increases with cutting length faster than that of SC diamond. The higher cutting force of BL-NPD is caused by the higher wear rate, even though BL-NPD is much harder than SC diamond.

(2) The flank temperature of the BL-NPD tool is considerably higher than that of the SC tool, reaching approximately 800ºC at the cutting length L_c=1125 m. This temperature difference is caused by the thermal conductivities of the tool materials.

(3) The *VB* curve with respect to cutting length has a similar form to those of cutting force and tool flank temperature. The tool wear mechanisms seem to be related to adhesion of Ti-6Al-4V on the tool.

(4) Diffusion–dissolution wear occurs in such a manner that a thin TiC layer is formed between the diamond tool and adhered Ti-6Al-4V material, which dissolves through the cutting chip. This wear model seems convincing, since carbon element is detected by EDS analysis.

(5) The SD diamond tool shows better cutting performance in turning of Ti-6Al-4V at the cutting speed of 300 m/min. The BL-NPD diamond is tough but causes a high cutting temperature due to its low thermal conductivity and high rate of tool wear.

References:

[1]. Ezugwu E. O., and Wang Z. M., "Titanium alloys and their machinability – a review", J. Material Processing Technology, Vol. 68, pp. 262-274, 1997.

[2]. Zoya Z. A., and Krishnamurthy R., "The performance of CBN tools in the machining of titanium alloys", J. Materials Processing Technology, Vol. 100, pp. 80-86, 2000.

[3]. Narutaki N., and Murakoshi A., "Study on machining of titanium alloys", Annals of the CIRP, Vol. 32, Issue 1, pp. 65-69, 1983.

[4]. Pretorius C. J., Soo S. L., Aspinwall D. K., Harden P. M., M'Saoubi R., and Mantle A. L., "Tool wear behaviour and workpiece surface integrity when turning Ti-6Al-2Sn-4Zr-6Mo with polycrystalline diamond tooling", Annals of the CIRP, Vol. 64, Issue 1, pp. 109-112, 2015.

[5]. Da Silva R. B., Machado A. R., Ezugwu E. O., Bonny J., and Sales W. F., "Tool life and wear mechanisms in high speed machining of Ti-6Al-4V alloy with PCD tools under various coolant pressures", J. Materials Processing Technology, Vol. 213, pp. 1459-1464, 2013.

[6]. Rahman M., Eang Z.-G., and. Wong Y.-S, "A review on high-speed machining of titanium alloys", JSME Int. J. (C), Vol. 49, No. 1, pp. 11-20, 2006.

[7]. Jawaid A., Che-Haron C. H., and Abdullah A., "Tool wear characteristic in turning of titanium alloy Ti-6246", J. Material Processing Technology, Vol. 92-93, pp. 329-334, 1999.

[8]. Zhang S., Li J. F., Deng J. X., and Li Y. S., "Investigation on diffusion wear during high speed machining Ti-6Al-4V alloy with straight tungsten carbide tools", Int. J. Advanced Manufacturing Technology, Vol. 44, pp. 17-25, 2009.

[9]. Hartung P. D., and Kramer B. M., “Tool wear in titanium machining”, Annals of the CIRP, Vol. 31, Issue 1, pp. 75-80, 1982.

[10]. Ezugwu E. O., Da Silva R., Bonney B. J., and Machado A. R., “Evaluation of the performance of CBN tools when turning Ti-6Al-4V alloy with high pressure coolant supplies”, Int. J. Machine Tool & Manufacture, Vol. 45, pp. 1009-1014, 2005.

[11]. Nabhani F., “Wear mechanism of ultra-hard cutting tool materials”, J. Material Processing Technology, Vol. 115, pp. 402-412, 2001.

[12]. Konig W., and Neises A., “Turning TiAL6V4 with PCD”, Industrial Diamond Review, Vol. 2/93, pp. 85-88, 1993.

[13]. Hirosaki K., Shintani K., Kato H., Asakura F., and Matsuo K., “High speed machining of bio-titanium alloy with a binder-less PcBN tool”, JSME Int. J. (C), Vol. 47, No. 1, pp. 14-20, 2004.

[14]. Wang Z. G., Wong Y. S., and Rahman M., “High-speed milling of titanium alloys using binderless CBN tools”, Int. J. Machine Tools & Manufacture, Vol. 45, pp. 105-114, 2005.

[15]. Klocke F., Konig W., and Gerschwiller K., “AMST’96 CISM Courses and Lectures 372” (E. Kuljanic ed.), Springer Verlag, Vienna, pp. 7-21, 1996.

[16]. Nishimoto H., Tanaka R., Hosokawa A., Ueda T., and Furumoto T., “Development of tool edge temperature measurement method in wet cutting”, J. Advanced Mechanical Design, Systems, and Manufacturing, Vol. 6, No. 6, pp. 916-922, 2012.

[17]. Okada M., Hosokawa A., Tanaka R., and Ueda T., “Cutting performance of PVD-coated carbide and CBN tools in hardmilling”, Int. J. Machine Tools & Manufacture, Vol. 51, No. 2, pp. 127-132, 2011.

[18]. Okada M., Asakawa N., Sentoku E., M'Saoubi R., and Ueda T., "Cutting performance of an indexable insert drill for difficult-to-cut materials under supplied oil mist", Int. J. Advanced Manufacturing Technology, Vol. 72, No. 1-4, pp. 475-485, 2014.

[19]. Okada M., Hosokawa A., Asakawa N., and Ueda T., "End milling of stainless steel and titanium alloy in an oil mist environment", Int. J. Advanced Manufacturing Technology, Vol. 74, No. 9-12, pp. 1255-1266, 2014.

[20]. Tanaka R., Hosokawa A., Furumoto T., and Ueda T., "Effects of Tool Edge Geometry on Cutting Temperature in Continuous Cutting of Case Hardened Steel", Int. J. Automation Technology, Vol. 7, No. 3, pp. 313-320, 2013.

[21]. Kuljanic E., Fioretti M., Beltrame L., and Miani F., "Milling titanium compressor blades with PCD cutter", Annals of the CIRP, Vol. 47, Issue 1, pp. 61-64, 1998.

[22]. Pettifor D. G., "Bonding and Structure of Molecules and Solids", Oxford University Press, pp. 12-13, 1995.

[23]. Gleiter H. and Chalmers B., "High-Angle Grain Boundaries", Progress in Material Science, Vol. 16, pp. 77-112, 1972.

[24]. Turnbull D., "Grain Boundary and Surface Diffusion", Atom Movements, American Society of Metals Special Volume, pp. 129-152, 1951.

[25]. Shewmon P., Diffusion in Solids, Wiley, 2nd Ed., 1989.

CHAPTER 5: INVESTIGATION OF HARD TURNING OF CEMENTED CARBIDE

5.0 Introduction

Cemented carbides, which are commonly used for molds, dies and cutting tools, are currently machined or shaped by grinding and/or EDM (electrical discharge machining) in order to achieve the exact desired dimensions. In grinding of cemented carbides, an expensive diamond grinding wheel is needed, and the MRR (Material Removal Rate) is very low as well as EDM process. In order to reduce the post-casting/sintering processes, cemented carbides are now being produced in near-net shape. This has encouraged researchers to find alternative post-processing methods to improve the production of precision tools, molds and dies without sacrificing the quality of the surface finish.

Ultrasonic elliptical vibration cutting/milling of sintered tungsten carbide yields almost the same quality of surface finish as grinding [1]. Previous research has reported the influence of binder content of sintered WC on cutting performances of PCD and CBN tools [2,3]. However, significant machining characteristics such as cutting force and cutting temperature have not been clarified with respect to the workpiece properties of cemented carbides. Furthermore, the appropriate tool materials for cemented carbides are still incompletely understood.

Table 5.1 Properties of three kinds of cemented carbide

Specification of carbide	Grain size μm	Co content wt%	Thermal conductivity λ W/(m·K)	Vickers hardness *HV* GPa
WC-m (for mold)	3	25	71	8.2
WC-d (for die)	3	20	71	9.5
WC-t (for cutting tool)	2	12	71	13.3

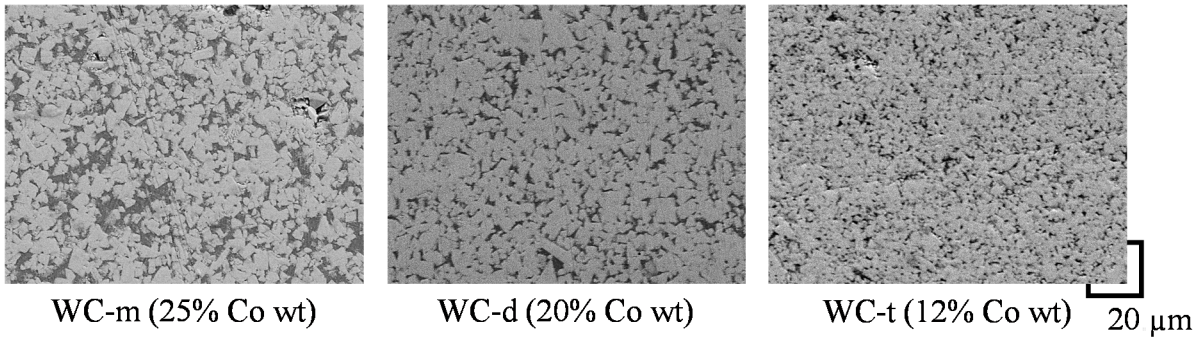

Fig. 5.1 Grain structures of cemented carbide workpieces

This chapter deals with the cutting performances of some diamond and CBN tools in hard turning of three types of cemented carbide material designed for mold, die and cutting tools, in which WC particle size and Co binder content are changed.

Table 5.2 Characteristics of cutting tools

Specification	Grain size μm	Binder content wt%	Thermal conductivity λ W/(m·K)	Vickers hardness *HV* GPa	Rake angle α °
CBN	2	7% Co	110-120	41 – 44	0
PCD-a	> 0.5	10% Co	480 – 560	50 – 60	0, 10
PCD-b	50	5% Co	480 – 560	60 – 80	0
BL-NPD	0.03 – 0.05	—	250 – 300	120 – 140	0
SC	—	—	1000 – 2200	70 – 120	0
CVD-SC	—	—	1000 – 2200	70 – 120	0

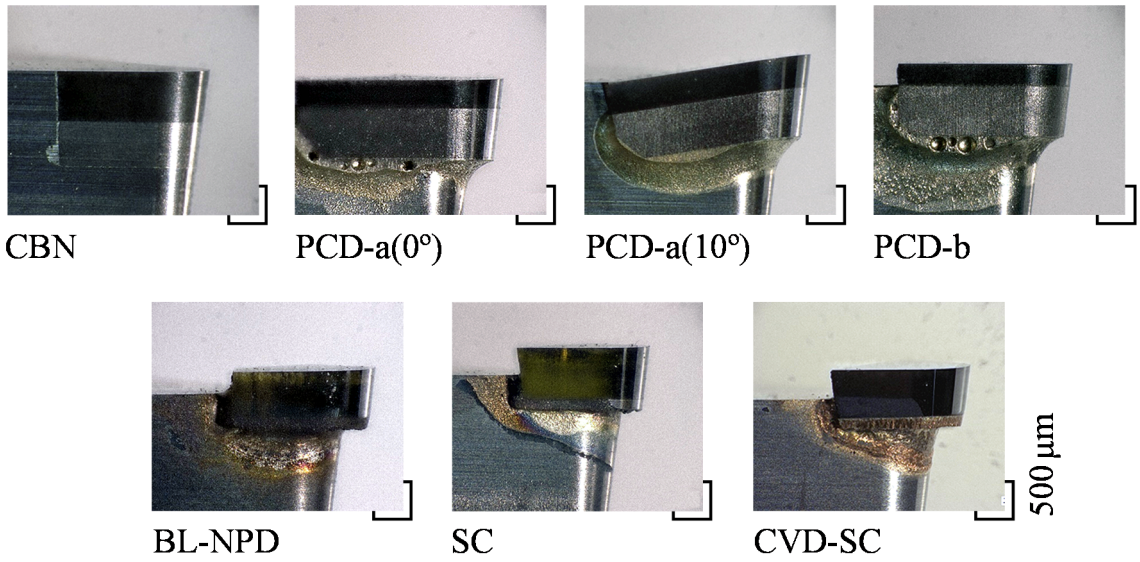

Fig. 5.2 Seven types of cutting tool

5.1 Experimental Procedure

5.1.1 Workpiece Material and Cutting Tools

Three types of cemented carbide – WC-m, WC-d and WC-t – with different mechanical characteristics are prepared, as shown in **Table 5.1.** The grain structure of these workpieces is

shown in **Fig. 5.1.** WC-m, used in mold-making contains about 25 wt% Co and is the softest of the carbides. WC-t, developed for tools, contains 12 wt% Co and is the hardest carbide, and

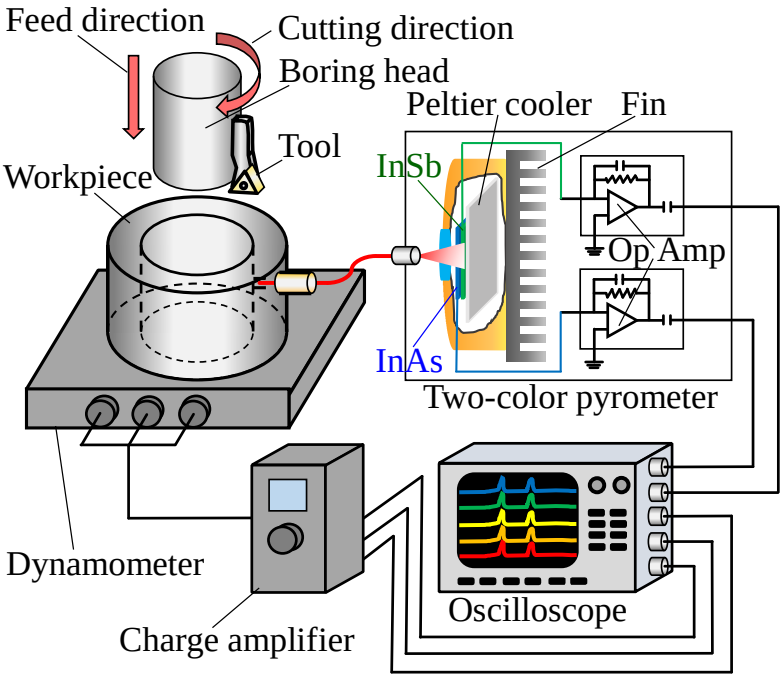

Fig. 5.3 Experimental arrangement

Table 5.3 Cutting conditions

Workpiece			Cemented carbide (WC-m, WC-d, WC-t)
Insert (Nose radius: r_ε = 0.8 mm)			CBN, PCD-a, PCD-b, BL-NPD, SC, CVD-SC
Cutting speed	v	m/s	40
Depth of cut	d	mm	0.05
Feed	f	mm/rev	0.1
Cutting style			Dry

WC-d, for dies, has medium hardness. These straight tungsten carbide grades have grain size of 2 to 3 µm.

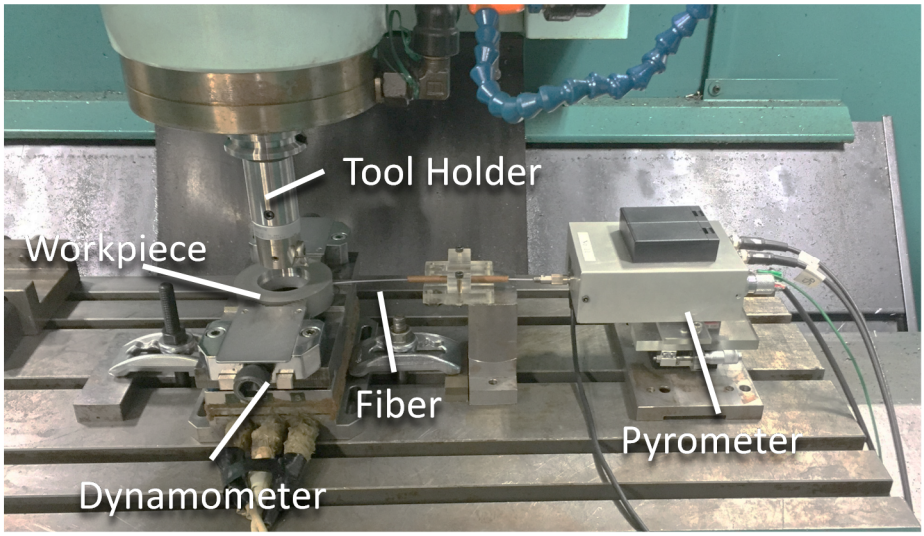

Fig. 5.4 Dry cutting assembly

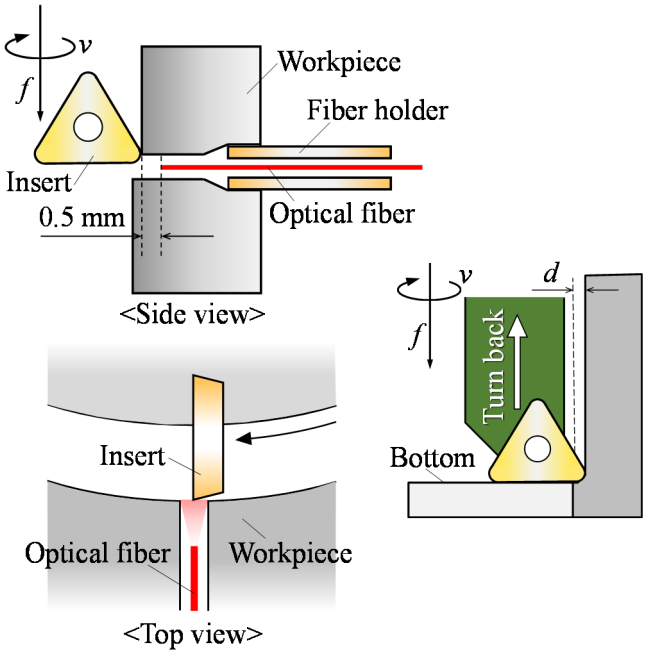

Fig. 5.5 Cutting temperature measurement

The tools used are made from CBN and five types of diamond: polycrystalline diamond (PCD-a, PCD-b), BL-NPD, SC diamond, and SC diamond produced by chemical vapor disposition (CVD-SC). The properties of these tool materials are listed in Table 4.2. **Fig. 5.2** illustrates seven cutting inserts.

5.1.2 Experimental Set-up and Conditions

The internal turning experiments are carried out without cutting fluid with the vertical machining center, as shown in **Fig. 5.3.** This experiment set-up on the machine is shown in **Fig. 5.4**. In order to assess the availability of cutting tools, a relatively high cutting speed of v=40 m/min is set, and other operating parameters as shown in Table 4.3 are also set as constant. The cutting performance of each tool is evaluated by cutting force, cutting temperature, surface roughness and tool wear. Cutting force, tool wear and surface roughness are measured by three-axis piezoelectric dynamometer, stylus profilometer and SEM, respectively. The cutting experiment is stopped upon reaching the flank wear width of 300 µm, or when signs of tool failure are observed. Two sets of cutting test are executed for each tool, where cutting force and surface profiles are measured as a first step and cutting force and cutting temperature in the second step.

5.2 Cutting Temperature Measurement

The cutting temperature is measured using a new compact two-color pyrometer. As shown in **Fig. 5.5**, the chalcogenide glass fiber is positioned into a small hole (ϕ1.1 mm), which extends to the internal surface of the tubular-shaped workpiece. The incidence face of the fiber receives the infrared rays emitted from the flank face of the cutting tool when it passes over

the hole throughout the cutting operation. The thermal radiation received by the fiber is conveyed to the two-color detector, in which InAs and InSb photocells are assembled in a sandwich structure. These detectors are electrically cooled by a Peltier device and have different spectral sensitivities in the ranges of 1–3 µm and 3–5.5 µm, respectively. Based on the output voltage ratio from these two detectors, the temperature of the object can be calculated using the calibration curve attained in the experiment. The pyrometer, having a flat response from 10 Hz to 400 kHz, can be used for tool temperature measurement in turning with a good degree of accuracy. This pyrometer type has been successfully applied in previous studies in cutting [4] and milling [5].

5.3 Experimental Results

In a preliminary experiment, the softest carbide (WC-m) is cut by the hardest tool (BL-NPD). The intensity of thermal radiation emitted from the tool is so low that it was undetectable by the pyrometer. This means that the tool temperature is very low, and no discussion of the tool performance is possible from the thermal viewpoint. For this reason, the PCD and CBN tools are assigned for WC-m cutting, and SC diamond, CVD-SC and BL-NPD for WC-d and WC-t.

5.3.1 Tool Wear

The experiment was carried out on three different carbides with five types of cutting tool. **Fig. 5.6** shows the change of flank wear width with cutting length *L* when the softest carbide, WC-m, is cut. As shown in the figure, the polycrystalline CBN tool has lower wear

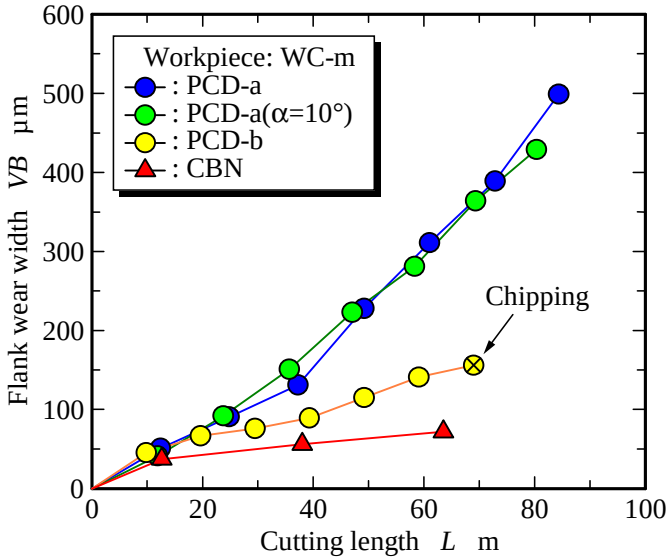

Fig. 5.6 Change of flank wear width with cutting length in turning of WC-m

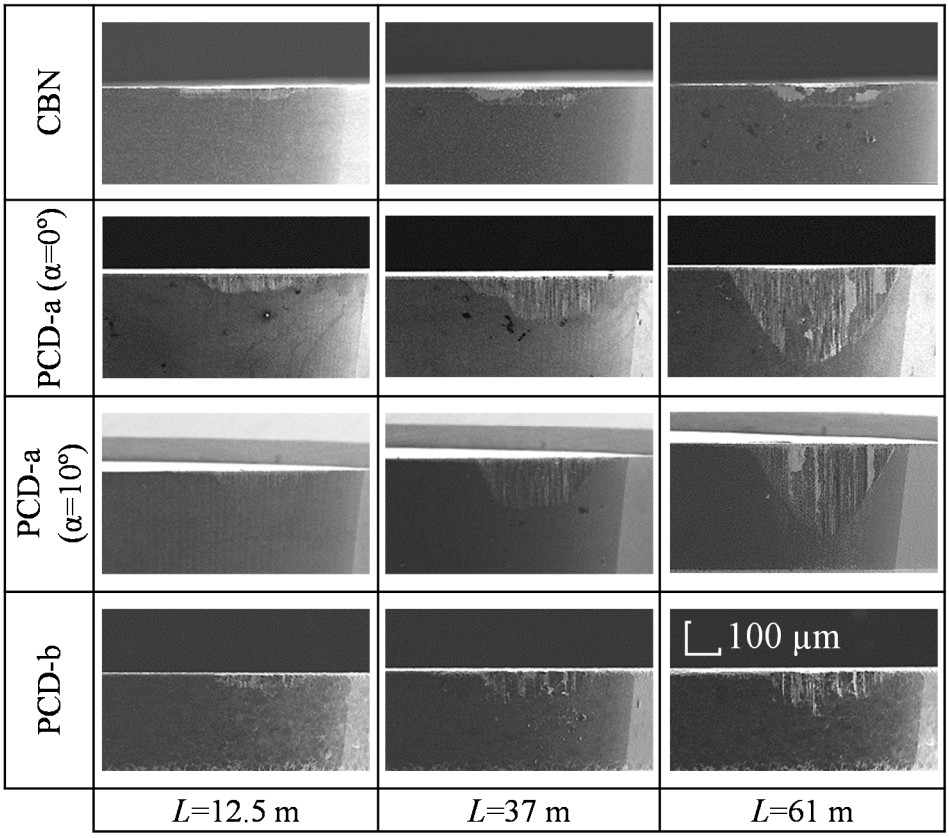

Fig. 5.7 SEM photographs of flank face in turning WC-m (see **Fig. 5.6**)

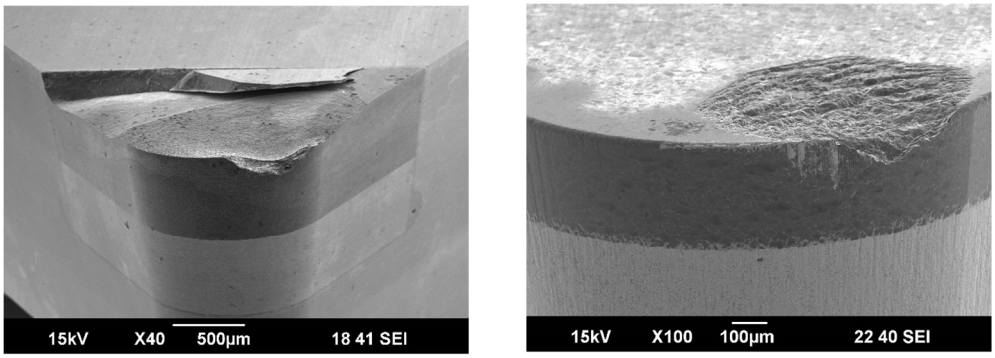

CBN (L = 89 m) (a)

PCD-b (L = 69 m) (b)

Fig. 5.8 Chipping on the cutting tools

than the PCD tool. This result is aligned with previous research [2] showing that CBN wears more slowly than PCD tools in cutting WC with higher cobalt content. The grain size of the CBN tool is very similar to that of WC-m, which seems to slow tool wear in comparison to PCD-b, which has a very similar cobalt binder content. In addition, CBN grains can endure interference between WC-m-grade carbides with cutting lengths within 64 m. As for PCD tools, the wear of PCD-b, with less Co content and larger grain size, is considerably smaller than that of PCD-a. The SEM photographs of the flank face at L =12.5, 37 and 61 m are shown in **Fig. 5.7**, in which traces of significant attrition can be observed, in the form of scratch marks, for PCD-a (α=0º, 10º). There is little evident effect of rake angle on tool wear. The CBN and PCD-b tools that show chipping during cutting of WC-m are shown in **Fig. 5.8**. This illustrates why these tools are not tested in cutting harder grades of cemented carbide.

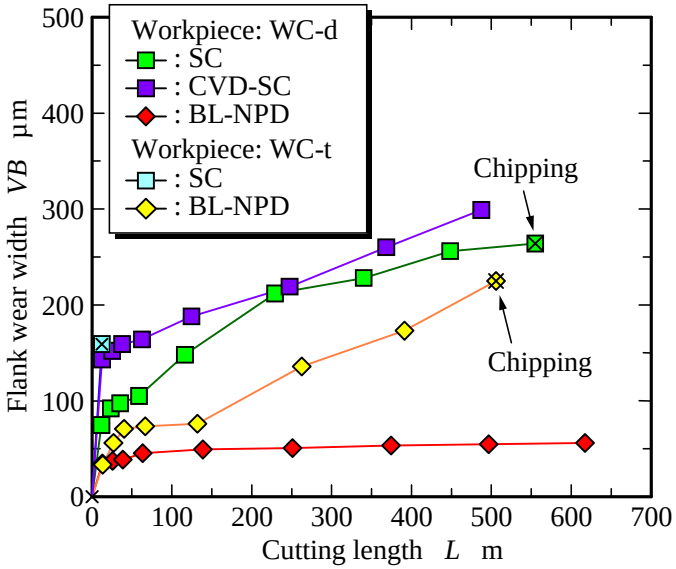

Fig. 5.9 Change of flank wear width with cutting length in turning of harder carbides WC-d and WC-t

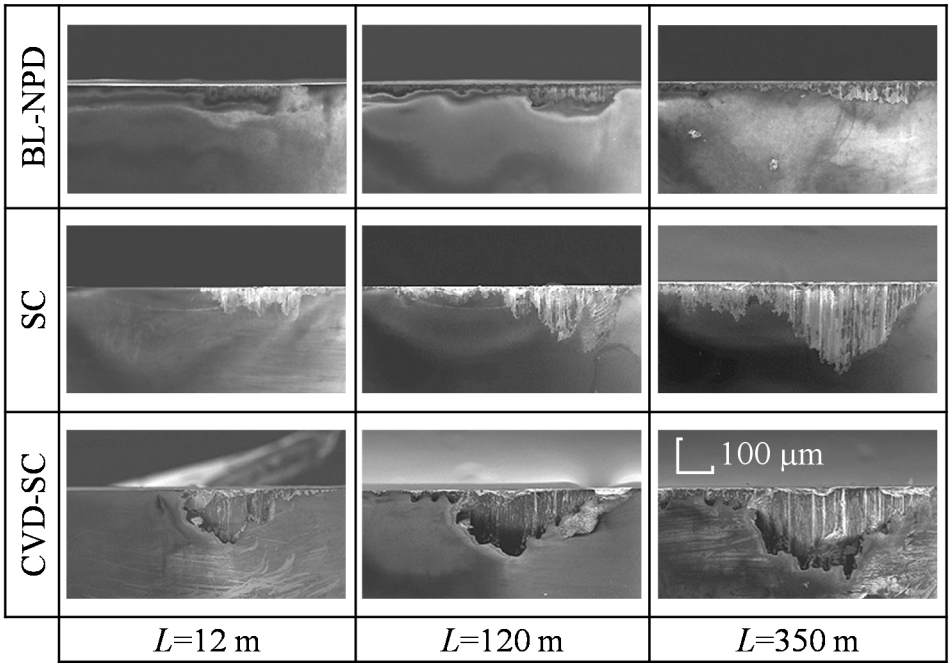

Fig. 5.10 SEM photographs of flank face in turning WC-d (see **Fig. 5.9**)

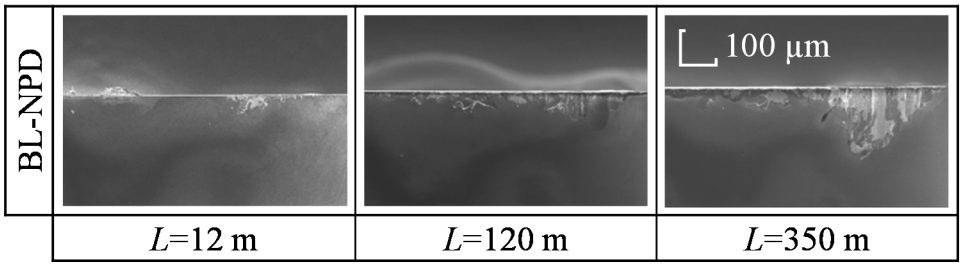

Fig. 5.11 SEM photographs of flank face in turning WC-t (see **Fig. 5.9**)

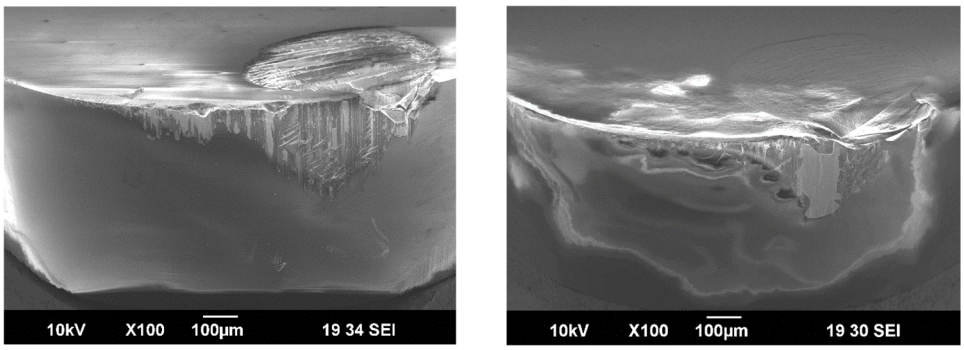

SC (L = 555 m) BL-NPD (L = 505 m)

(a) (b)

Fig. 5.12 Chipping on the cutting tools

Meanwhile, the change of flank wear width with cutting length L in turning of the harder carbides WC-d and WC-t is shown in **Fig. 5.9**. In cutting these harder materials, neither CBN nor PCD can be used continuously, due to the low hardness of the tool material; BL-NPD and SC diamond tools are applicable, however. Only BL-NPD is available for cutting of the hardest carbide, WC-t.

In turning of WC-d, the BL-NPD tool has the best cutting performance with the least flank wear. In the case of the SC diamond tool, on the other hand, the flank wear with *VB*

approaches approximately 270 µm at the cutting length of 560 m, and chipping occurs at the same time. **Fig. 5.10** represents the SEM photographs of the tool flank, and it is visible that the cutting-edge geometry of BL-NPD remains almost constant. CVD-SC shows similar behavior to SC diamond because it has similar physical properties. In the case of CVD-SC, however, although wear rate is somewhat higher, chipping has not taken place. It is estimated that the toughness of CVD-SC is higher than that of SC diamond.

In the case of turning WC-t, the SC diamond tool undergoes chipping at the initial stage of cutting, whereas BL-NPD is able to continue cutting up to the cutting length of approximately 500 m. In most cases, chipping of the cutting edge occurs at the bottom of the workpiece where the feed stops and turns back immediately, as shown in **Fig. 5.5**; it is at this moment that a pulsed cutting force arises. This can cause the chipping. The SEM photographs of the flank face of BL-NPD are shown in **Fig. 5.11**. Despite turning WC-t, the hardest carbide material, the flank wear is smaller than that of SC diamond when turning the medium-hardness carbide WC-d. This abrasion resistance of BL-NPD can be explained by its high hardness and toughness, which emerge from the extremely fine grain size. From the above results, it can be concluded that BL-NPD has the best cutting ability of the tested materials in turning of cemented carbide. Based on the same physical properties of CVD-SD and SC, cutting test on WC-t is not done with CVD-SC tool. **Fig. 5.12** shows the chipping on SC diamond in cutting WD-d and on BL-NPD in cutting WD-t, as illustrated in **Fig. 5.9**.

5.3.2 Cutting Force

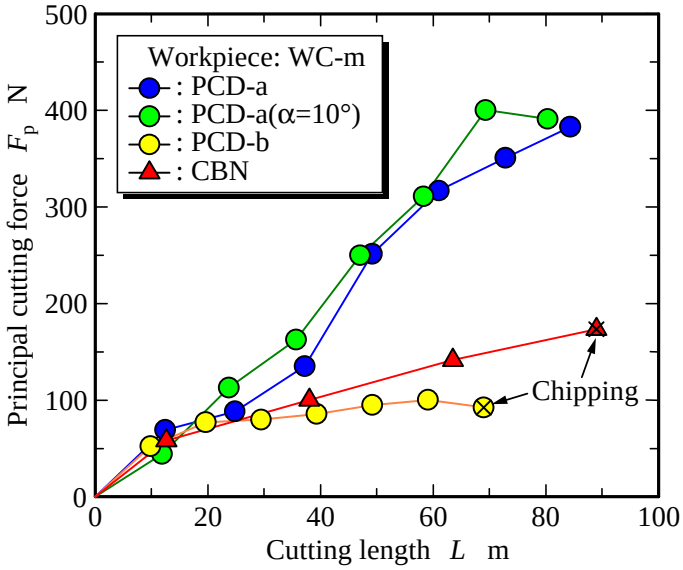

Fig. 5.13 Change of principal cutting force with cutting length in turning of softest carbide, WC-m

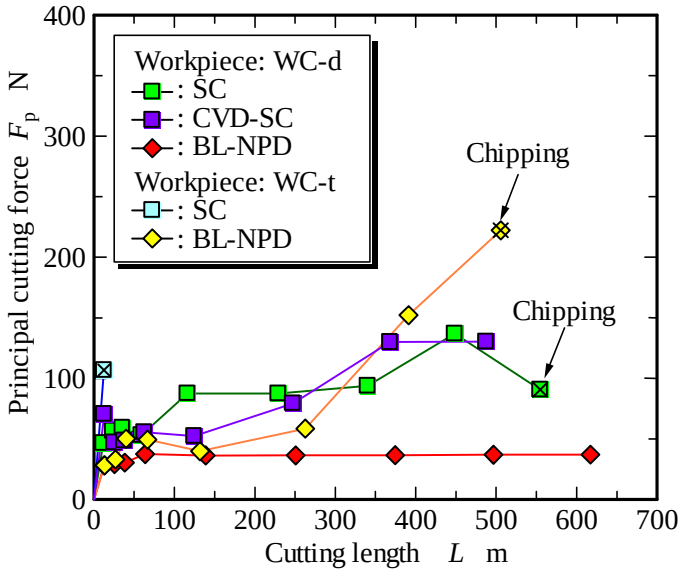

Fig. 5.14 Change of principal cutting force with cutting length in turning of carbides WC-d and WC-t

The change of cutting force with cutting length in turning of the softest carbide, WC-m, is shown in **Fig. 5.13**. It can be noticed from the figure that CBN and PCD-b show almost the same cutting forces, which are smaller than the other PCD tools. This shows a similar tendency as the tool wear characteristics shown in **Fig. 5.6**. From **Figs. 5.6** and **5.13**, the CBN tool seems to be suitable for cutting of cemented carbide sintered for molds.

Fig. 5.14 shows the cutting force in turning of the harder carbides WC-d and WC-t. To begin with the WC-d carbide, both SC diamond and BL-NPD are usable, although chipping occurs on the SC diamond tool when cutting length L approaches 560 m. BL-PCD, however, allows extremely stable cutting, where the principal cutting force is kept almost constant at 40 N. CVD-SC shows a similar tendency to the SC diamond tool, whereby the cutting force reaches approximately 130 N at 500 m without chipping. In the case of the hardest carbide, WC-t, the turning experiment can be continued with BL-NPD only. As shown in **Fig. 5.14**, the cutting force increases rapidly from L=260 m and reaches approximately 220 N at L=510 m, where a tool failure occurs. According to the above results, the cutting conditions should be set up to ensure that the cutting force does not exceed approximately 200 N.

5.3.3 Cutting Temperature

The tool flank temperature reading in cutting WC-m is shown in **Fig. 5.15**. Although this is a hard material, the tool temperatures measured are relatively low, below 450°C, due to the high thermal conductivities of the tool materials. It is estimated, however, that the temperatures at the chip–tool interface are somewhat higher than those at the flank face [6].

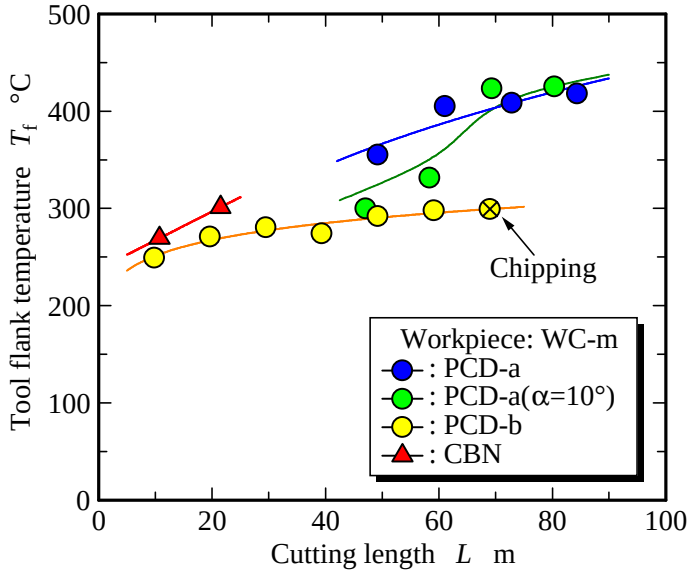

Fig. 5.15 Change of tool flank temperature with cutting length in turning of softest carbide, WC-m

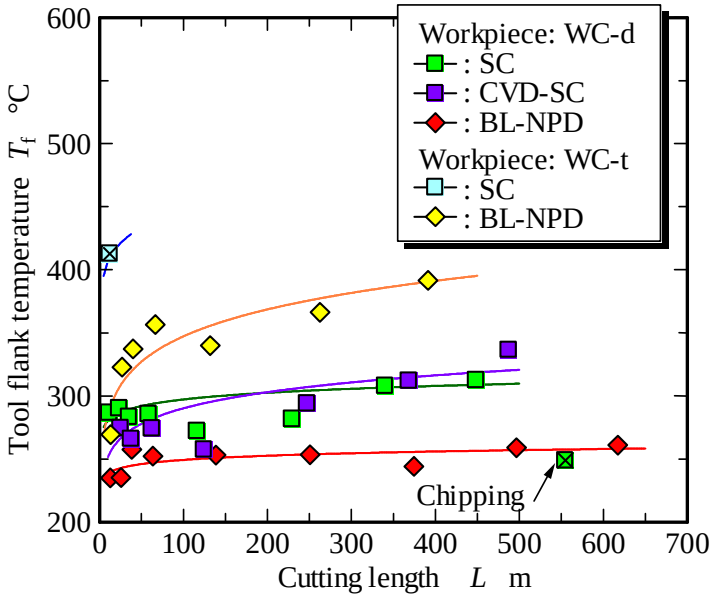

Fig. 5.16 Change of tool flank temperature with cutting length in turning of WC-d and WC-t

Both PCD-a (α=0° and 10°) tools indicate that higher temperatures over 400°C are associated with cutting force, as shown in **Fig. 5.13**. WC-m cutting with the CBN tool also produces temperature of around 250°C to 310°C within the cutting length of 20 m. In the case of CBN, the cutting temperature rises due to the low thermal conductivity, while the cutting force is kept

low. On the other hand, PCD-b emits a lower thermal energy in cutting WC-m in comparison to CBN and PCD-a. This is closely related to the combination of flank wear and cutting force, and also the thermal conductivity of PCD-b.

Meanwhile, when cutting the harder WC-d carbide, the cutting temperature T_f of BL-NPD is clearly lower than that of the SC and CVD-SC diamond tools, anchored around 250°C with a very slow increment, whereas the T_f values of SC diamond increase from approximately 270°C to 320°C. Meanwhile, with the CVD-SC tool T_f reaches a slightly higher value than with SC diamond at 340°C, but the temperature curve has a similar pattern due to the similarity between the tools' properties. This temperature difference is directly related to the lower tool wear and cutting force rather than thermal conductivity, as shown in **Figs. 5.9** and **5.14**. In this case, thermal conductivity has less effect on cutting temperature. Additionally, the SC diamond is not perfectly transparent and has some absorbance within the visible-to-infrared region. As shown in **Fig. 5.17**, both SC and CVD-SC diamond tools comprise colored materials; CVD-SC in particular looks almost opaque. Thermal radiation occurs when they become hot. Clear

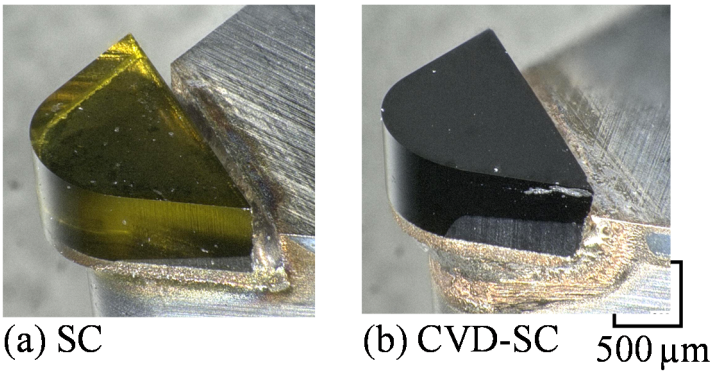

Fig. 5.17 Appearances of two types of SC diamond

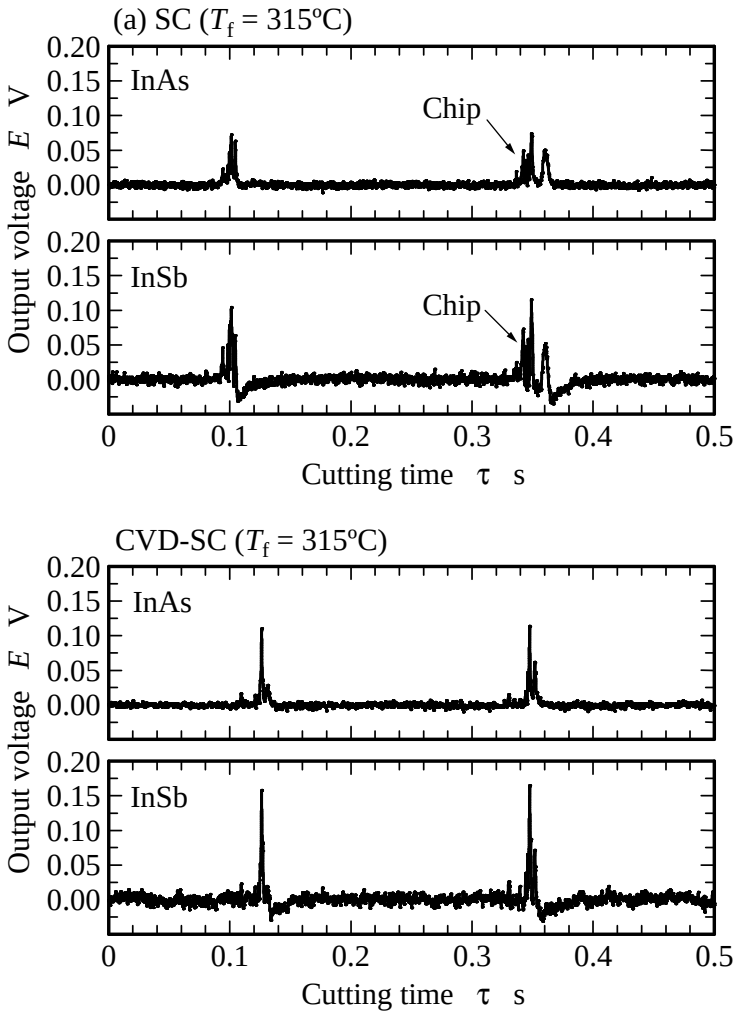

Fig. 5.18 Typical output voltage of the two-color pyrometer (InAs and InSb cells) when WC-d carbide is cut by the SC and CVD-SC diamond tools

output signals of thermal radiation were obtained from the tool flank faces for both SC and CVD-SC diamond tools, as shown in **Fig. 5.18**.

When cutting the hardest carbide, WC-t, the SC diamond tool breaks abruptly after the first cutting pass, as shown in **Fig. 5.14**, so that the temperature measurement cannot be continued; a peak temperature of about 420°C is obtained. This seems to be caused by significant flank wear, as shown in **Fig. 5.9**. It is clear here that WC-t is a very hard material to cut in dry and hard turning conditions. The cutting temperature of BL-NPD progressively increases from 275°C to 420°C as the tool wear grows in a steeper pattern than cutting

temperature in WC-d machining. The gradient of cutting temperature tabulated for BL-NPD, as shown in **Fig. 5.16**, again reflects the flank wear and cutting force.

5.3.4 Surface finish

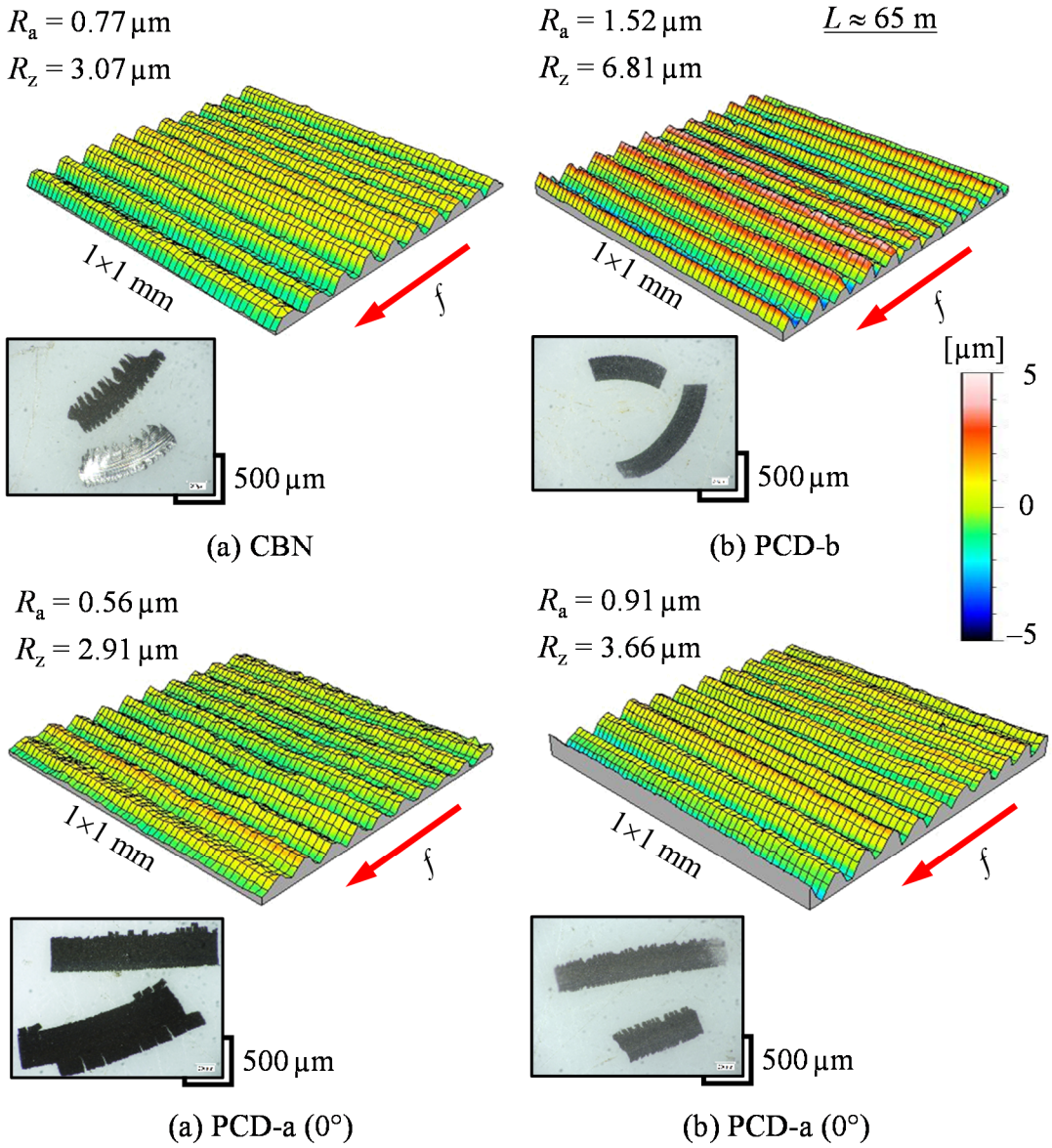

Fig. 5.19 3D surface profiles of WC-m cut by CBN, PCD-a and PCD-b

Figs. 5.19 and **5.20** represent the typical turned surface of WC-m carbide cut by CBN, PCD-a and PCD-b, and WC-d carbide cut by BL-NPD and SC and CVD-SC diamond tools, respectively. As seen in the figure, clear feed marks are observed on the machined surface. These stable finished surfaces seem to be formed by the plastic flow of workpiece material.

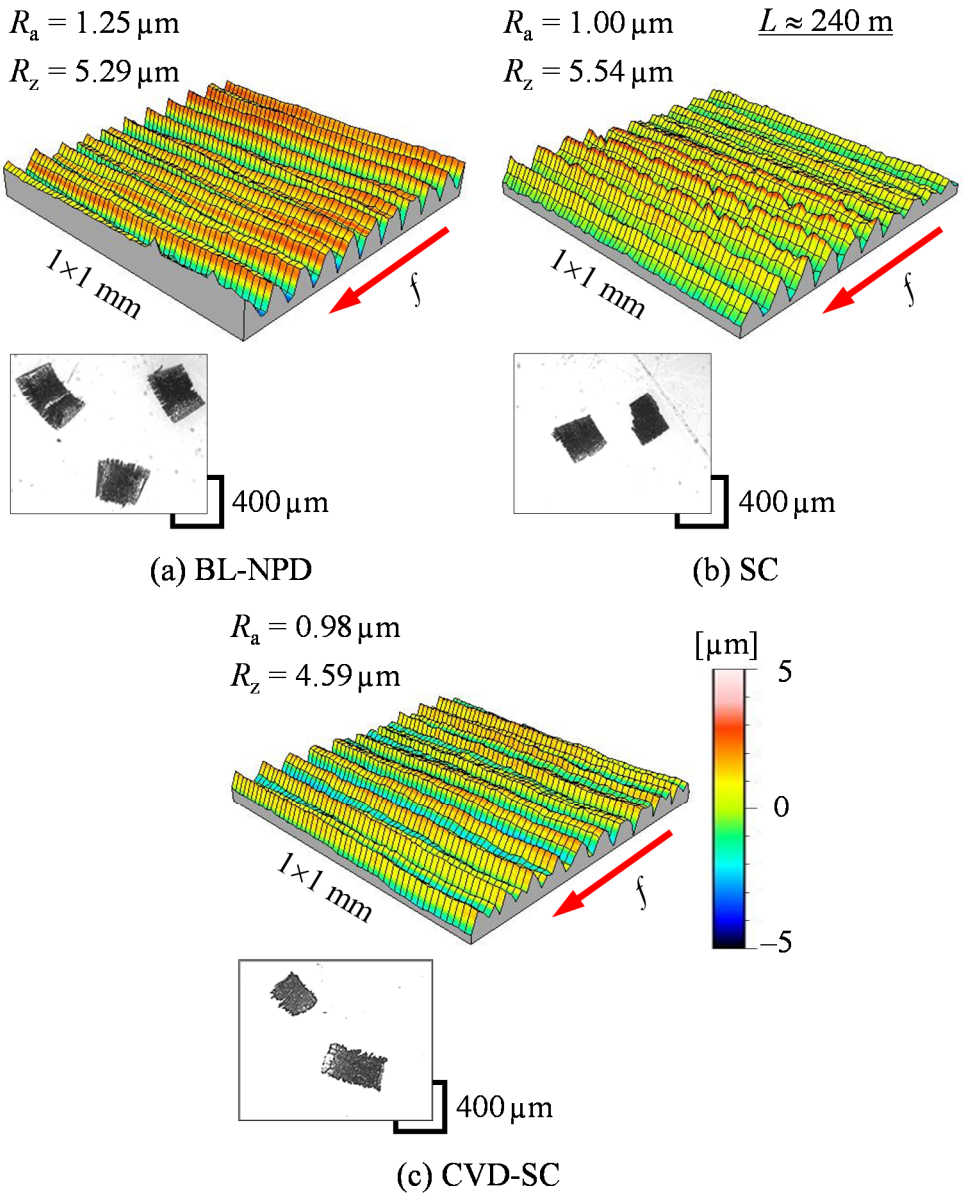

Fig. 5.20 3D surface profiles of WC-d cut by BL-NPD and SC and CVD-SC diamond

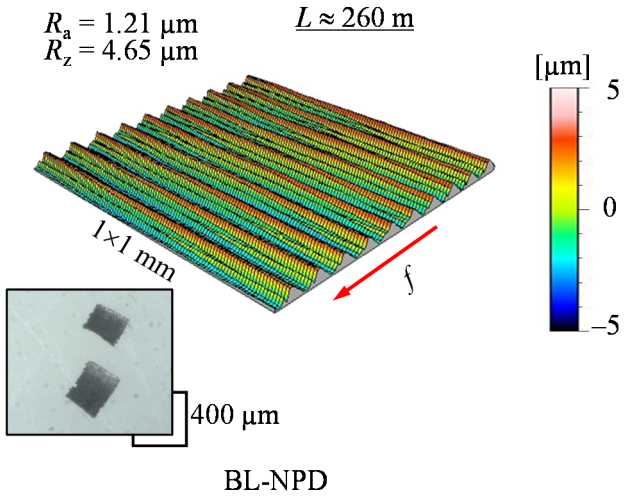

Fig. 5.21 3D surface profiles of WC-d cut by BL-NPD and SC and CVD-SC diamond

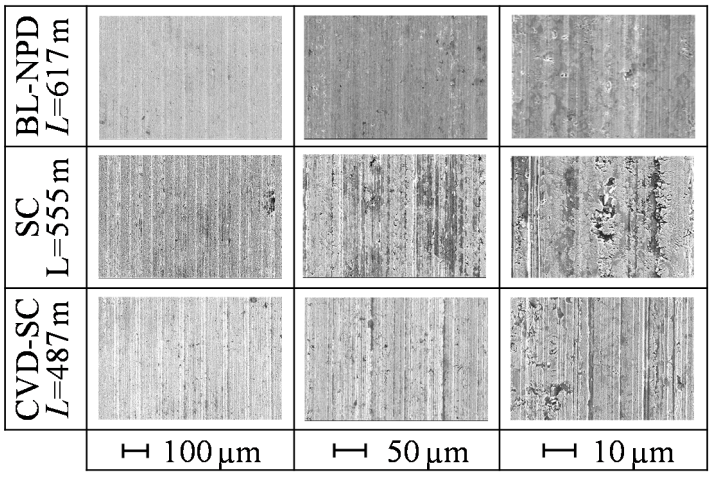

Fig. 5.22 SEM photographs of machined surface of WC-d cut by BL-NPD and SC and CVD-SC diamond

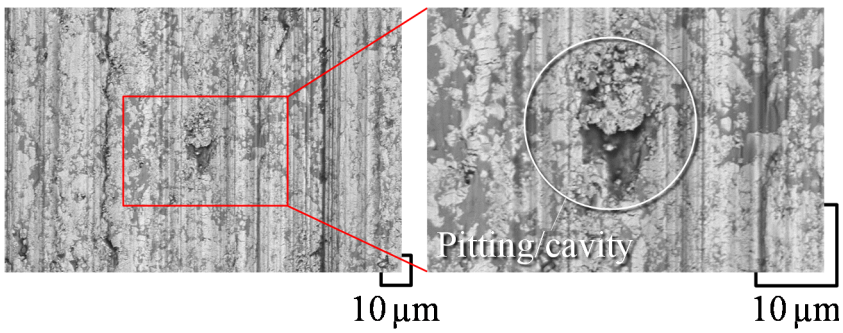

Fig. 5.23 Close-up BES images of pitting/cavity on WC-d surface machined by SC diamond tool

Ductile cutting has been achieved for WC-m, as shown in **Fig. 5.19**, using the discontinuous chip produced during cutting. The chip morphologies are also shown in **Figs. 5.20** and **5.21**: short-length semicontinuous chips are generated similar to high-carbon steel. According to the above results, it can be said that the cemented carbides for molds, dies and tools can be turned by the binderless diamond tools tested.

Further observations are made of the machined surface of the WC-d cut by BL-NPD and SC and CVD-SC diamond, as shown in **Fig. 5.22**. Cutting with SC and CVD-SC diamond produced obvious cavities/pitting at the end of the tool's life. This is clearly shown in **Fig. 5.23**. Meanwhile, cutting with BL-NPD produced a much smoother surface with smaller cavities/pitting in comparison to the results of SC and CVD-SC diamond cutting. On the other hand, clear marks of cutting were seen, similar to those shown in **Fig. 5.20**.

5.4 Discussion

Most of the tools experience attrition as the main tool wear mechanism. Failures are usually due to an exceeding of the allowable flank wear width and major chipping. With softer-grade cemented carbide (WC-m), however, most of the failures are due to mechanical shocks. Effects were similar for the harder-grade WC (WC-d and WC-t) with the harder BL-NPD and SC and CVD-SC diamond tools. The aforementioned tool wear mechanism is accompanied by some adhesion of the workpiece material. **Fig. 5.24** shows the EDS analysis of the adhesion section on the tool surface, including the mass percentage of W, C, Co and O. From the figure, it should be noticed that the adhesion of work materials (Co and W) is detected on the CBN,

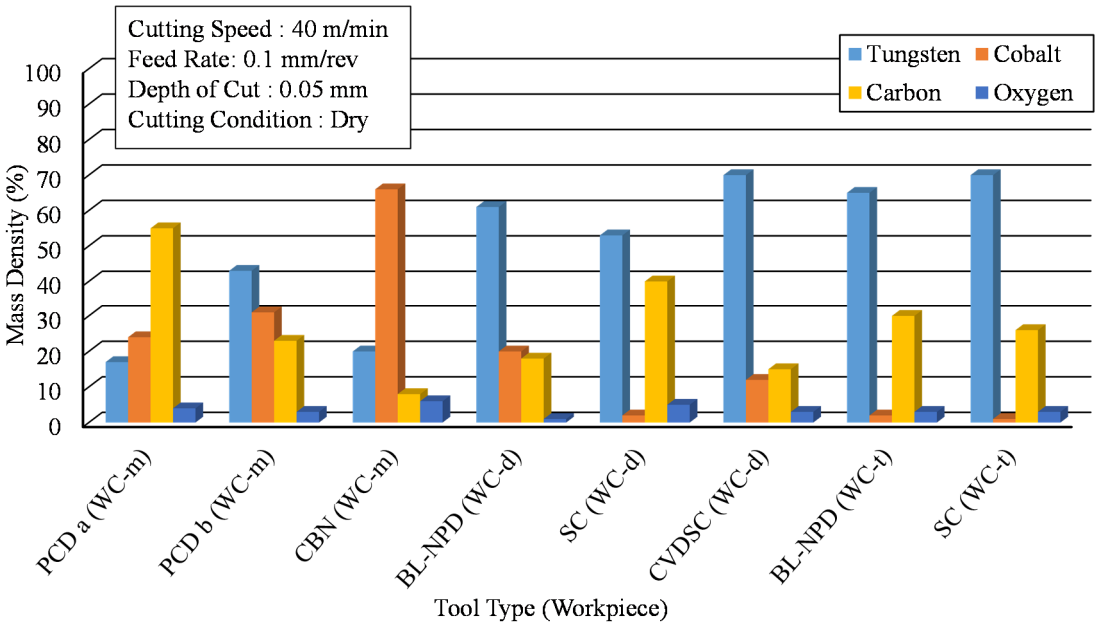

Fig. 5.24 EDS elemental analysis of adhesion at tool edge

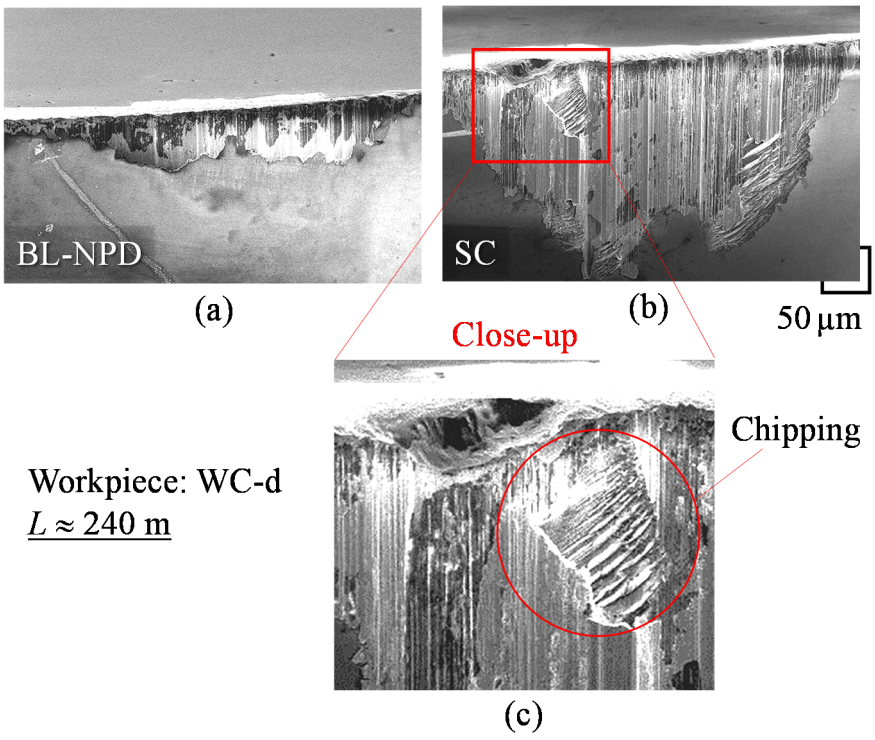

Fig. 5.25 Close-up SEM images of flank wear

BL-NPD, and SC and CVD-SC diamond tools. The influence of this adhesion on generation of chipping is not clear at the present stage.

Tool performance is somehow related to the tool hardness value and the grain structure of the tool. This is evident in cutting WC-d and WC-t with BL-NPD and SC and CVD-SC diamond tools, although these have almost the same hardness value. BL-NPD, with its grain size of several nm, seems to perform better in terms of cutting force and tool wear in comparison to the single-crystal-structured tools. In cutting WC-d, any tendency towards chipping or edge chipping is non-existent at the BL-NPD cutting edge, in contrast to the SC and CVD-SC diamond tools. These latter seem to incur chipping during cutting of WC particles, while BL-NPD wears in a gradual manner. Comparable performance has also been seen in previous research [7], where similar tools were used in cutting binderless cemented carbide.

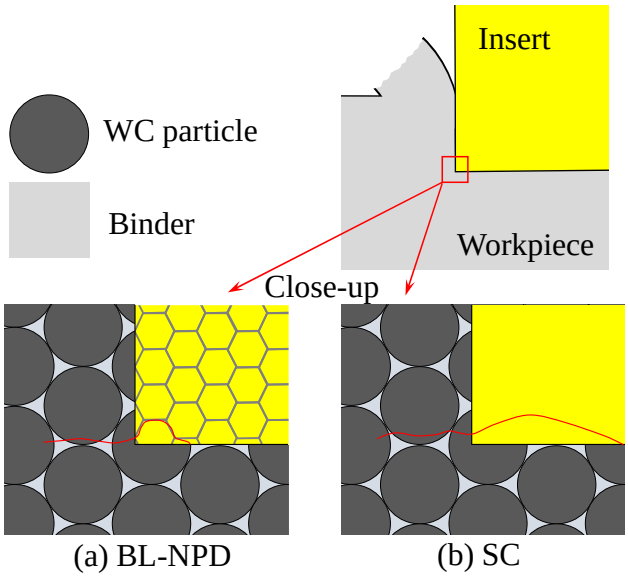

Fig. 5.26 Crack propagation model in cutting tools

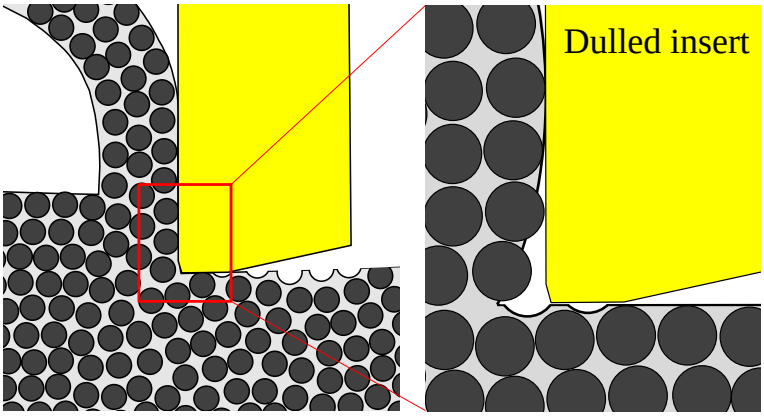

Fig. 5.27 Formation of machined surface by dulled SC/CVD-SC diamond tools (a). Magnified view in the vicinity of cutting edge showing cleaving and grain plucking by dulled SC/CVD-SC tools.

This wearing phenomenon is noticeable in **Fig. 5.25** and is explained further in **Fig. 5.26**. It is apparent that the nano-grained tool wears more gradually, and the crack formed by chipping to exposed WC particles is halted by other grains/particles interface before propagating to other areas in BL-NPD. This reduces large chipping and the tool will usually sustain attritional wear. Meanwhile, the structure of the SC and the CVD-SC diamond tools is a factor in localized chipping. This is due to the nature of singular crystals. When the worn tool starts to crack, the crack will propagate and become uncontrollable. This is the reason for the chipping that is visible at the tool edge.

The difficulties of cutting cemented carbide have been touched on in earlier studies [3]. This study emphasizes that as the binder content increases, carbides become much easier to cut as the spaces between the WC particles become bigger. Here, binderless small-grained (µm or

nm) tool material has been clearly shown to perform best in cutting of harder carbides. Tools with hard single-crystal structure are second best. The interaction between carbides and SC/CVD-SC diamond tools is explained in **Fig. 5.27**. It can be seen that WC grains can be ripped out by the SC and/or CVD-SC diamond tool. It can be concluded that as the tool draws near the end of its life, unsuccessful cutting of WC grains results in cavities/pitting on the machined surface; the WC grain is then plucked out of the workpiece by the plunging tool's cutting edge. This phenomenon also seems to cause chipping/micro-chipping of the tool face. This is an effect of the dulling process of cutting a WC-d workpiece using SC and CVD-SC diamond tools. It is obvious here that grain structure and hardness are important parameters in choosing a tool for cutting of cemented carbide, as these feature improve the tool's ability to withstand wear and maintain edge sharpness.

Tool flank temperature is low due to the high thermal conductivity of both the workpiece and the tool materials. Thermal conductivity values indicate the ability of the tool and workpiece to channel thermal energy away from the source; the higher the value, the quicker the thermal energy is transferred to the surroundings. However, **Figs. 5.14** and **5.16** suggest that cutting temperature is more influenced by cutting force (tool wear) than thermal conductivity in the case of the harder carbides WC-d and WC-t. SC diamond tools have been shown in previous research to produce high cutting temperature at slower cutting speed and higher depth of cut [6]. This phenomenon is similar in WC-m cutting, where although PCD-a has a higher thermal conductivity than the CBN tool, it shows a much higher cutting temperature, as shown in **Fig. 5.15**.

5.5 Conclusions

The cutting performance of the CBN and four types of diamond tool has been examined in dry turning of three grades of cemented carbide (WC), with Co binder content of 12%, 20% and 25%. The main results are summarized as follows.

(1) In cutting of the softest carbide, WC-m (25% Co), the polycrystalline CBN tool shows lower tool wear than any of the PCD tools, but not BL-NPD. Grain particles in the CBN tool are of similar size to the tungsten carbide particles in WC-m, improving the cutting performance of the tool, as shown in the relatively small attritional wear.

(2) In turning of the harder carbides WC-d (20% Co) and WC-t (12% Co), neither polycrystalline CBN nor PCD can be used continuously due to their low hardness, but BL-NPD and SC and CVD-SC diamond tools are applicable. The BL-NPD tool has the best cutting performance with the lowest flank wear. With WC-d, extremely stable cutting can be carried out with BL-NPD, where the principal cutting force is kept almost constant at 40 N. It can be reasonably assumed that the BL-NPD tool will also show the best performance in turning WC-m, as well as WC-d and WC-t.

(3) In the case of the hardest carbide, WC-t, turning can only be continued with BL-NPD, and the cutting force and flank wear width reach approximately 220 N and 270 μm, respectively, as the cutting length exceeds 500 m.

(4) Although hard materials are being turned, the tool temperatures measured are relatively low, below 450°C, due to the high thermal conductivities of tool materials. However, cutting temperature is directly related to the tool wear and cutting force rather than thermal conductivity in turning of WC-d and WC-t.

(5) The stable finished surface is formed by clear feed mark on machined surface indicating that the tool geometry is maintained in cutting all carbides.

References:

[1]. Nath, C., Rahman, M. and Neo, K. S., Machinability study of tungsten carbide using PCD tools under ultrasonic elliptical vibration cutting, International Journal of Machine Tools and Manufacture, Vol. 49, No. 14 (2009), pp.1089–1095.

[2]. Fujiwara, J., Wakao, K. and Miyamoto, T., Influence of tungsten-carbide and cobalt on tool wear in cutting of cemented carbides with polycrystalline diamond tool, International Journal of Automation Technology, Vol. 7, No. 4 (2013), pp.433–438.

[3]. Miyamoto, T., Fujiwara, J. and Wakao, K., Influence of WC and Co in cutting cemented carbides with PCD and CBN tools, Key Engineering Materials, Vol. 407–408 (2009), pp.428–431.

[4]. Moriwaki, T., Tsurimoto, S. and Ueda, T., Cutting temperature in diamond turning of tungsten carbide, Proceedings of the 13th euspen International Conference, Vol. 2 (2013), pp.43–46.

[5]. Okada, M., Hosokawa, A., Tanaka, R. and Ueda, T., Cutting performance of PVD coated and CBN tools in hardmilling, International Journal of Machine Tools and Manufacture, Vol. 51, No. 2 (2010), pp.127–132.

[6]. Tanaka, R., Hosokawa, A., Furumoto, T. and Ueda, T., Wear characteristics of ceramic tools when turning BN free-machining steel, Journal of Advanced Mechanical Design Systems and Manufacturing, Vol. 7, No. 3 (2013), pp.474–484.

[7]. Yui, A., Okuyama, S., Kitajima, T., Okahata, G., Sumiya, H. and Harano, K., Performance of single-crystalline and nanometer-sized polycrystalline diamond tools in cutting cobalt-free tungsten carbide under face turning, Proceedings of the 12th euspen International Conference, Vol. 2 (2012), pp.307–310.

CHAPTER 6: CONCLUSION

Advancements in the machine world are rapidly evolving. Demand for specific-use components in the manufacturing industry is increasing, and materials such as titanium alloys are used in the aerospace and biomedical industries. Cemented carbide is used to manufacture tools, dies and molds used in the production of components such as glass lenses, drawn wires and cutting tools. Demand for efficient means of producing components using these materials has increased due to the high costs that are currently incurred.

In this study, several tools have been successfully tested in cutting of titanium alloys and cemented carbides. The main emphasis however has been on BL-NPD, a binderless polycrystalline diamond tool material with grain size of 30–50 nm, Vickers hardness of 120–140 GPa and thermal conductivity of 250–300 W/(m·K). BL-NPD tools have been thoroughly investigated in terms of cutting performance and tool life. The findings have been addressed in Chapter 4 and Chapter 5.

Chapter 2 provided an overview of difficult-to-machine material cutting. Means of measuring tool performance were explained, with a focus on tool life. Previous studies on the

cutting of titanium alloys and cemented carbide were also discussed, and previous studies on cutting temperature in relation to these materials were reviewed.

In Chapter 3, the principles of the two-color pyrometer were introduced. This pyrometer measures the temperature generated in turning operation using the infrared radiation channeled through an optical fiber to the detector from the desired target area. This detector, consisting of InAs and InSb cells sandwiched together, turns the infrared radiation that is received into electrical signals. By using two detectors, the emissivity problem in the infrared pyrometer is mitigated. The calibration of the pyrometer shows an exceptional level of accuracy in temperature measurement.

In Chapter 4, SC diamond tools showed better performance than BL-NPD tools in high-speed cutting of Ti-6Al-4V. It should be noted that this type of cutting at 300 m/min induces high temperature, although it is carried out using a flooded coolant delivery technique. Titanium alloys, though they have desirable material properties, are known to accelerate tool wear due to high cutting temperature and chemical reactions with the tool material. It is clear here that the formation of titanium carbide does not inhibit diffusion wear on the tool in high-speed cutting in wet conditions. Although BL-NPD has rather high thermal conductivity, the wear severely reduces the tool's life expectancy. This is due to the polycrystalline structure and the nano-sized grain. This physical attribute accelerates the tool wear mechanism. The thermal conductivity value of BL-NPD is not able to mitigate the thermal damage, despite the flooding technique. This is clearly shown in the cutting temperature measured throughout the experiment. The SC diamond tool excelled in this study, showing lower wear on the cutting edge. Diffusion wear is believed to occur with SC diamond tools, but at a slower rate. The

single-crystal structure is found to reduce diffusion wear. Furthermore, the very high thermal conductivity of the SC diamond material helps to transfer the thermal energy to the coolant medium. This has been proven effective in reducing the cutting temperature, thus reducing the thermal damage on the tool edge. With lower adhesion, SC diamond shows very promising tool performance in high-speed cutting of titanium alloys.

In Chapter 5, the BL-NPD tool was shown to have the best performance in cutting harder-grade cemented carbides. The cutting performance of the binder tool material, CBN, was shown to be better than that of PCD with cemented carbides, due to the similar grain sizes and the similarity of these grain sizes to those in the workpiece. It should be noted that the CBN tool is limited to the softest cemented carbide tested. This is due to the mechanical shock endured by the tool during cutting. The hardness and grain structure of the tool help determine the performance in cutting of cemented carbide. If applicable, CBN is preferred over PCD tools in this context due to better performance in terms of tool wear. Binderless tools reign supreme over single-crystal tools here. BL-NPD, which has a nano-sized grain structure, wears more gradually than SC diamond. The micro-cracking on the tool does not propagate as fast as it does on SC diamond. This slows tool wear and lowers cutting force, thus also lowering cutting temperature. It should be noted that thermal conductivity influences the cutting temperature. Tools that have higher thermal conductivity emit a lower cutting temperature, but cutting force outweighs this influence. This study has shown that cutting force has the most significant influence on cutting temperature. Ductile cutting of cemented carbide has been achieved with indication of clear feed marks on the machined surface.

In high-speed cutting of titanium alloys, or other workpieces with similar attributes, using conventional coolant delivery, the best tool is certain to have a single-crystal structure and very high thermal conductivity. This study has shown that thermal wear damage such as diffusion–dissolution greatly reduces the life of polycrystalline tools. As this type of wear involves very high cutting temperature, tools which have high or very high thermal conductivity are certainly needed.

The study has suggested that strong tool candidates for the cutting of cemented carbide should have high hardness with a binderless polycrystalline structure. This requirement is based on the tool wear induced during cutting in BL-PCD and SC diamond tools. The results have shown that cutting of cemented carbide does not induce high temperature because of the combined thermal conductivity of tool and workpiece. Hard turning at 40 m/min is possible, although this might not be the recommended cutting speed.

The pursuit of the best performing cutting tool will not be ending in the near future. A better understanding of the cutting requirements of new components is needed for new tools be developed. The introduction of more difficult-to-machine materials needs to be addressed by improving tool materials. It is recommended that the simulation on cutting performance based on the result from this study is to be developed in the future. Furthermore, comparative studies with binderless nano-polycrystalline and single-crystal CBN could also be carried out. MQL (minimum quantity lubrication) cutting of cemented carbides seems a suitable method for future works.

LIST OF PUBLICATIONS

1. Abang Mohammad Nizam Abang Kamaruddin, Akira Hosokawa, Takashi Ueda, Tatsuaki Furumoto, Tomohiro Koyano, “Cutting Performance of CBN and Diamond Tools in Dry Turning of Cemented Carbide” The 8th International Conference on Leading Edge Manufacturing in 21st Century (LEM21 2015), Kyoto, Japan, 2015
2. Abang Mohammad Nizam Abang Kamaruddin, Akira Hosokawa, Takashi Ueda, Tatsuaki Furumoto, Tomohiro Koyano, “Cutting Performance of CBN and Diamond Tools in Dry Turning of Cemented Carbide” Mechanical Engineering Journal, JSME, Vol. 3, No. 1, p. 15-00526, 2016.
3. Abang Mohammad Nizam Abang Kamaruddin, Akira Hosokawa, Takashi Ueda, Tatsuaki Furumoto, “High Speed Cutting of Ti-6Al-4V with Diamond Tools” International Journal of Automation Technology, accepted Feb. 25, 2016.

ACKNOWLEDGEMENT

This dissertation will not be possible without the help of numerous individual in so many ways. First of all I would like to express my deepest gratitude to my advisors, Prof. Akira Hosokawa and Prof. Takashi Ueda for the precious guidance, advises and encouragements that have been provided throughout my research. I am also would like to thank Assocs. Prof. Tatsuaki Furumoto for the helps and guidance that he have given me. A very deep appreciation to Prof. Ryiochi Monzen and Assocs. Prof .Chihiro Watanabe for the advices and opinions on my research works. Last but not least, I would like to thank Dr. Tomohiro Koyano, Dr. Yohei Hashimoto and all the members of Manufacturing Systems Laboratory for the advices and the help during presentation and experiments.

I would like to express my deepest thankfulness toward my parents, Abang Kamaruddin Abang Fauzan and Fatimah Poli for non-stop prayers and for believing in me. I also would like to extend my appreciation and gratitude towards Malaysian community in Kanazawa for their invaluable help.

I am also would like to sincerely thank the Sumitomo Electric Hardmetal Co. Ltd. for generously helping with advices and providing us with tools and workpieces to work with. Last but not least, I am grateful to Ministry of Education, Malaysia and Universiti Malaysia Sarawak for their financial supports during my studies at Kanazawa University.